INFLUENCE OF LITHOLOGIC VARIABILITY ON NANOPORE SYSTEMS, NIOBRARA INTERVAL, DENVER-JULESBURG AND PICEANCE BASINS, COLORADO, USA

by

WESLEY EVANS BALL

B.S., Western Washington University, 2013

A thesis submitted to the Faculty of the

Graduate School of the

University of Colorado in Partial fulfillment

of the requirement for the degree of

Master of Science

Department of Geological Sciences

2015

This thesis entitled:
Influence of Lithologic Variability on Nanopore Systems, Niobrara Interval, Denver-Julesburg and Piceance Basins, Colorado, USA
written by Wesley Evans Ball
has been approved for the Department of Geological Sciences
by

_____
David A. Budd

_____
Paul Weimer

_____
Edmund Gustason

Date_____

The final copy of this thesis has been examined by the signatories, and we find that both the content and the form meet acceptable presentation standards of scholarly work in the above mentioned discipline.

Ball, Wesley Evans (M.S., Geological Sciences)

Influence of Lithologic Variability on Nanopore Systems, Niobrara Interval, Denver-Julesburg and Piceance Basins, Colorado, USA

Thesis directed by Dr. David A. Budd

ABSTRACT

The Niobrara Formation, Denver-Julesburg (DJ) and Piceance basins, Colorado, is one of the most active unconventional petroleum plays in the United States. This study characterizes those pore systems in one well in the DJ Basin and two wells in the Piceance Basin in order to isolate the impact of lithologic variability on pore characteristics. This objective is accomplished through the combination of scanning electron microscopy of Ar-milled rock surfaces, image analysis with Avizio 9 software, and mineralogical characterization by X-ray fluorescence (XRF) and electron microprobe mapping.

The twenty-one imaged samples span the chalk to marly shale lithologies of the Niobrara Interval. This study focuses on the pre-hydrocarbon migration pore systems in order to minimize the influences of differential hydrocarbon saturations, surface wettability, and post-migration thermal maturation. The goal of this project is to understand the basic lithologic controls on the pore systems. Data on size, shape, and orientation of individual pores were collected and compared to lithology (weight percent calcium) and grouped by fabric element to establish trends that can be related to well-scale observations.

Total pre-migration porosity positively correlates to lithology ($r = 0.93$) with a range of 3.4% to 11.7%, with the chalkiest samples showing the greatest porosity. Median pore size,

width, anisotropy, and degree of horizontal orientation also all correlate, to varying degrees, with lithology. Overall, pores associated with peloids (always calcitic) and calcitic matrices (chalk and marly chalk) consistently display the largest sizes (medians of ~175 nm), most equant shapes, and smallest horizontal preference. In contrast, pores in clay-rich, calcite-poor matrices (marl and shaley marl) are the smallest (medians of ~150 nm), most elongate, and most horizontal.

Petroleum explorationists should guide drilling toward zones of the highest calcite and peloid concentrations in order to find the largest and best connected pore systems. Pairing this information with an understanding of the thermal maturity and hydrocarbon saturations will help identify the most favorable petroleum resources in the Niobrara Formation.

Contents

TABLES

FIGURES

CHAPTER 1: INTRODUCTION

Recent developments in petroleum exploration and production have increased the viability of targets deemed unproducible even in the latest part of the last century. The introduction of horizontal drilling paired with multi-stage hydraulic fracturing has negated many of the production limitations associated with low permeability lithologies. As of 2013, estimates of technically recoverable shale and other tight reservoir reserves inside the United States had reached 58 billion barrels oil and 665 tcf wet gas, representing 26% and 27% of total recoverable oil and gas respectively (http://www.eia.gov/analysis/studies/worldshalegas/). This rise in energy production capability has led to a natural gas independence for the United States estimated to last for the next 30 to 100 years (Jarvie, 2010). In addition, natural gas usage has, in part, led to a 10.4% decrease in US CO_2 emissions since 2005 (http://www.eia.gov/environment/emissions/carbon/).

Given the importance of the pore systems in these newly accessible petroleum reservoirs, both industry and academia have placed an emphasis on the study of porosity and permeability at the micro-nanometer scale. By combining traditional scanning electron microscopy techniques, argon-milling, and focused ion-beam milling, both high quality 2-D and 3-D renderings have given researchers insight into intricacies of pore systems too small to be explored previously. This type of study has focused on dominantly siliciclastic units such as the Barnett and Marcellus (Loucks et al., 2009, 2010; Milliken et al., 2010, 2012; Schieber, 2010; Slatt and O'Brien, 2011; Chalmers et al., 2012; Tian et al., 2013). More carbonate-rich unconventional reservoirs such as the Pearsall, Eagle Ford, Missisipian Lime, and Niobrara (Loucks et al., 2012; Milliken et al., 2013, 2014; Loucks et al., 2014; Michaels, 2014; Burt, 2014;

Pommer et al., 2014; Zhao et al., 2014) have been less heavily studied, leaving questions about the impacts of carbonate mineralogy on these types of systems unanswered. Characterization and evaluation of pore type, size, and shape are the first steps in a more complete understanding of how variable mineralogy impacts hydrocarbon storage and mobility.

The Rocky Mountain region is host to multiple petroliferous basins (Fig. 1) with oil and gas production from sandstone, shale, and carbonate reservoirs (Nelson and Santus, 2011). Two basins with recent interest and strong unconventional petroleum production since the early 2000s are the Denver-Julesberg (DJ) in eastern Colorado, Wyoming, and Nebraska and the Piceance in western Colorado and eastern Utah. Two recent publications by Burt (2014) and Michaels (2014) focused on the characterization of the Niobrara pore systems in these two basins. The goal of those studies was to analyze pore system heterogeneity as a function of thermal maturity in the primary drilling zones of each basin in order to gauge the impact organic material maturation has on the pore systems. In contrast, this study focuses on characterization of lithofacies heterogeneity through seven vertical intervals of the Niobrara in the DJ basin and through the dominant producing interval in the Piceance Basin, while limiting lateral variation and the effects of thermal maturity.

The Denver-Julesberg Basin is host to Colorado's largest producing oil field (Wattenberg) and currently produces from both conventional and unconventional reservoirs. Production in the DJ Basin began in Boulder County in 1901 with the discovery of oil in fractured reservoirs of the Pierre shale (http://www.coga.org/index.php/FastFacts/EnergyFactsArticle/history_of_the_second_oldest_oilfield_in_the_united_states_florence_colorad#sthash.XAuaPcsm.dpbs). Since then,

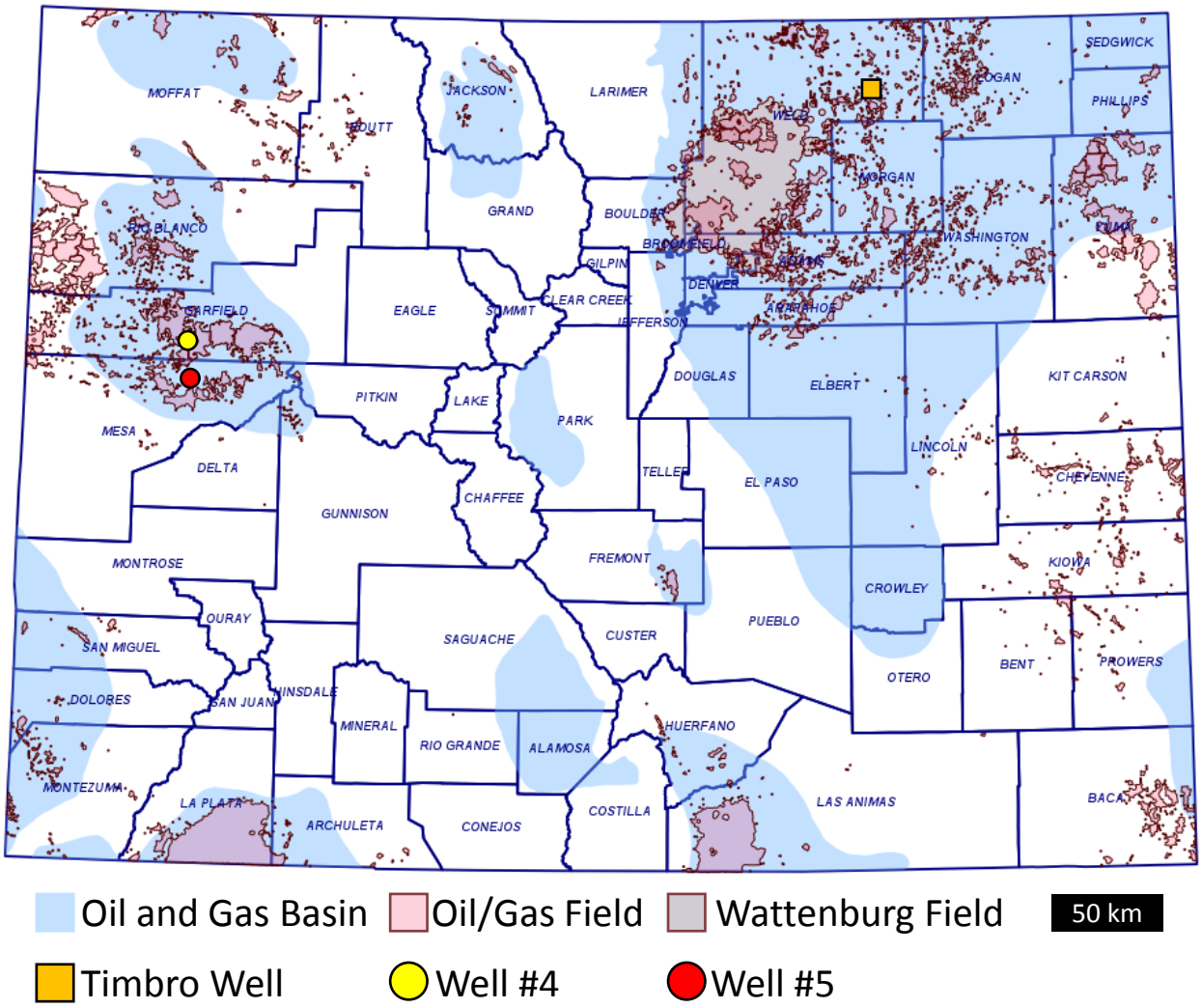

Figure 1. Map of Colorado's petroliferous basins and oil and gas fields (http://dnrwebmapgdev.state.co.us/mg2012app/). Shown approximately are the locations of the three wells used for this study.

production in this area has grown and changed immensely and while drilling for oil in the J Sandstone in the 1980's, gas accumulations were recognized in the overlying Cretaceous chalks of the Niobrara Formation (Nelson and Santus, 2011). In 2009, EOG dilled the #201H Jake, the first lateral, multi-stage hydraulically-stimulated well in the Niobrara Formation in Weld County, Colorado (Williams and Lyle, 2011). It was this discovery that has led to the Niobrara becoming not only the biggest producing interval in Colorado, but one of the largest unconventional plays in the country.

In the Piceance basin, the coeval deposits to the DJ Basin's Niobrara Formation is the Niobrara Member of the Mancos Shale. Despite lithologic differences between the two basins, the Niobrara Member remains a key gas-producing unit in western Colorado. The Mancos in Rangely Field has produced from fractured shale reservoirs since discovery in 1903 (Peterson, 1955) with over 15 million barrels of oil produced from the Niobrara member since that time (Cumella et al., 2014). The Piceance Basin Niobrara currently produces both oil and gas with three distinct play types from both vertical and horizontal wells (Cumella et al., 2014).

In the DJ Basin, the Niobrara Formation is known for its multi-scaled lithologic oscillations between chalks and marls (Fig. 2). In the Piceance Basin, this alteration is between marls and shaley marls, thus it is not as visibly obvious. These stratigraphic variations, hypothesized to be due to changing relative amounts of siliciclastic input and planktonic fallout connected to Milankovich cyclicity (Locklair and Sageman, 2008), leads to varying hydrocarbon production throughout the Niobrara. This study attempts to identify and categorize any variation in original, pre-migration pore systems associated with the stratigraphic and litho-chemical oscillations. This goal is achieved through the study of FE-SEM analysis in 21 samples

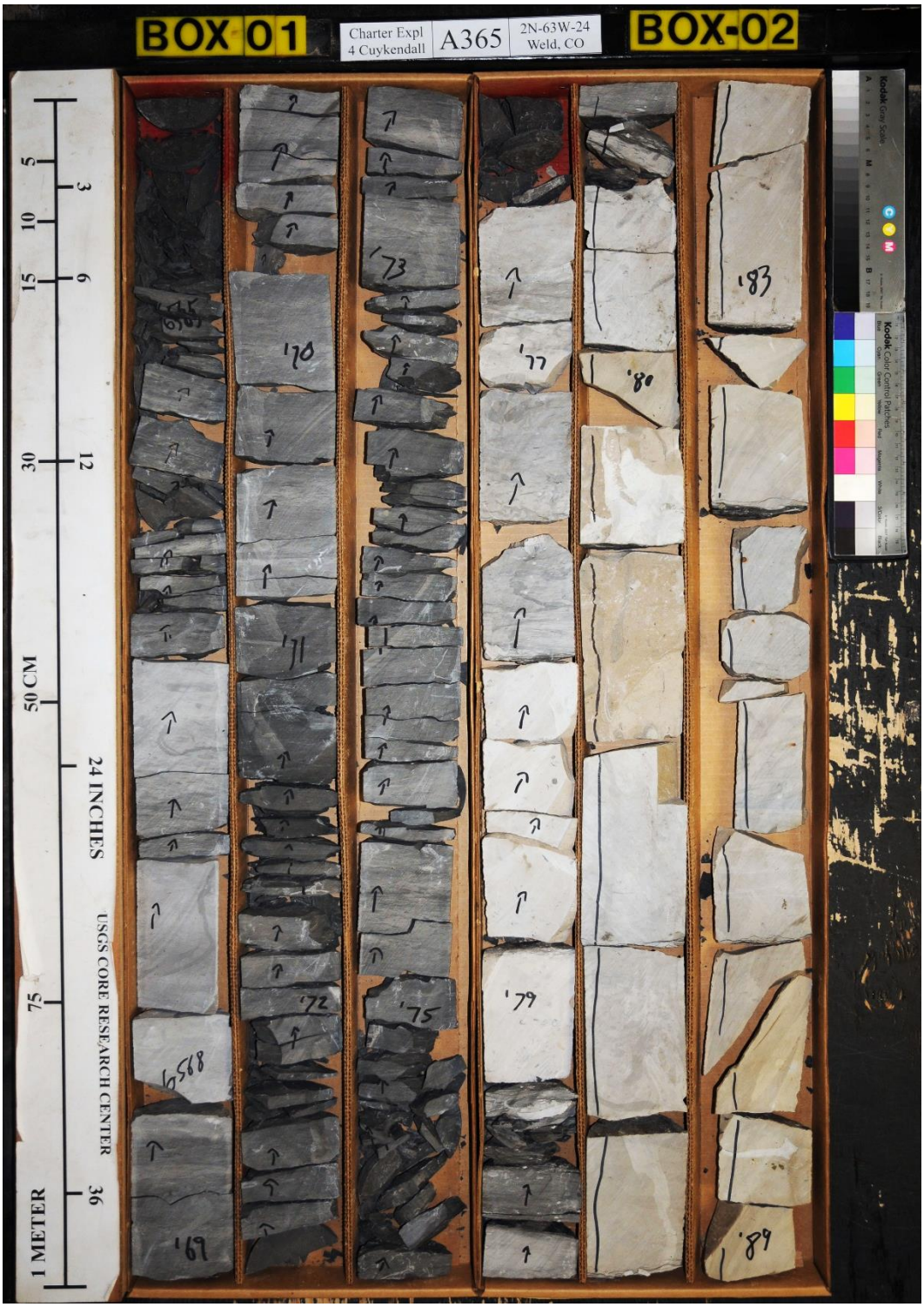

Figure 2. Core photo of the Niobrara Formation in the Charter Exploration, #4 Cuykendall (2N-63W-24, Weld County, CO) taken from the public domain (http://my.usgs.gov/crwc/core/report/8443). Photo shows color variation between chalky (lighter) and marly (darker) lithofacies.

taken from one well in the northeastern portion of the DJ Basin and two wells in the southwest Piceance Basin.

CHAPTER 2: GEOLOGIC SETTING

Cretaceous sediments in the Denver-Julesburg and Piceance basins were deposited in the Western Interior Seaway (WIS), a large asymmetric foreland basin that stretched from the Gulf of Mexico to the Arctic and reached up to 1600 km (~1000 miles) at its widest part (Weimer, 1983). The DJ and Piceance basins were created in the latest Cretaceous when the Laramide Orogeny split the Western Interior Basin into a series of smaller intermontane basins.

Clastic sedimentation in the WIS was dominated by material shed eastward from the topographic highs of the Cordilleran Orogenic Belt (Pollastro and Scholle, 1986). These clastic sediments dominate much of the Niobrara deposits in the present Piceance Basin. In contrast, the land mass east of the WIS had relatively low relief and clastic input westward was restricted to more proximal shoreface localities (Longman et al., 1998). In the eastern portion of the Western Interior Basin, more carbonate-rich sediments dominated the Late Cretaceous due to a combination of this minimal siliciclastic input and high primary productivity likely caused by mixing of arctic and tropical waters in the area (Longman et al., 1998). Deposition of the Niobrara Interval in both basins is considered to have occurred during the Upper Turonian through lowermost Campanian from 89.5 to 83 Ma (Ball et al., 2010; Sageman et al., 2014) during a major relative sea-level rise inferred to be on the scale of a second order transgressive-regressive cycle (Weimer, 1983; Longman, 1998).

Denver-Julesburg Basin Niobrara Sedimentation

The Niobrara Formation in the DJ basin is divided into two main members, the basal Fort Hays and the overlying Smoky Hill members. The Fort Hays Member, approximately 10 m (~33

ft) thick, unconformably overlies the Codell Sandstone Member of the Carlile Shale. The Fort Hays represents some of the purest chalks in the Western Interior Basin (Pollastro and Scholle, 1986) with deposition occurring during a major marine transgression. The Smoky Hill Member is a series of chalks and marls with a total thickness of approximately 80m (~260 ft). Variations in lithology are controlled by varying relative amounts of terriginous input and pelagic carbonate input. The Smoky Hill is overlain by the Pierre Shale throughout the DJ Basin.

The Niobrara in the DJ Basin is characterized by oscillations of varying calcium carbonate content in the form of chalks, chalky marls, and marls. The characteristic lithologic oscillations are recognized at a variety of scales. Millimeter-scale variations of single beds or laminae are seen in thin section. Centimeter and meter-scale variations are best recognized in core and outcrop. Decameter scale chalk to marl transitions, informally designated A,B,C, and D by several researchers (Scott and Cobban, 1964; Lockridge and Scholle, 1978; Longman et al., 1998), are seen in core and gamma ray and resistivity logs (Rogers, 2012; Milne and Cumella, 2014; Cumella et al., 2014).

During Niobrara deposition in the eastern portion of the WIS (Colorado, Kansas, and Nebraska) a large, generally shallow shelf and slope prevailed with water depths thought to fluctuate between 30 and 150m (Kauffman, 1977). Periods of incision or subaerial exposure are thought to have occurred periodically (Weimer, 1983). Macrofaunal assemblages, primarily *Inoceramus*, suggest a soft to soupy substrate (Hattin, 1981) comprising both fine-grained siliciclastic sediment and carbonate ooze dominated by coccolithophore debris and, to a lesser extent, benthic and planktonic foraminifera (Kauffman, 1977; Hattin, 1981; Pollastro, 1981). SEM analysis in both two and three dimensions has shown clay particles were deposited both

as single grains as well as floccules (Michaels, 2014). Despite suspension settling likely being the dominant form of sedimentation, these floccules may be related to varying levels of wave or current energy as described in flume experiments by Scheiber (2010). Support for these types of energy changes include observed scour and cross bedding in thin section (Michaels, 2014) (Fig. 3).

A major sedimentary element in the Smoky Hill member is peloidal grains identified by Hattin (1975, 1981) as fecal pellets likely derived from small planktonic organisms such as copapods (Hattin, 1975). Pellet concentrations vary both stratigraphically and laterally across the basin (Hattin, 1975; Longman et al., 1998; Burt, 2014; Michaels, 2014) with the greatest concentrations occurring in the chalkiest facies. Microprobe elemental maps of peloids show they have very high calcium concentrations within the grains in both chalk- and clay-dominated matrices (Michaels, 2014; Fig. 4) with little, if any siliciclastic component. Both chalky and shaley lithologies can appear bioturbated or laminated containing both cryptic bioturbation attributed to meiofauna such as nematodes (Longman, 1998; Hattin, 1981; May, 2013) and larger burrows likely made by worms and other burrowing organisms (Fig. 5).

Piceance Basin Niobrara Sedimentation

The coeval Upper Turonian to Santonian deposits in the Piceance Basin retain much of the characteristic lithologic oscillations of the Niobrara in the DJ Basin but with a distinctly more siliciclastic signature. The Niobrara Member is referred to both independently and as a member of the Mancos Shale in the Piceance Basin (Rogers, 2012; Cumella et al., 2014). The calcitic shales and marls of the Niobrara member overly the Frontier and Montezuma Shale and

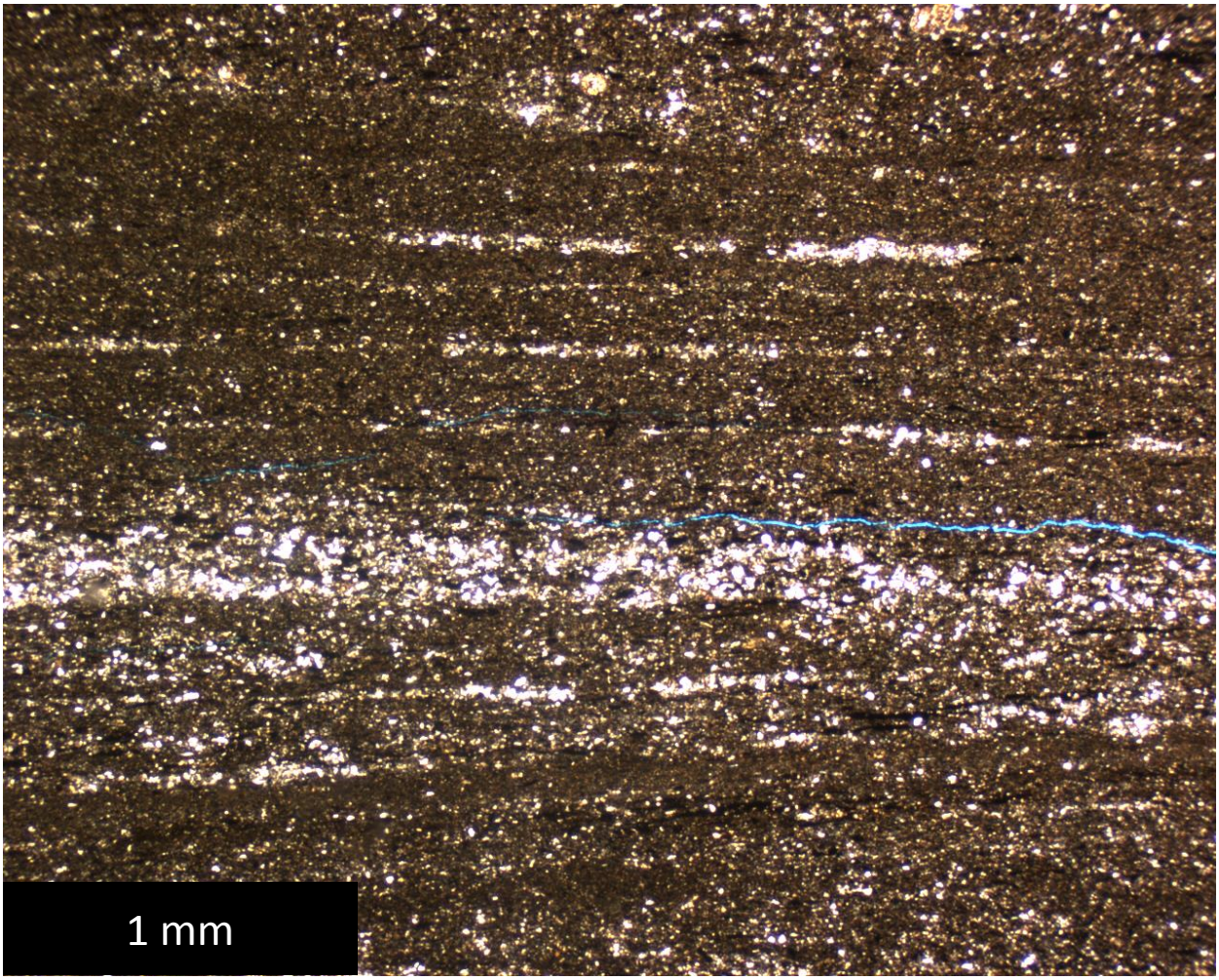

Figure 3. Photomicrograph of DJ Basin marl sample showing very low angle cross-lamination of silt- and clay-rich laminae. The laminations, once an allowance for compaction is made, probably indicate transport of the fine-grained material in clay ripples. White spots are laminae of concentrated foraminifera shells.

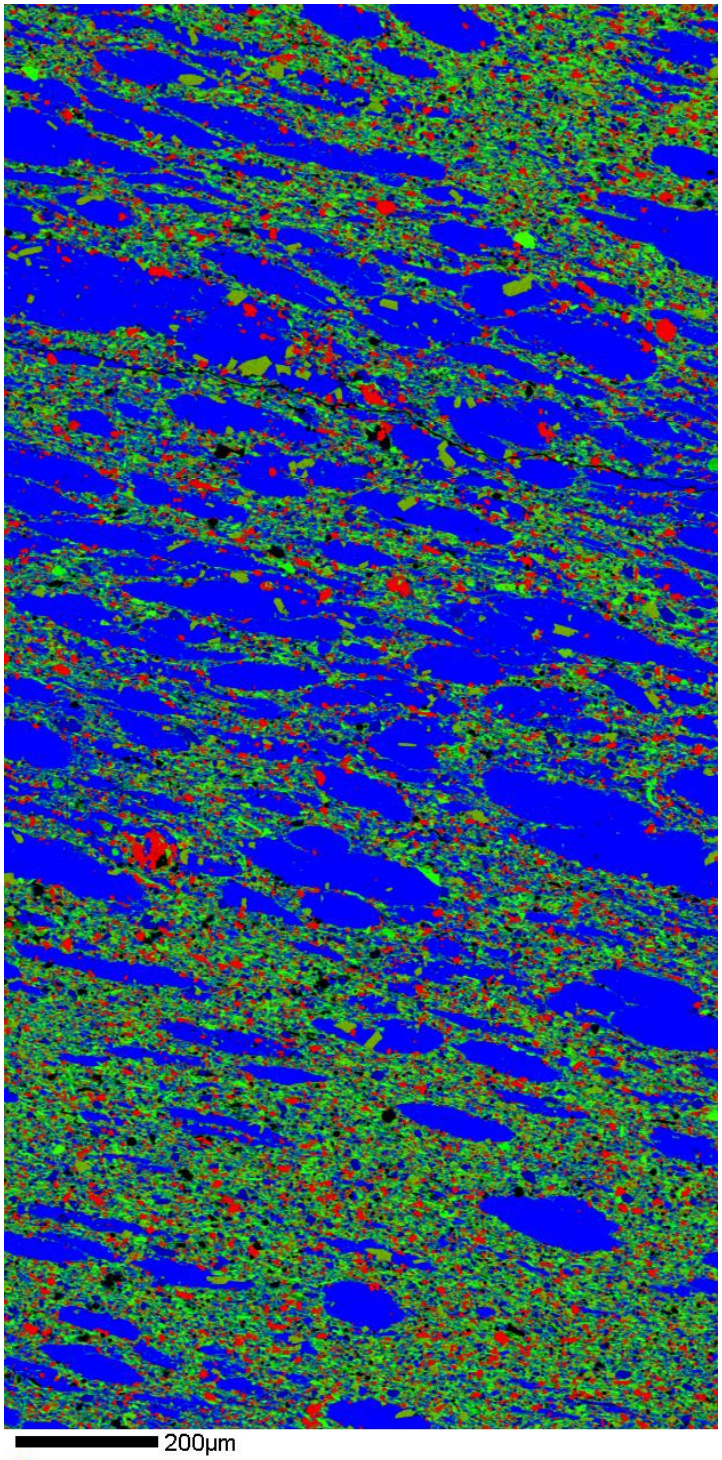

Figure 4. Composite elemental microprobe map for silicon (red), aluminum (green), and calcium (blue) for a marl sample, well #5, 7638, Piceance Basin. Blue ovals are calcite-rich peloids, red is quartz silt, and the orange and green is a clay-rich aluminosilicate matrix. Stratigraphy runs from top-right to bottom-left.

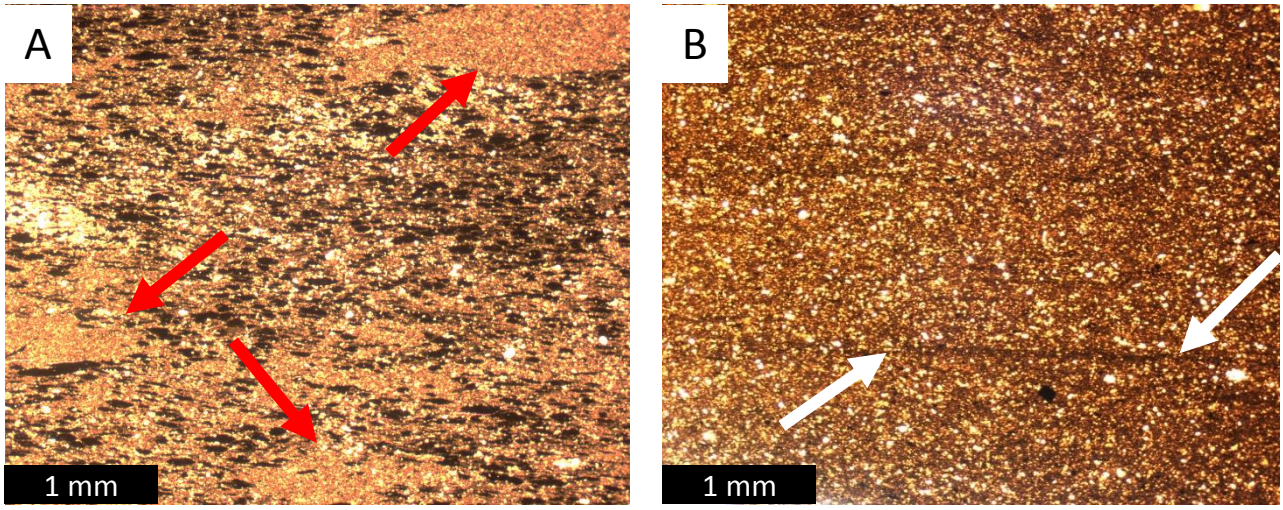

Figure 5. Two photomicrographs showing variations in types of bioturbation observed. Photo A from well #4, 10380, Piceance Basin, shows three distinct burrows in a peloid-rich substrate highlighted by red arrows. Photo B from well #5, 8376, Piceance Basin, shows an example of cryptic bioturbation that has overprinted almost all evidence of original bedding patterns. The cryptic burrows are small – 10s of micron in size – and individual burrows are not visible. Their presence though is suggested by the faintness and disruption of physical laminations (white arrows).

underly the Mesaverde Group. The basin dips steeply on the eastern edge as it reaches the structural pinchout at the Grand Hogback and shallows towards the west opening up into the Uinta Basin in Utah. Thickness of the upper Cretaceous Niobrara in the Piceance Basin ranges from its thickest point in northwest Colorado at 520 m (~1700 ft) to the thinnest at less than 150m (~500 ft) in the southwest portion of the basin (Rogers, 2012; Cumella et al., 2014). Deposition of the Niobrara in the Piceance was shown by Ball et al. (2010) to have begun at 89.3 ± 1.0 Ma based on ammonite zonations, which is contemporaneous with the Fort Hays Member in the DJ Basin.

Primary clastic provenance derived from the Cordilleran Orogenic complex to the west of the WIS, a steeper topographic gradient into the seaway, rapid subsidence, and high detrital influx led to greater siliciclastic dilution of both carbonate and organic material in the Piceance Basin relative to the DJ Basin (Longman et al., 1998; Rogers, 2012; Cumella et al., 2014). This dilution corresponds to a shift in the lithologic oscillations to marls and shales rather than the chalk-marl oscillations seen in the DJ Basin. In the central portion of the WIS, it is suggested there existed interfingering of these sediments where much has now been eroded due to Larimide mountain building (Pollastro and Scholle, 1986).

Like the Niobrara of the DJ Basin, oscillating sub-units in the Piceance lack a formal member designation. Rogers (2012) separated the Niobrara throughout the Piceance Basin into 12 distinct, correlatable units based on well-log signatures separated on surfaces mostly inferred to correspond to marine flooding surfaces. Log character and inferred lithologies are explained in detail in Rogers (2012) and will be addressed herein in correspondence to sample

descriptions in Chapter 4. Samples incorporated in this study from Burt (2014) are from Roger's Unit 8 (the Tow Creek Bench), a primary petroleum target interval in the basin.

Cyclostratigraphy and Other Explanations for Lithologic Variations

Several explanations exist for the rhythmic oscillations between chalk and marl facies within the Niobrara of the DJ Basin. Kauffman (1977) invoked global eustatic cyclothems generated by continent-scale tectonics and smaller, more localized, tectonically-driven eustatic oscillations throughout the Cretaceous as forcing agents to have drove changes in sedimentation, salinity, water depth, water temperature, and faunal assemblages. Another explanation put forth by Pollastro and Scholle (1986) is that these cycles reflect changing degrees of seawater oxygenation and thus variable primary productivity, which in turn changed relative concentrations of terrigenous and carbonate sediment. The periodic shifts in the mixing of warm, calcium-rich tropical waters and colder arctic waters has also been suggested to have impacted primary productivity and thus calcium deposition (Longman et al., 1998). Most recently, Locklair and Sageman (2008) suggest that orbital forcing on the scale of Milankovitch cycles drove climatic changes leading to varying rates of erosion and siliciclastic dilution. Whether any or all of these factors play a role in the lithofacies variation, the characteristic oscillations in the Niobrara, in both the DJ and Piceance Basins, play a major role in the structure of the petroleum systems. This study attempts to tie these lithologic changes to more specific fabric elements and their impacts on the pore systems of the formation.

Diagenesis

The diagenesis of the Niobrara chalks have been discussed at length by Scholle (1977), Scholle and Arthur (1980), Hattin (1981), Scholle and Pollastro (1985); Pollastro and Scholle (1986), and Longman et al. (1998). Comparisons have been drawn between the chalks of the Niobrara Interval and those of the Austin Chalk and the North Sea chalks with the conclusion that not all chalks behave similarly at the point of, and after deposition (Scholle, 1977). Even within the Niobrara, major differences in the relative impact of neomorphic reactions, physical compaction, and chemical compaction are evident with burial along east to west transects. Based on the work of Hattin (1981) who examined the Niobrara in Western Kansas, physical compaction within the first several thousand feet played the most significant role in the loss of roughly half of original porosity. He argued that the low-magnesium calcite composition of cocoliths and forams, the most stable form of calcite at deposition, underwent little chemical alterations. However, within the DJ Basin, where burial depths of the Niobrara are commonly greater than 7000 ft (~2100 m) it has been observed (Pollastro and Scholle, 1986; Michaels, 2014; Fig. 6) that significant calcite cementation and overgrowth imparts a major impact on the development of the pore systems in both chalky and marly facies. These observations, made with SEM techniques, are supported by a well-log porosity with depth plots that show average porosities of approximately 10% at oil-producing DJ basin burial depths (Scholle, 1977; Scholle and Halley, 1985). In addition, an increasingly negative $\delta^{18}O$ ratio associated with the dissolution of marine biogenic calcium carbonate and calcite re-precipitation at high temperatures suggests at least some amount of chemical compaction affecting the loss of porosity with depth (Pollastro and Scholle, 1986).

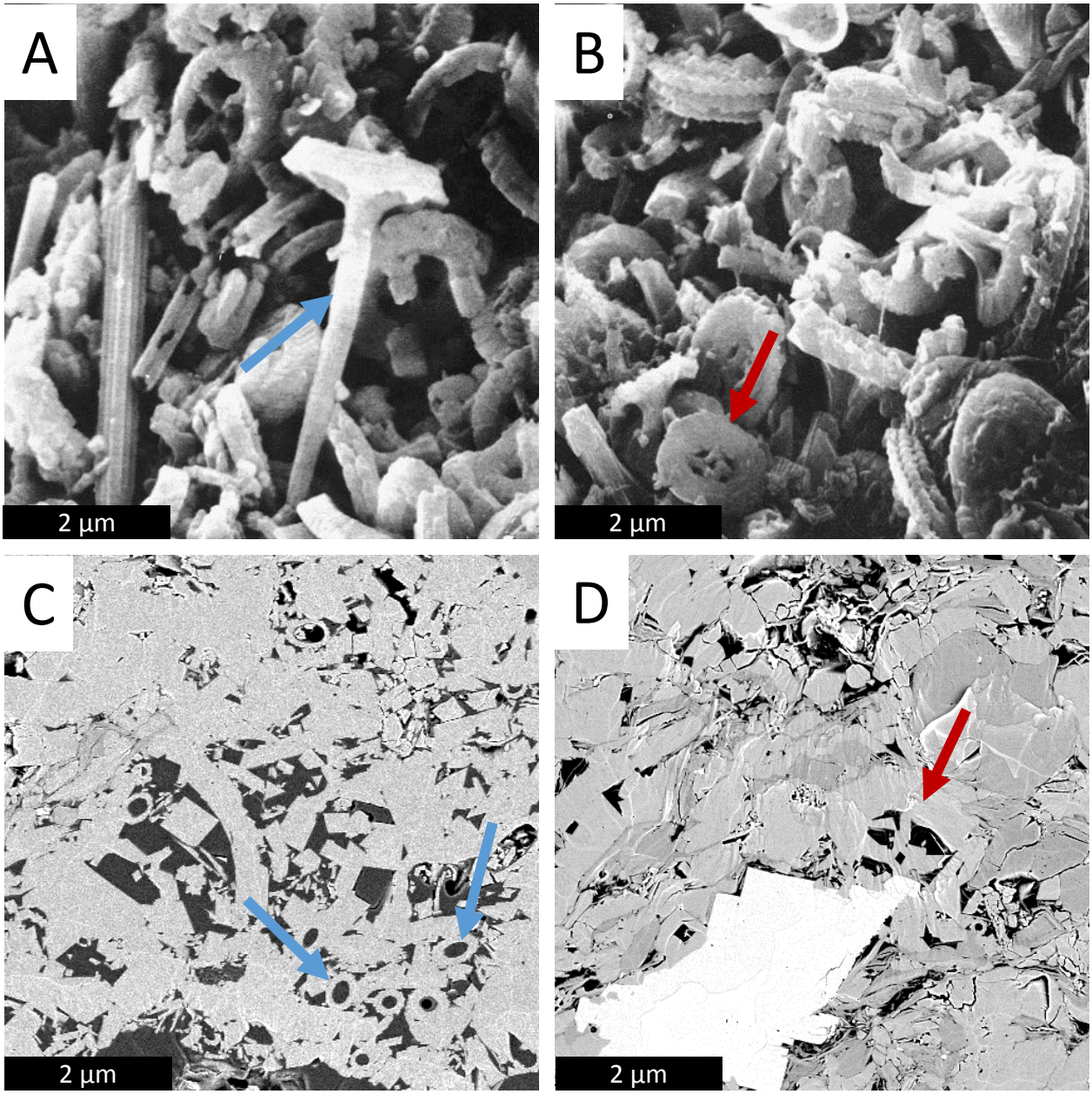

Figure 6. Pre- and post-compaction comparison of Niobrara chalk material in Yuma County, Colorado (A and B) and the DJ Basin, Colorado (C and D). Photos A and B are SEM images of the Niobrara Formation at 1680-1690 feet and 1720-1730 feet burial (from Lockridge and Scholle, 1978). Photos C and D are from the Timbro core and had maximum burials of at least 5758 and 5835 feet respectively. Blue arrows show coccolithophore spicules and red arrows show individual pieces of coccolith shells. In both examples from Yuma County, coccolith debris remains largely intact and generally uncemented. In image C spicules are seen overgrown by calcite rhombs and surrounded by migrated organic material. Image D shows a coccolith plate encased in calcite cement.

Less research has been done on the diagenesis of the Niobrara member in the Piceance Basin, but like in the DJ Basin, deep burial appears to have driven extensive compaction of the silts and shales. Burt's (2014) images of marls illustrate the significant role of both mechanical compaction and calcite cementation in pore occlusion.

The complex nature of the lithologic variations in the Niobrara at scales from millimeters to decameters have, no doubt, had a major impact on the petroleum systems in both the DJ and Piceance Basins.

CHAPTER 3: METHODS

Sampling

Samples from one DJ and two Piceance basin cores were used in this study. The DJ Basin material is from the Timbro well (9N, 58W, API# 0512333305) which had been previously sampled by Michaels (2014). Michaels collected 28 samples from the A-marl zone through the C-marl zones. Those samples and 14 additional samples were used for this study, with the 14 additional samples collected to increase sampling density and add material down to the base of the Smoky Hill Member (D-chalk). The two Piceance Basin cores used for this study were provided by sponsoring companies and do not lie within the public domain; they are referred to as Well #4 and Well #5 as established by Burt (2014). Sixteen samples in the #4 well covered the 385 ft (117.2 m) stratigraphic interval from the top of the Niobrara member to the base of the lower Tow Creek Bench landing zone studied by Burt (2014). Twenty-seven samples from the #5 well covered the 755 ft (230.2 m) interval from that landing zone to the base of the Niobrara member. As described in Michaels (2014) and Burt (2014), sampling relied on proprietary core descriptions done on a roughly quarter-foot scale for lithology, gray-scale, grain-size, degree of bioturbation, sedimentary structures, and abundance of other visible constituents.

Elemental compositions of all 85 samples were acquired through handheld x-ray fluorescence (XRF) analysis using a Thermo Scientific NITO XL3t 950 at half foot scale for the Timbro and on sampled billets for wells #4 and #5. Details as to instrument calibration and calculation of elemental enrichment concentrations relative to the standard North American shale standard are in Burt (2014). Lithofacies were defined by the relative weight percentages of Ca versus Al+Si, three elements that comprised >82 weight percent of all samples. In that

samples. In that distinction, Ca is assumed to be a proxy for carbonate minerals (calcite, i.e., the biogenic component) and Al+Si a proxy for quartz and all aluminosilicates (i.e., the detrital component). The 85 samples plot consistently along a shale to chalk continuum and are subdivided into lithologies using a modified classification from Pettijohn (1975). Chalks are defined as greater than 85% Ca, marly chalks as between 85% and 60% Ca, marls are between 60% and 40% Ca, marly shales are between 40% and 15% Ca, and shales are less than 15% Ca.

Petrographic thin sections were cut from each of the 85 collected samples. The 28 Timbro samples collected by Michaels (2014) were vacuum impregnated with blue dyed epoxy and then mounted and trimmed to 30 micron thickness by Spectrum Petrographics (www.petrography.com/). Well #4 thin sections were provided by the well's operator; they had been prepared using a red dyed epoxy by Terratek, Inc. Thin sections from the 14 new Timbro and all Well #5 samples were impregnated with blue dyed epoxy, mounted onto glass slides, trimmed to 30 microns, and polished in the Department of Geological Sciences, University of Colorado, Boulder. All thin sections were examined and imaged using an Olympus BH-2 petrographic microscope and attached AmScope FMA050 digital camera at 400x magnification. Photomicrographs were then analyzed for bioturbation, sedimentary structures, and relative abundances of clay-sized material, silt-sized material, and sand-sized material (foraminiferal tests and peloids). Six microfacies were then created based on the modal estimates of the three size classes.

Sample Preparation and Imaging

The lithofacies and microfacies groups established by the elemental and petrographic analyses were used to high grade 21 samples for FE-SEM (field emission scanning electron microscopy) imaging. The 21 thin sections associated with high-graded samples were polished, carbon coated, and mapped for carbon, calcium, silica, and aluminum using a JEOL-8600 electron microprobe at the Department of Geological Sciences, University of Colorado, Boulder. Samples were run at 15 kV, 150 nA, and a 1.6 µm spot size with 28 microsecond dwell time per spot. The resulting four images were adjusted for intensity and stacked to create a RGB color image in ImageJ (imagej.nih.gov/ij/). These color images were then analyzed using the image analysis software Avizo 9 for relative area proportions of calcium, silica, aluminosilicate mixtures (Al +Si), and other material (undifferentiated pyrite and detrital organic matter). The microprobe elemental data were then used as a mineralogoical proxy for determining elemental distribution throughout each sample's fabric elements. The area percentages calculated from the elemental maps in Avizo 9 were used directly in calculating matrix carbonate by subtracting the area of peloid material, assumed to be completely calcite, from the total calcite area in the entire field of view. Relative proportions of Ca, Si, and Al did not always agree between the microprobe and XRF analysis, probably due to the differences in volumes of investigation (~2 mm^2 for microprobe versus cm^3 for the XRF) and the fact that not all XRF data were collected from the thin-sectioned samples. If chemical assemblages varied by more than 20% for any element between the two datasets, values derived from the microprobe analysis were used for lithologic classification because the microprobe analyses were done on the same material as that analyzed for pore systems by FE-SEM. This step was only necessary in two of the 21 samples.

The 21 samples were split into two groups for FE-SEM analysis. Group A consists of 13 samples (six from Timbro, four from Well #4, and three from Well #5). Group B included the remaining eight samples (four from Timbro, one from Well #4, and three from Well #5). Group A samples were prepared and imaged by Whiting Petroleum Corporation in Denver, CO and group B samples were prepared and imaged at the USGS facility in Lakewood, CO. Overall preparation and imaging was similar for each sample set with only the operator, FE-SEM models, and some imaging and preparation techniques varying. All samples were cut to roughly 10x10x10mm cubes and mounted to aluminum pedestals using epoxy with the top face perpendicular to stratigraphic laminations. The top surface was then mechanically polished with 1µm diamond grit and allowed to dry before ion polishing in an Ar-mill. Group A samples were milled in a Fischione Model 1060 for 20 minutes at a 4.0 degree angle followed by a 3.0 degree angle for 30 minutes followed by a 2.0 degree angle for 15 minutes all at 5 kV and 50-60 µA. After milling, each sample in group A was imaged in a FEI Helios NanoLab 650 Dual Beam FE-SEM at 40 nm pixel resolution. A total of 240 images with horizontal field width (HFW) of 61.44µm were then tiled together in a 10x24 image mosaic (Fig. 7). Group B samples were also Ar-milled in a Fischione Model 1060 but for 150 minutes at 2.0 degree tilt at 4.0 kV and 86.9 µA. Samples were then imaged at high vacuum in a FEI Quanta FEG 450 FE-SEM. Overview images of the Ar-milled surface were taken at approximately 400x magnification (horizontal field of view of ~ 1.0 mm; Fig. 8), then three randomly selected zones were imaged from within the larger initial imaged area. Those three zones were documented with a 5x5 photo mosaic taken at a 29.4 nm pixel resolution and HFW of ~ 59.7 µm. The image working distance for both groups was ~6 mm.

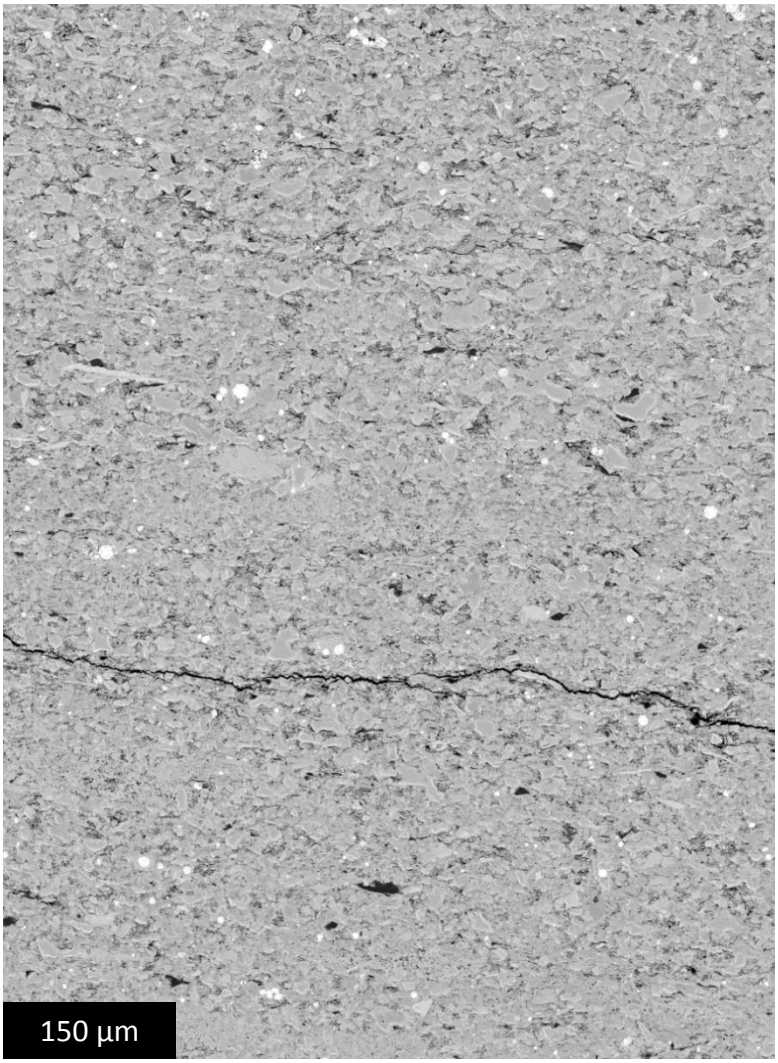

Figure 7. Composite image of 240 backscattered SEM photos from well #5, 7750, Piceance Basin. Mosaic consists of 10 images across by 24 images down.

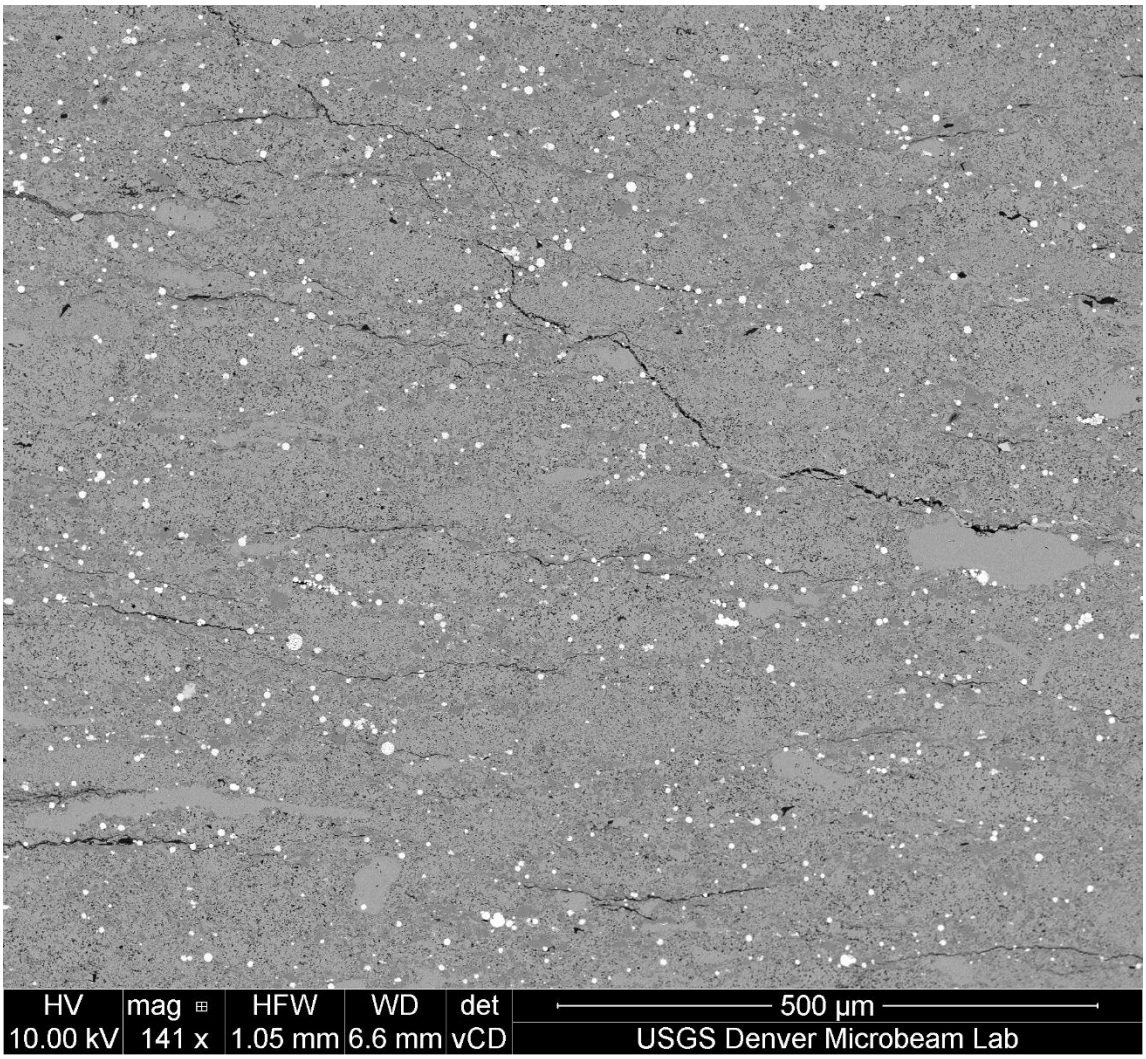

Figure 8. Backscattered SEM overview photo from group B (USGS) used to establish areas for higher resolution image mosaics. Photo shown for Timbro well, 5680.7.

For both sample groups, three five-by-five image groups were selected at random from each sample and stitched together before being cropped down to 150 µm by 150 µm squares for porosity analysis (Fig. 9). This resulted in 63 fields of view (FOV) from the 21 samples, with each FOV covering 22,500 μm^2. Due to differences in the images' focus between group A and group B samples, the group A samples display greater resolution of smaller objects than group B samples.

Image Analysis

Image analysis and object segmentation of the 63 FOVs was completed in Avizo 9. Manual contrast and brightness adjustments were first done as needed in Adobe Photoshop. Then, all images were smoothed to remove imaging artifacts with a single non-local means filter in Avizo 9. Organic material visible in the images was manually segmented into two groups, detrital and migrated. Detrital organic material was identified by shape (generally highly elongate or blocky and jagged), size (far larger than open pores), and gray-scale, depending the sample on sample, generally between light gray siliciclastic material and dark gray open porosity (Fig. 10). The detrital organic matter was not included in pore identification. Migrated organic material was identified where it fills pre-existing pores in the rock and can be seen through a gray-scale contrast with open porosity (i.e., it is not as dark as open pores; Fig. 11). Because migrated organic material fills pores already present in the rock, it is included in the calculation of total initial (pre-migration) porosity when identified. After manual selection of detrital organic material and pyrite, concentrated chalky objects composed of broken cocoliths (fecal pellets or chalk-filled burrows, which will be collectively referred to herein as peloids) were also manually selected (Fig. 12). With material already assigned as migrated hydrocarbons

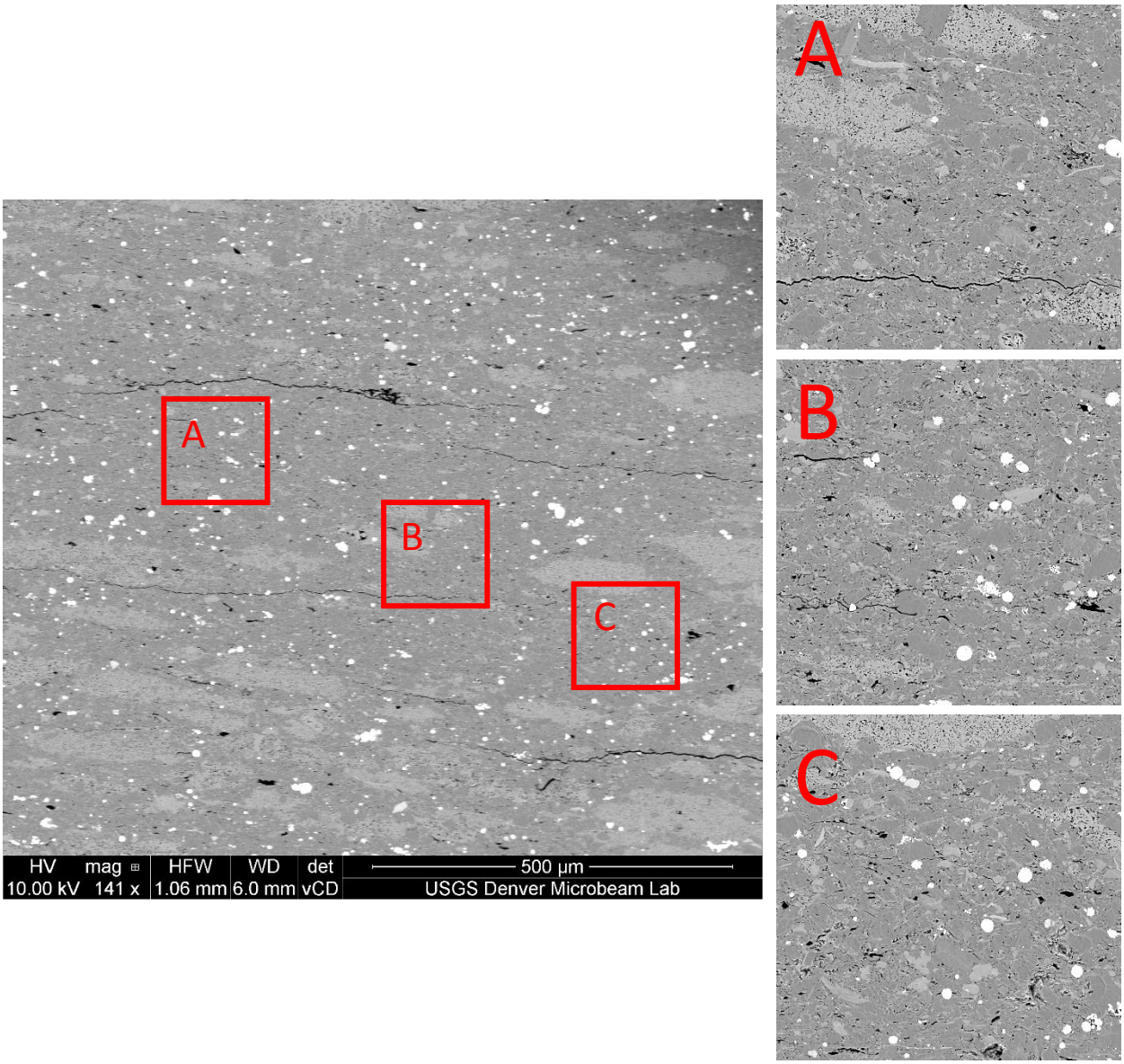

Figure 9. Overview backscattered SEM image from well #5, 7645, Piceance Basin, showing randomly selected positions of the three higher resolution 150x150 µm fields of view (FOVs).

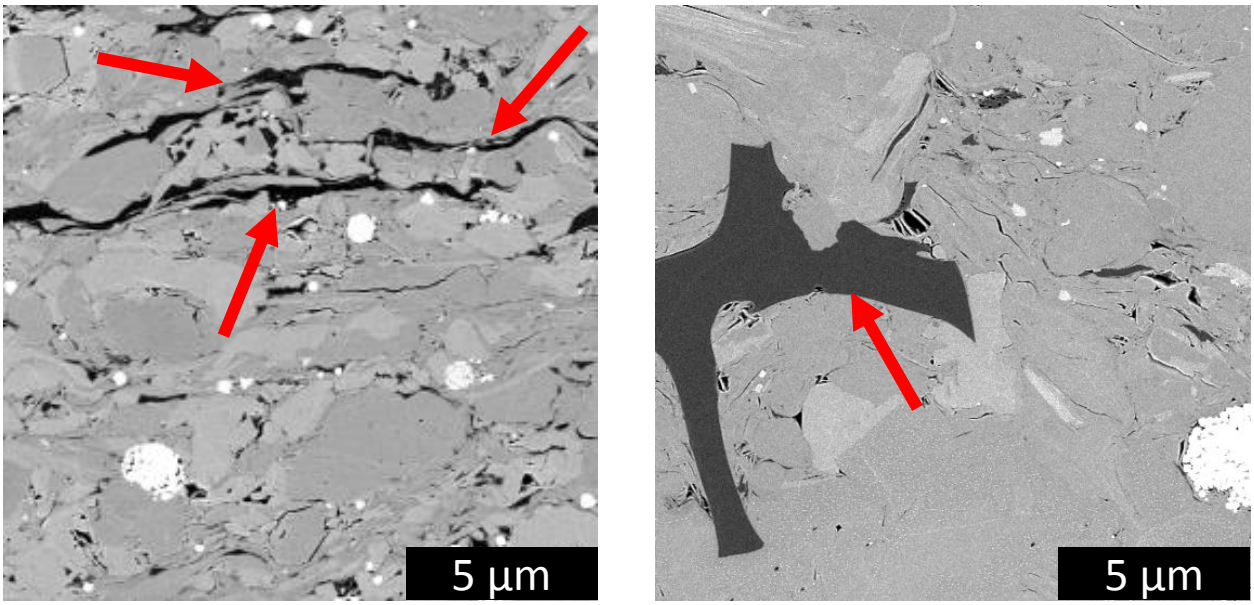

Figure 10. Backscattered SEM images of detrital organic material (red arrows) in the DJ Basin (left; Timbro well, 5666) and the Piceance Basin (right; well #4, 10010). The DJ sample shows long, stringy organic material and the Piceance sample shows a blocky, jagged piece of organic material.

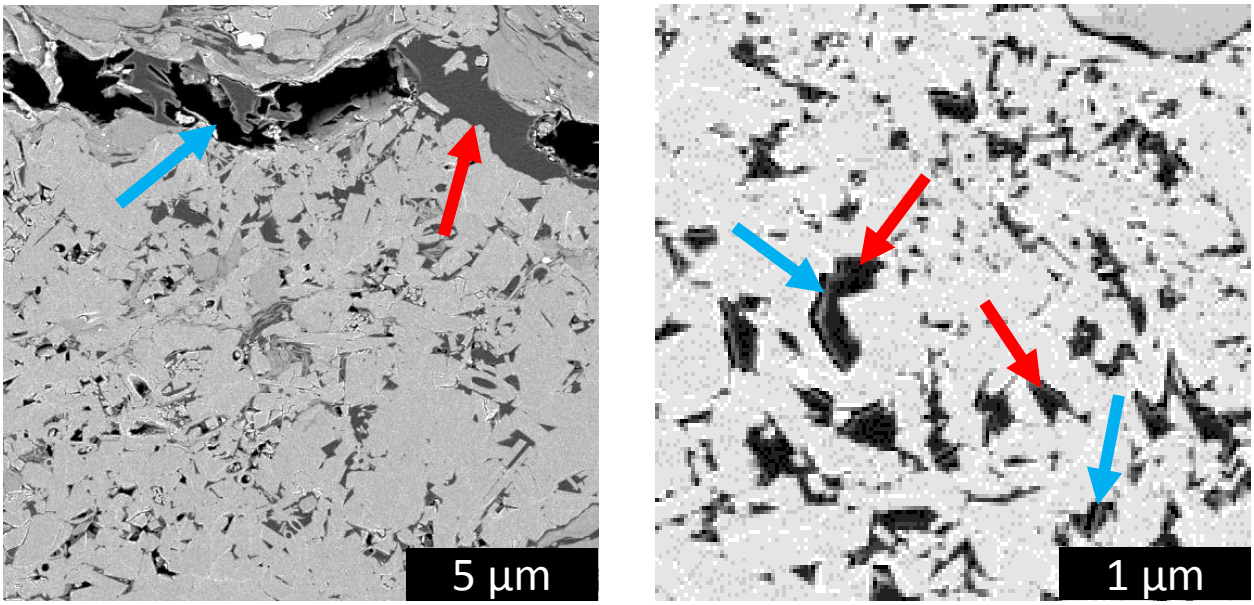

Figure 11. Backscattered SEM images of migrated organic material in the DJ Basin (left; Timbro well, 5799) and Piceance Basin (right; well #5, 7750). Red arrows highlight organic material currently occupying once open pore and blue arrows point to remaining, currently porosity. In both cases still open pores are only slightly blacker than the migrated organic matter.

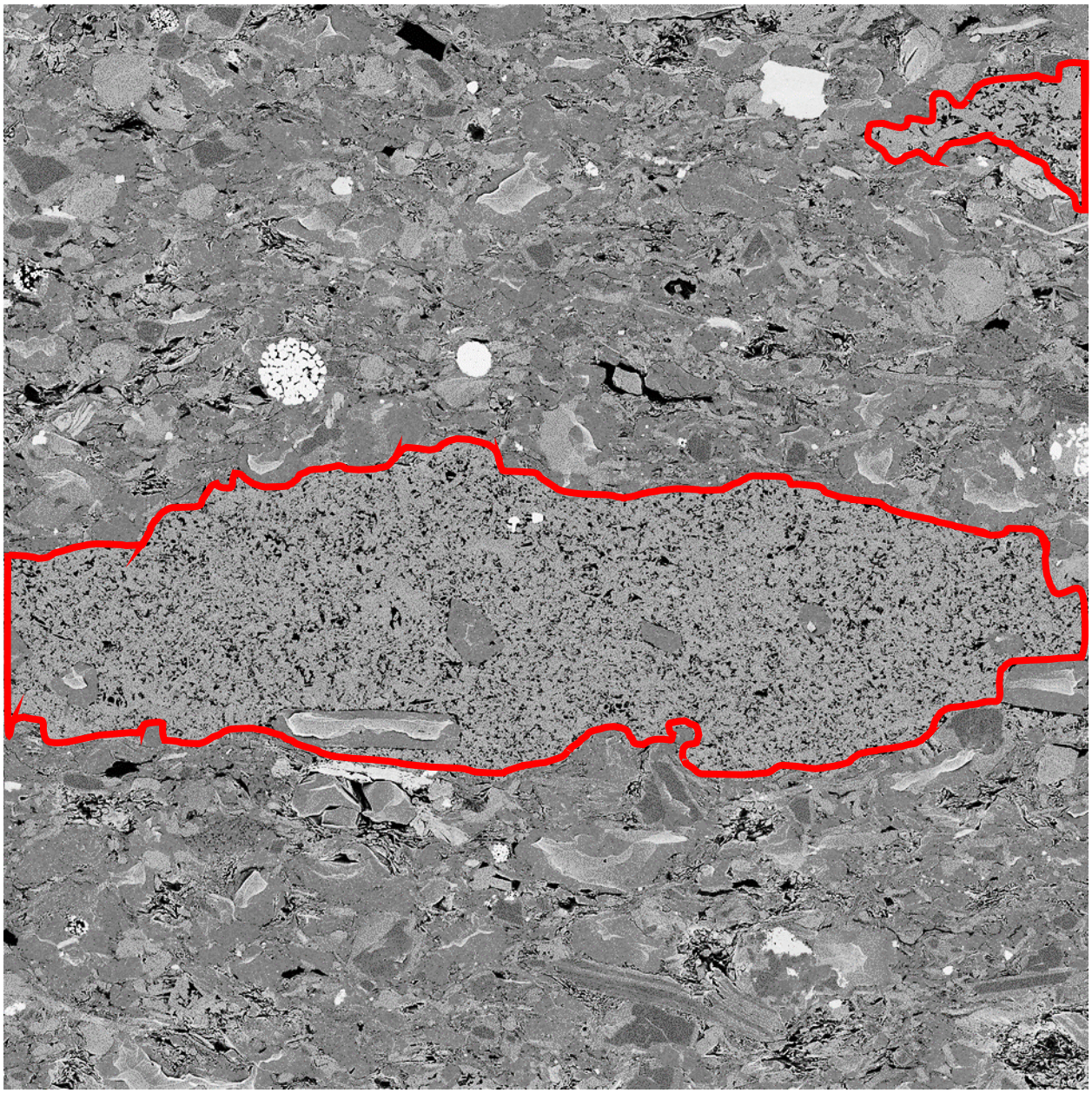

Figure 12. Backscattered SEM image of a marl field of view from well #5, 8000, Piceance Basin. Peloids are highlighted by the red outlines; remainder of the image is interpreted to be matrix. Peloids were segmented manually so pores could be identified and characterized by the fabric element in which they occur (i.e., peloid or matrix). Horizontal field of view is 150 µm.

locked, gray-scale thresholding was then used to automate pore identification in both matrix and peloids (Fig. 13). Once segmented, total (pre-migration) porosity, pore sizes (area, width, and equivalent circular diameter), pore shapes (anisotropy), and pore orientations (long axis' angle relative to images' horizontal axis) were collected for each pore object and totaled for each of the 21 samples (Fig. 14). Size, shape and orientation data was also collected for current porosity (the pores that remain open after partial or total occlusion by migrated organic material in seven samples (five Piceance and two DJ) where images had adequate contrast between these two materials (Fig. 15).

Segmented objects that fit the proper gray-scale cutoff and were of at least five pixels in size were considered pores. Objects with fewer pixels were abundant but have such a limited range of shapes that they dramatically skew any shape and orientation data. This cutoff means the effective resolution of an individual object was 200 nm (group A) and 146 nm (group B) rather than 40 nm and 29.14 nm (pixel resolution) respectively. Although the smaller objects were not used in pore size and shape analyses, they were considered for porosity analysis as they can occupy up to 3.5% of a FOV. Pores are considered based on the fabric element (peloid or matrix) by which they are surrounded. Each sample is categorized based on the lithology group and microfacies it falls into and pore size frequency is reported for total pores (matrix plus peloid pores), peloid pores, and matrix pores for each sample. For frequency analyses, pores were binned into 100 nm equivalent circular diameter ranges and 0.1 anisotropy ranges, and pore frequency was normalized to percentage of total pores in each sample.

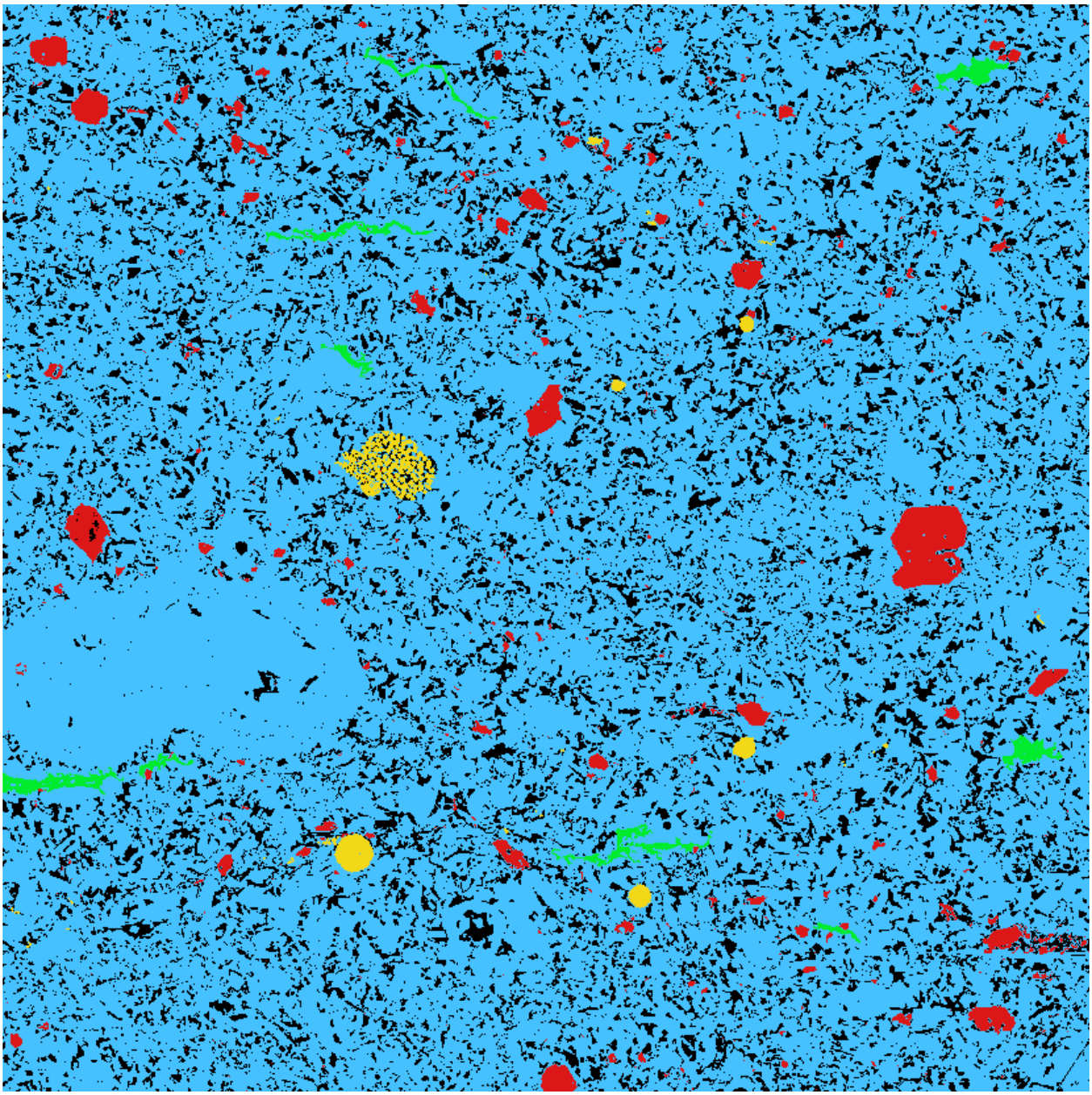

Figure 13. Backscattered SEM image of a chalk from Timbro, 5724. Image shows a combination of automatically and manually segmented color-coded objects and minerals. Threshold-derived pores are black, pyrite is yellow, detrital organic material is green, siliciclastic minerals are red, and calcite is blue. Horizontal field of view is 150 µm.

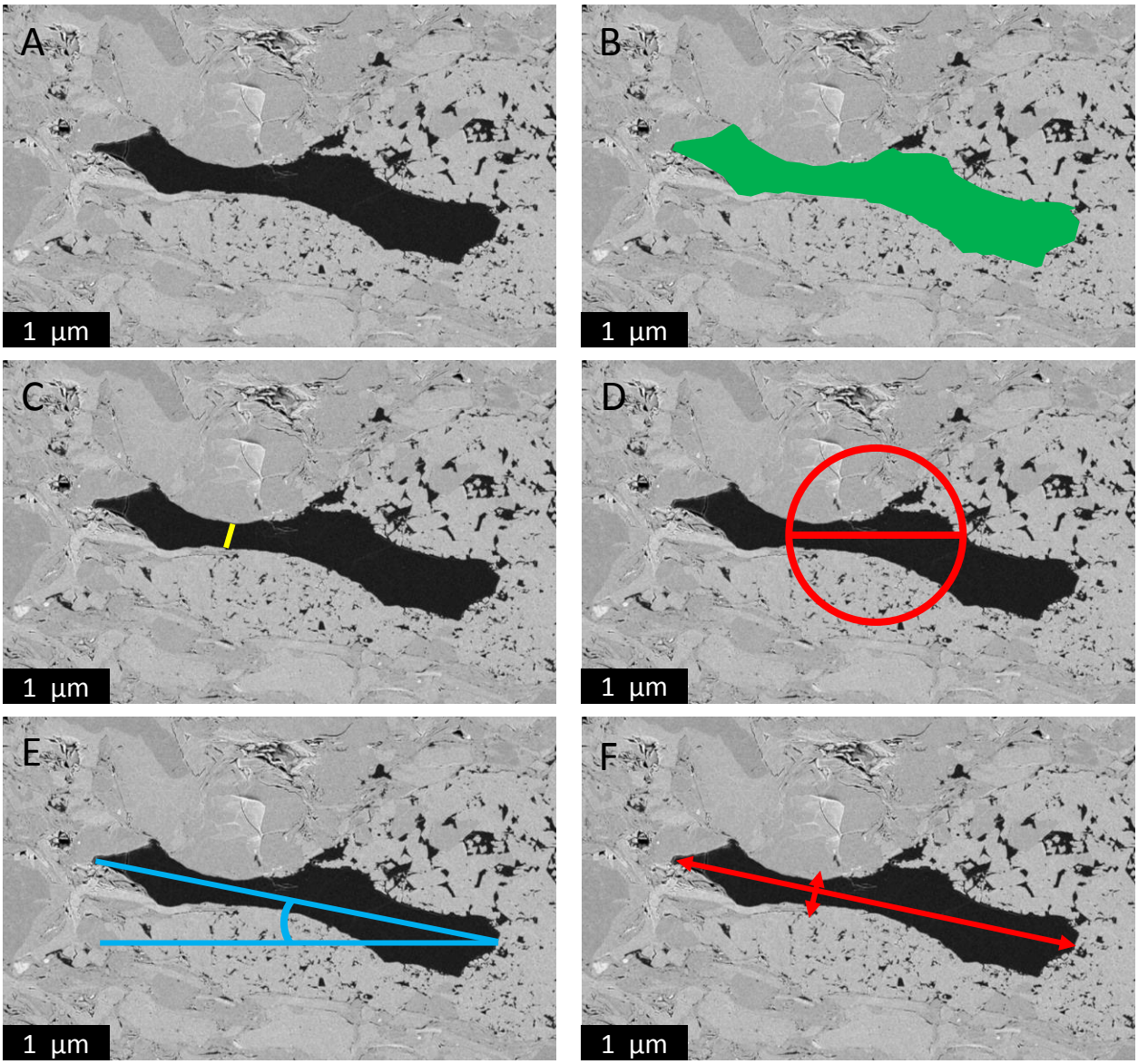

Figure 14. Set of a single backscattered SEM image depicting size, orientation, and shape parameters collected by Avizo 9. A) Image of detrital organic maceral. B) Green area depicts the segmented object's area. C) Yellow line segment shows the width measurement. D) Red circle represents the object's area-equivalent circle. The line represents the diameter of this circle (the equivalent circular diameter). E) Angle between the horizontal and longest axis of the object (blue lines) defines the object's orientation relative to horizontal. F) Ratio between longest and shortest axes (red arrows) determines anisotropy measurement.

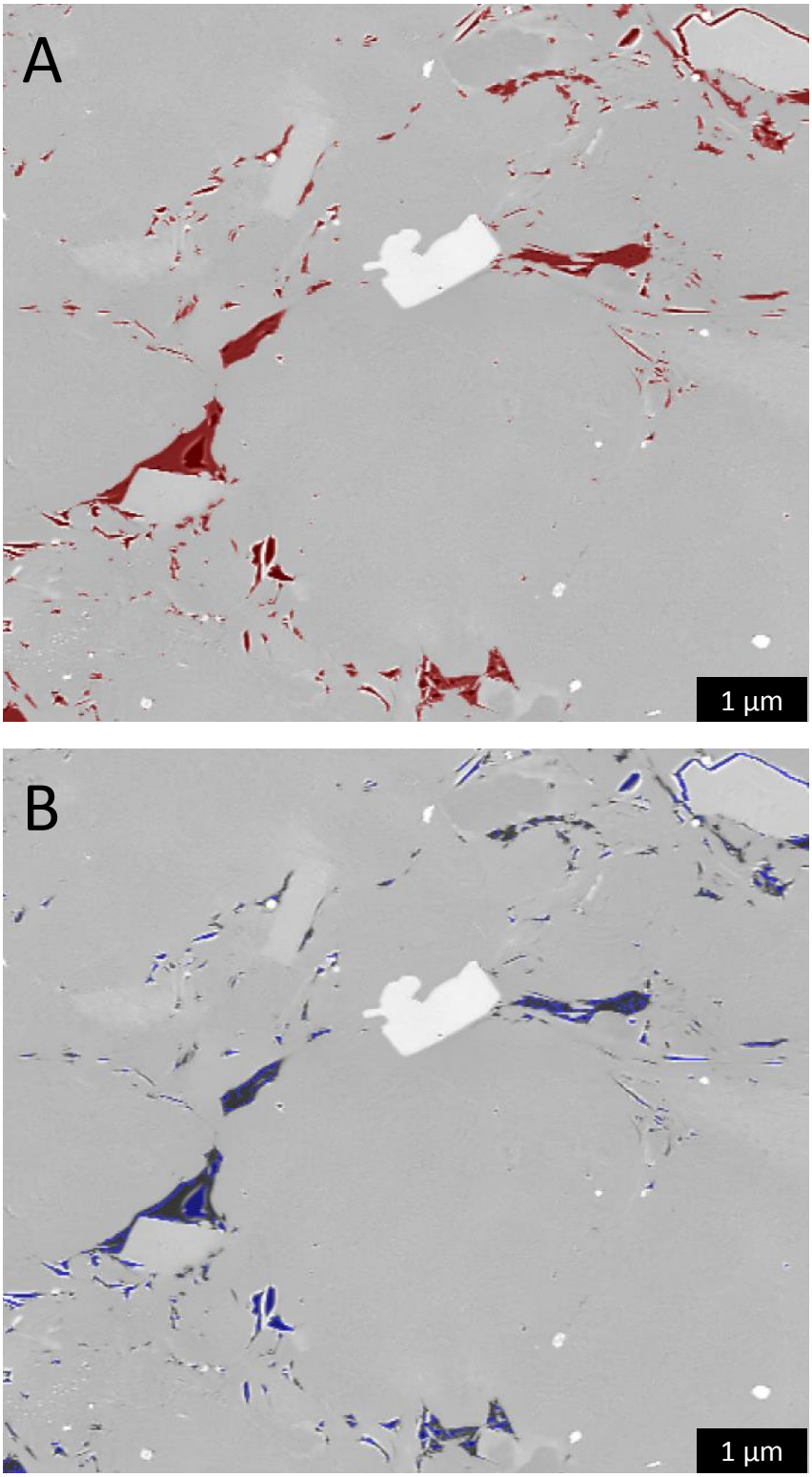

Figure 15. Two backscattered SEM images of the same field of view from well #5,10380, Piceance Basin. Photo A shows the original, pre-migration porosity filled in red. Photo B shows the current still open porosity in blue. The difference between the two is the original pores that have been partially occluded by migrated organic material.

CHAPTER 4 - SAMPLE CHARACTERIZATION

The original 85 samples from the three wells were characterized based on lithology and petrographic microfacies (Table 1). Michaels (2014) and Burt (2014) also used XRF-derived trace-element geochemistry as a characterization tool, but they found it to be inconclusive. Trace-element compositions were thus not utilized in this study. Of the original 85 samples, 21 were high-graded for Ar-milling and SEM analysis based on capturing the greatest lithologic and petrographic variability possible. Table 2 lists the 21 by basin, well, depth, lithofacies, and microfacies.

Lithologic Characterization

Weight-percent calcium and aluminum plus silica were plotted against each other for the 85 total samples to establish lithology variation amongst the entire sample suite (Fig. 16). The ten high-graded samples from the Timbro well in the DJ Basin are composed of two chalks, five marly chalks, and three marls. The eleven samples from the two Piceance wells consist of five marls and six marly shales (Table 1).

The microprobe elemental maps constructed using composite images of Ca, Si, and Al (Fig. 17) show that peloids consist of almost completely of calcite (coccolith fragments with calcite overgrowth cement). In contrast, matrices comprise a wider range of minerals from almost complete calcite in chalk samples to almost complete quartz and clay minerals in shaley samples.

Petrographic Characterization

Based on visually estimated proportions of sand-sized (foraminifera shells and peloids), silt-sized (siliciclastic silt) and clay-sized material, all 85 samples were divided into five distinct

Table 1. Complete list of 85 samples, their lithology proxies, lithologies, petrographic components, and microfacies. PW = Peloidal Wackestone PP = Peloidal Packstone SW = Silty Wackestone SP = Silty Packstone *Information not available

Basin	Well	Depth	Weight % Ca	Weight % Al+Si	Lithology	Clay %	Sand %	Silt %	Microfacies
DJ	Timbro	5666	77.3	21.2	MC	50	40	10	PW
DJ	Timbro	5675.6	57.1	26.6	M	20	70	10	PP
DJ	Timbro	5680.7	61.8	29.2	MC	40	55	5	PP
DJ	Timbro	5689.3	83.0	13.1	MC	40	55	5	PP
DJ	Timbro	5698	82.4	11.6	MC	25	70	5	PP
DJ	Timbro	5703.3	85.9	11.2	C	25	70	5	PP
DJ	Timbro	5714	82.2	14.4	MC	30	65	5	PP
DJ	Timbro	5718.3	75.9	16.8	MC	40	55	5	PP
DJ	Timbro	5721.7	89.4	7.6	C	65	30	5	PW
DJ	Timbro	5724.2	92.2	5.8	C	75	20	5	PW
DJ	Timbro	5730.5	86.6	9.7	C	75	20	5	PW
DJ	Timbro	5731.9	66.4	24.9	MC	65	25	10	PW
DJ	Timbro	5739.6	19.1	66.8	MS	50	45	5	PW
DJ	Timbro	5742	89.6	8.1	C	65	30	5	PW
DJ	Timbro	5745.2	58.3	31.6	M	65	30	5	PW
DJ	Timbro	5747.5	93.7	5.1	C	70	25	5	PW
DJ	Timbro	5752.7	84.2	14.8	MC	45	50	5	PW
DJ	Timbro	5758	52.5	30.9	M	15	75	10	PP
DJ	Timbro	5768	47.3	37.6	M	25	65	10	PP
DJ	Timbro	5772.5	50.1	46.6	M	20	75	5	PP
DJ	Timbro	5783.2	42.7	54.4	M	25	65	10	PP
DJ	Timbro	5790	63.1	39.5	MC	70	20	10	PW
DJ	Timbro	5799.5	78.6	19.5	MC	35	50	15	PP
DJ	Timbro	5801.9	77.4	21.3	MC	80	10	10	CS
DJ	Timbro	5809.5	64.6	29.1	MC	80	10	10	CS
DJ	Timbro	5811	73.7	25.7	MC	75	15	10	PW
DJ	Timbro	5813.6	55.5	35.2	M	70	20	10	PW
DJ	Timbro	5815.3	78.0	20.6	MC	60	30	10	PW
DJ	Timbro	5816.8	52.7	44.8	M	50	25	25	PW
DJ	Timbro	5823.4	69.2	29.2	MC	65	20	15	PW
DJ	Timbro	5825.7	41.3	52.3	M	70	20	10	PW
DJ	Timbro	5828.6	59.7	38.1	M	85	5	10	CS
DJ	Timbro	5833.8	43.4	53.8	M	65	5	30	SW
DJ	Timbro	5835.7	53.9	43.5	M	65	5	30	SW
DJ	Timbro	5838	57.7	39.0	M	60	5	35	SW
DJ	Timbro	5843	46.8	28.9	M	70	15	15	PW
DJ	Timbro	5849	46.9	38.5	M	40	55	5	PP
DJ	Timbro	5861	46.9	38.0	M	20	70	10	PP
DJ	Timbro	5871	49.1	44.9	M	50	35	15	PW
DJ	Timbro	5886	34.1	58.8	M	30	60	10	PP
DJ	Timbro	5892	70.7	27.5	MC	70	15	15	PW
DJ	Timbro	5902	82.3	13.8	MC	70	25	5	PW

Table 1. (Continued) Complete list of 85 samples, their lithology proxies, lithologies, petrographic components, and microfacies. PW = Peloidal Wackestone PP = Peloidal Packstone SW = Silty Wackestone SP = Silty Packstone *Information not available

Piceance	#5	7550	33.0	49.1	M	60	30	10	PW
Piceance	#5	7600	25.8	60.9	MS	50	25	25	PW
Piceance	#5	7635	39.1	49.3	M	30	50	20	PP
Piceance	#5	7638	45.3	44.1	M	40	25	35	SP
Piceance	#5	7640	40.5	48.2	M	40	30	30	PP
Piceance	#5	7642	36.1	51.1	M	50	25	25	PW
Piceance	#5	7643	39.9	48.5	M	45	25	30	SW
Piceance	#5	7645	36.7	50.9	M	50	20	30	SW
Piceance	#5	7647	29.7	57.4	MS	40	40	20	PP
Piceance	#5	7648	37.5	50.5	M	*	*	*	*
Piceance	#5	7650	22.7	62.1	MS	*	*	*	*
Piceance	#5	7652	39.6	48.6	M	45	20	35	SW
Piceance	#5	7700	22.3	63.8	MS	*	*	*	*
Piceance	#5	7750	17.5	67.5	MS	30	10	60	SP
Piceance	#5	7800	25.3	62.0	MS	45	15	40	SW
Piceance	#5	7850	22.3	63.7	MS	45	10	45	SW
Piceance	#5	7900	22.1	65.2	MS	50	10	40	SW
Piceance	#5	7950	27.7	60.8	MS	50	20	30	SW
Piceance	#5	8000	36.6	51.6	M	20	35	40	SP
Piceance	#5	8300	16.3	71.1	MS	70	0	30	SW
Piceance	#5	8350	23.7	62.2	MS	65	10	25	SW
Piceance	#5	8376	16.9	70.5	MS	70	0	30	SW
Piceance	#5	8380	33.5	55.1	M	75	10	15	SW
Piceance	#5	8382	28.9	57.7	MS	40	30	30	PP
Piceance	#5	8383	28.4	59.0	MS	45	20	35	SW
Piceance	#5	8385	14.5	68.7	MS	70	5	25	SW
Piceance	#5	8390	16.1	69.1	MS	55	5	40	SW
Piceance	#4	10010.66	19.8	65.6	MS	50	10	40	SW
Piceance	#4	10025.16	16.2	67.9	MS	50	10	40	SW
Piceance	#4	10045.13	41.7	47.2	M	30	35	35	PP
Piceance	#4	10064.77	24.4	62.2	MS	50	25	25	PW
Piceance	#4	10071.9	18.7	66.6	MS	35	15	50	SP
Piceance	#4	10126.17	17.3	68.2	MS	30	10	60	SP
Piceance	#4	10142.78	14.0	71.5	MS	35	10	55	SP
Piceance	#4	10207.38	36.9	51.6	M	35	25	40	SP
Piceance	#4	10242.21	16.0	69.5	MS	30	5	65	SP
Piceance	#4	10251.92	35.7	52.7	M	35	40	25	PP
Piceance	#4	10289.8	23.5	63.4	MS	40	10	50	SP
Piceance	#4	10355.13	37.8	51.9	M	40	30	30	PP
Piceance	#4	10379	41.7	47.3	M	*	*	*	*
Piceance	#4	10380.26	29.3	59.0	MS	50	25	25	PW
Piceance	#4	10386.23	42.3	46.6	M	40	30	30	PP
Piceance	#4	10395.23	56.6	33.6	M	35	35	30	PP

Table 2. Complete list of 21 high-graded samples, their lithologies and microfacies. PW = Peloidal Wackestone PP = Peloidal Packstone SW = Silty Wackestone SP = Silty Packstone C = Chalk MC = Marly Chalk M = Marl MS = Marly Shale

Basin	Well	Depth	Lithology	Microfacies
DJ	Timbro	5666	MC	PW
DJ	Timbro	5680.7	MC	PP
DJ	Timbro	5703.3	C	PP
DJ	Timbro	5724.2	C	PW
DJ	Timbro	5758	M	PP
DJ	Timbro	5799.5	MC	PP
DJ	Timbro	5813.6	M	PW
DJ	Timbro	5823.4	MC	PW
DJ	Timbro	5835.7	M	SW
DJ	Timbro	5902	MC	PW
Piceance	#5	7638	M	SP
Piceance	#5	7750	MS	SP
Piceance	#5	7645	M	SW
Piceance	#5	8000	M	SP
Piceance	#5	8382	MS	PP
Piceance	#5	8390	MS	SW
Piceance	#4	10010.66	MS	SW
Piceance	#4	10045.13	M	PP
Piceance	#4	10142.78	MS	SP
Piceance	#4	10251.92	M	PP
Piceance	#4	10380.3	MS	PW

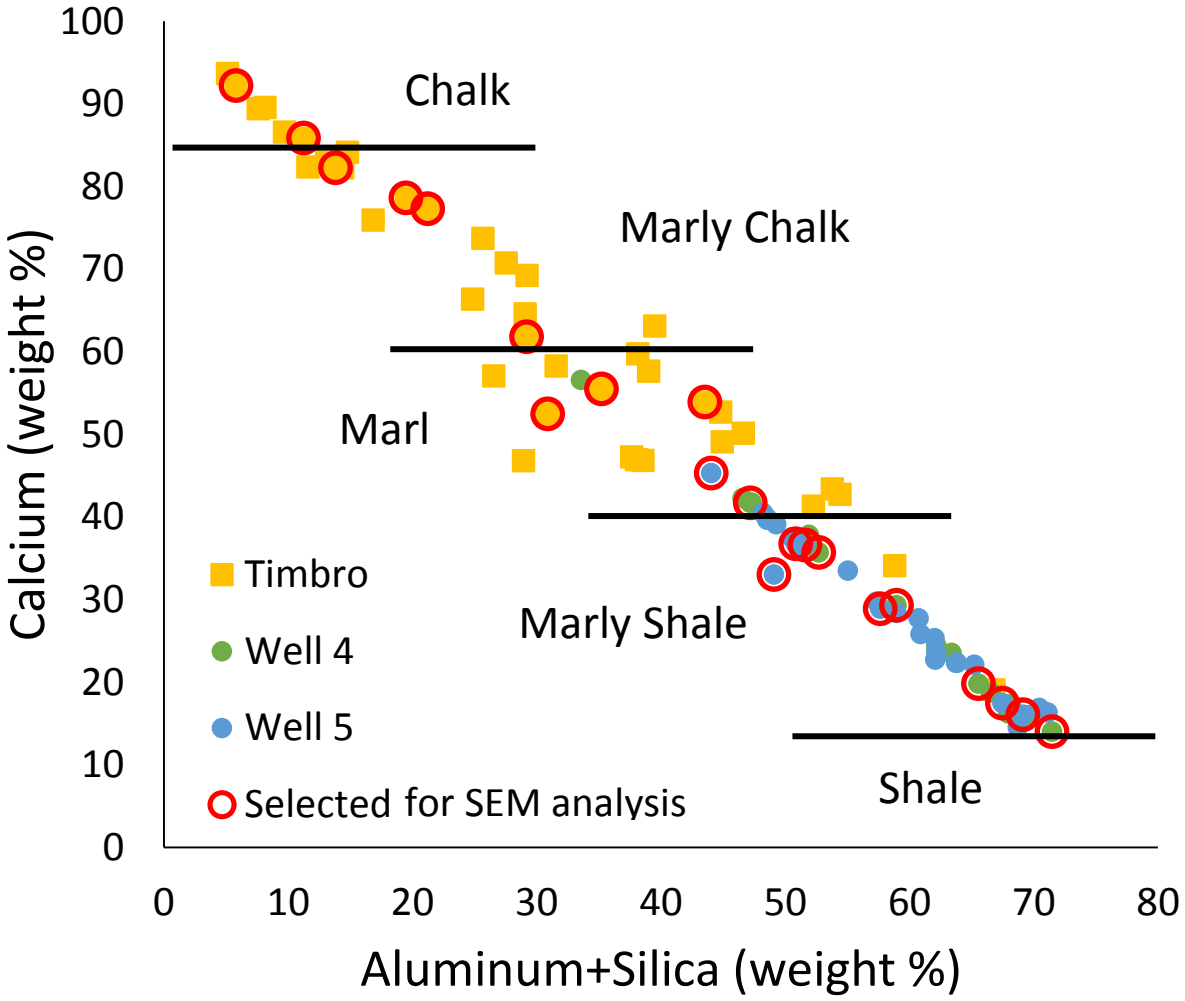

Figure 16. Weight percentages of calcium versus silicon plus aluminum for all samples. Squares represent DJ basin samples and circles represent Piceance Basin samples. Samples circled in red are the 21 used for SEM analysis. Lithofacies divisions are shown along with rock names.

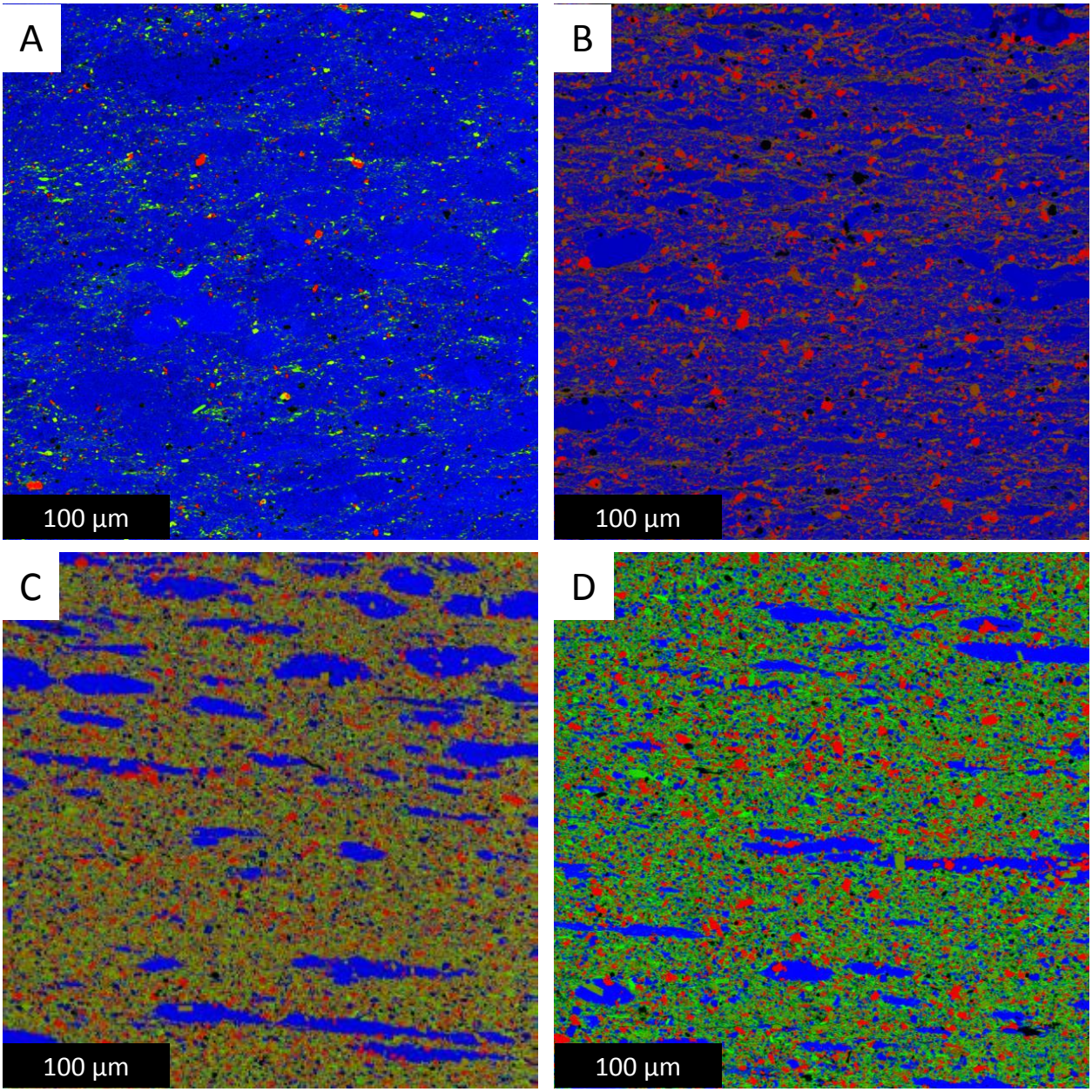

Figure 17. Microprobe elemental maps illustrating mineralogical differences between the four lithofacies studied. Blue indicates calcite, red is silica, black is pyrite or organic material, and orange through green are aluminosilicates. A) Chalk, Timbro, 5724 B) Marly chalk, Timbro, 5823 C) Marl, well #5, 7645 D) Marly shale, well #5, 7750.

microfacies (Fig. 18; Table 1). Microfacies are defined as claystone (greater than 80% clay), peloidal wackestone (between 20 and 50% clay and containing a greater proportion of sand-sized material than silt-sized material), peloidal packstone (less than 50% clay and containing a greater proportion of sand-sized material than silt-sized material), silty wackestone (between 20 and 50% clay and containing a greater proportion of silt-sized material than sand-sized material), and silty packstone (less than 50% clay and containing a greater proportion of silt-sized material than sand-sized material). Examples of each microfacies is shown in thin section in Figure 19. Silty microfacies dominate Piceance Basin samples, while the DJ samples are relatively peloid rich. Of the ten final high-graded DJ samples there are no silty wackestones and only one silty packstones. Of the eleven high-graded Piceance samples there are only three peloidal packstones and one peloidal wackestone (Table 2).

Although microfacies are determined based on differing criteria in Michaels (2014) and Burt (2014), some comparisons can be made. Because those two authors each looked at only one of the two basins each, a scheme to capture the full fabric variation between basins was unnecessary. Burt (2014) did recognize much more silt in the Piceance Basin samples than Michaels (2014) did in the DJ Basin samples. This observational consistency is the only trait commonly shared by their microfacies schemes and the one herein, suggesting that large interpreter bias is present in the visual estimates of the depositional elements.

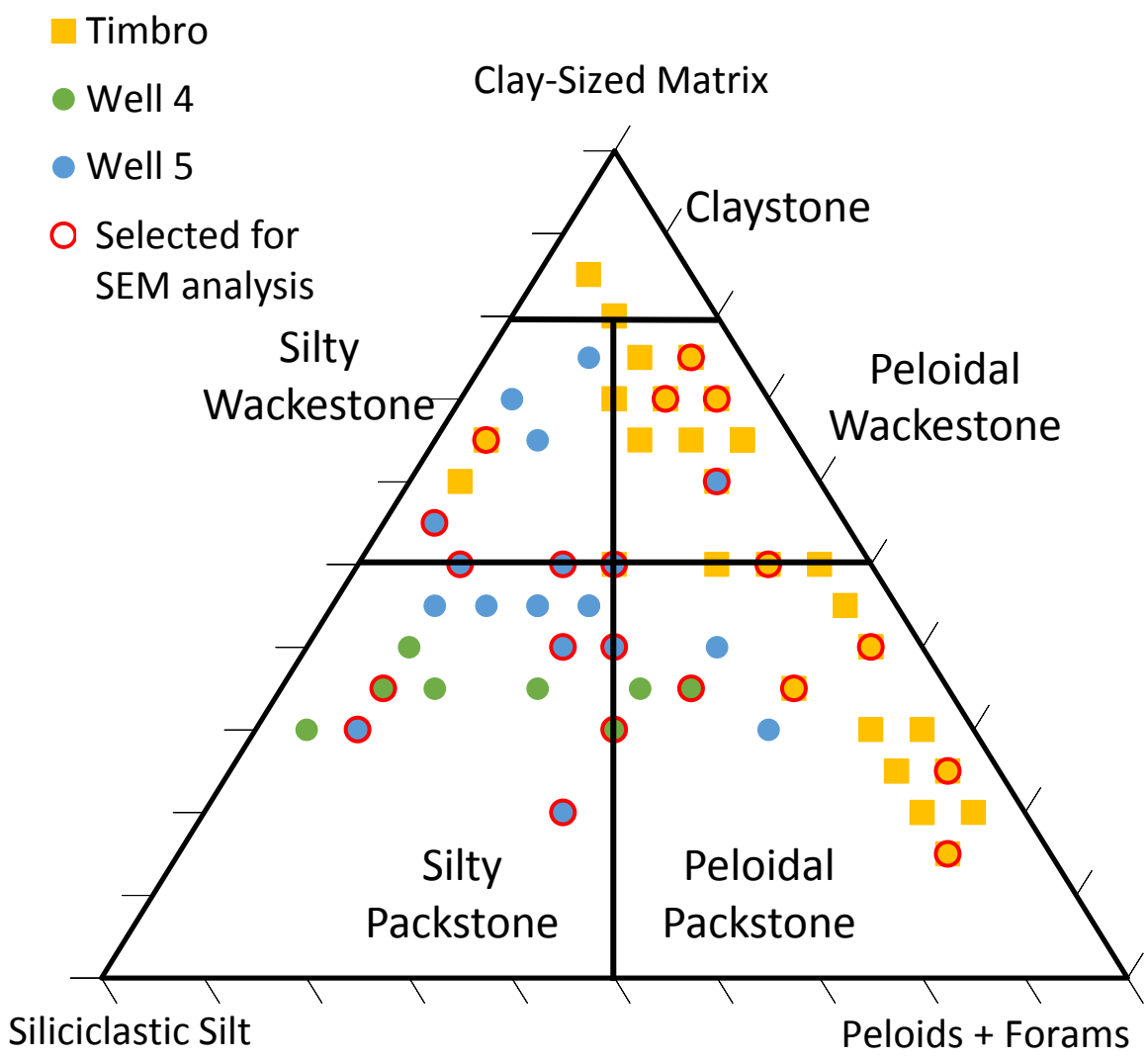

Figure 18. Ternary diagram depicting modal proportions of clay-sized matrix material, siliciclastic silt, and sand-sized material (peloids and foram tests). Samples are shown as either squares (DJ Basin) or circles (Piceance Basin). The boundaries of the five microfacies are defined by the black lines. Red circled samples are the 21 used for SEM analysis.

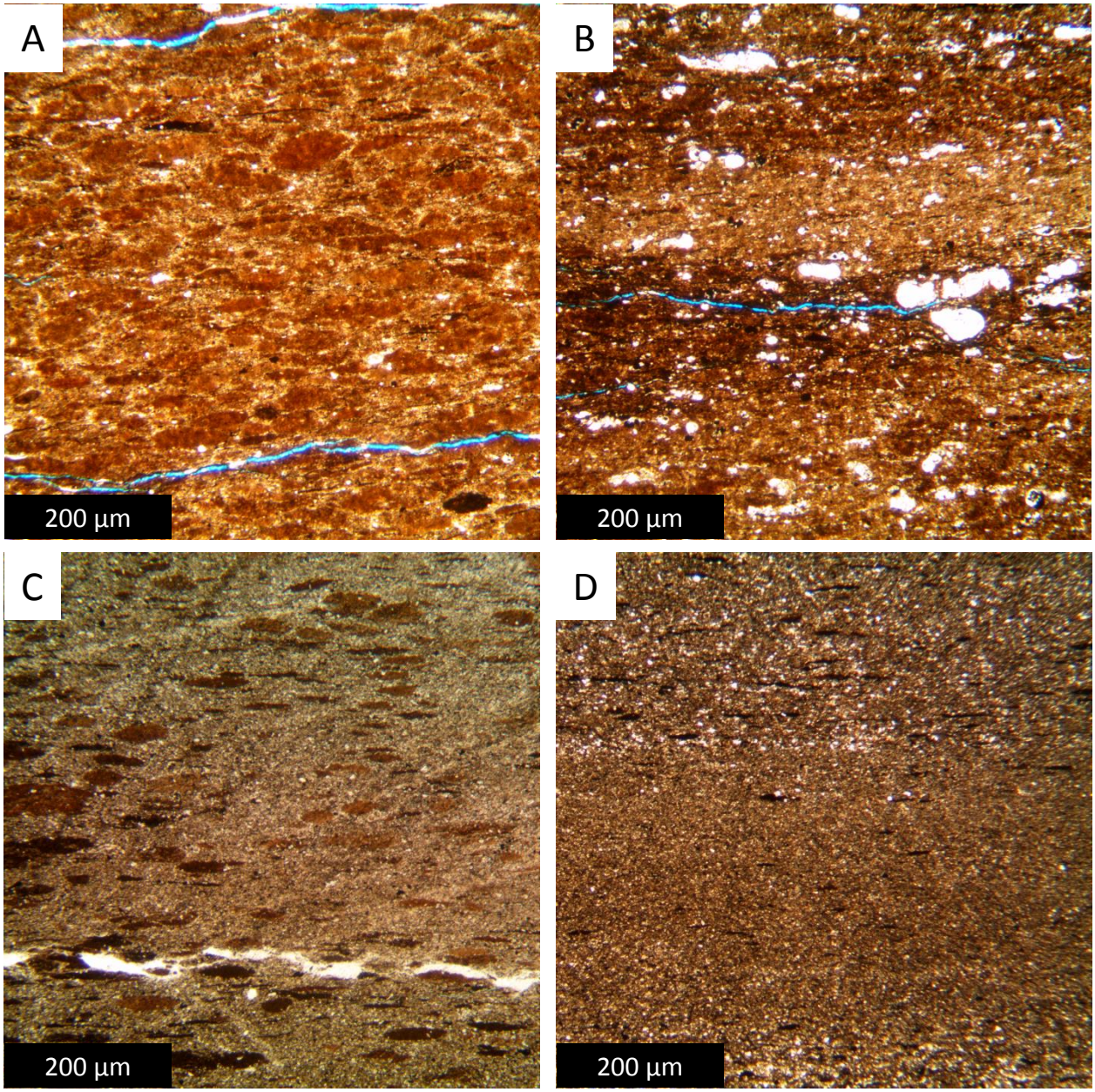

Figure 19. Thin-section photomicrographs exemplifying the four lithofacies studied. A) Chalk, Timbro, 5724 B) Marly chalk, Timbro, 5823 C) Marl, #5, 7645 D) Marly shale, #5, 7750.

CHAPTER 5: RESULTS

Burt (2014) and Michaels (2014) showed that the Niobrara Interval in both the Piceance and DJ basins, respectively, contained a variety of intercrystalline and intraparticle pore space that was partially to completely filled with residual migrated hydrocarbons (RMHC). How much, if any of that RMHC would be mobile at reservoir conditions was unknown by Michaels (2014) and Burt (2014), but presumably would depend on thermal setting. In the Timbro well utilized herein, a %Ro value of ~0.85 (Michaels, 2014) indicates it would still contain liquid hydrocarbons, In contrast, the two Piceance wells studied herein have %Ro values of 1.8 and 2.5 (Burt, 2014) indicating they would not contain mobile, liquid hydrocarbons. Evaluating lithologic controls on the pore systems would thus be hindered by the uncertainty in the mobility of the RMHC.

To overcome this problem, and to explore just lithologic controls, the focus was placed on the pre-migration pore system. Eliminating the overprint of the RMHC allows any lithologic controls on pore systems to be resolved. Most reported results are thus for the pre-migration pore systems and ignore the RMHC that occupy some or all pores in the analyzed 2D fields of view. That also means the results do not incorporate pores that may occur within the RMHC. The current pore system, which accounts for the RMHC in pores, is reported for a subset of the 21 samples and the potential impact of the presence of the RMHC is taken up in the discussion of the results (Chapter 6).

The 21 high-graded samples display a broad variation in total pre-migration porosity and a significant variety of pore types, pore sizes, pore shapes, and pore orientations. Each of these

observations can be tied, with varying correlation strength to fabric elements, lithology, and microfacies.

Pore Network Variability by Fabric elements

Regardless of lithology or microfacies, all but one of the samples contain two, identifiable basic fabric elements: peloids and matrix (Fig. 12). Matrix material spans a spectrum from nearly total calcite (chalks) to nearly total siliciclastic minerals (marly shales) while peloids are consistently just calcite. As a result, pore characteristics between the two fabric elements differ. Because those elements vary in abundance by lithology and microfacies, pore types appear in differing amounts based on microfacies, lithology, and the surrounding fabric element.

In masses of calcite, be it in peloids and wherever calcite occurs in the matrix (especially in chalks and marly chalks), there is a dominant intercrystalline pore system formed in association with the calcite rhombs (Fig. 20). These pores are defined by the rhombic shapes of the calcite crystals and often have rhombic terminations of calcite crystals extending into the pores. Also potentially present are intraparticle pores within coccolithophore spines that range from spheres to elongate ovals in 2D milled images depending on the orientation of the spine relative to the milled face (Fig. 21). In 3D, these pores form tubes. Lastly, intraparticle pores maybe present in sand-sized foram shells that occur within matrix (Fig. 22), although such pores are rare and typically small as cements generally occlude almost all of the original open space in the forams.

Where siliciclastic material dominates, which is in the matrix of marls and shaley marls, interparticle pores between siliciclastic silt and clay minerals (Fig. 23) are common. As the

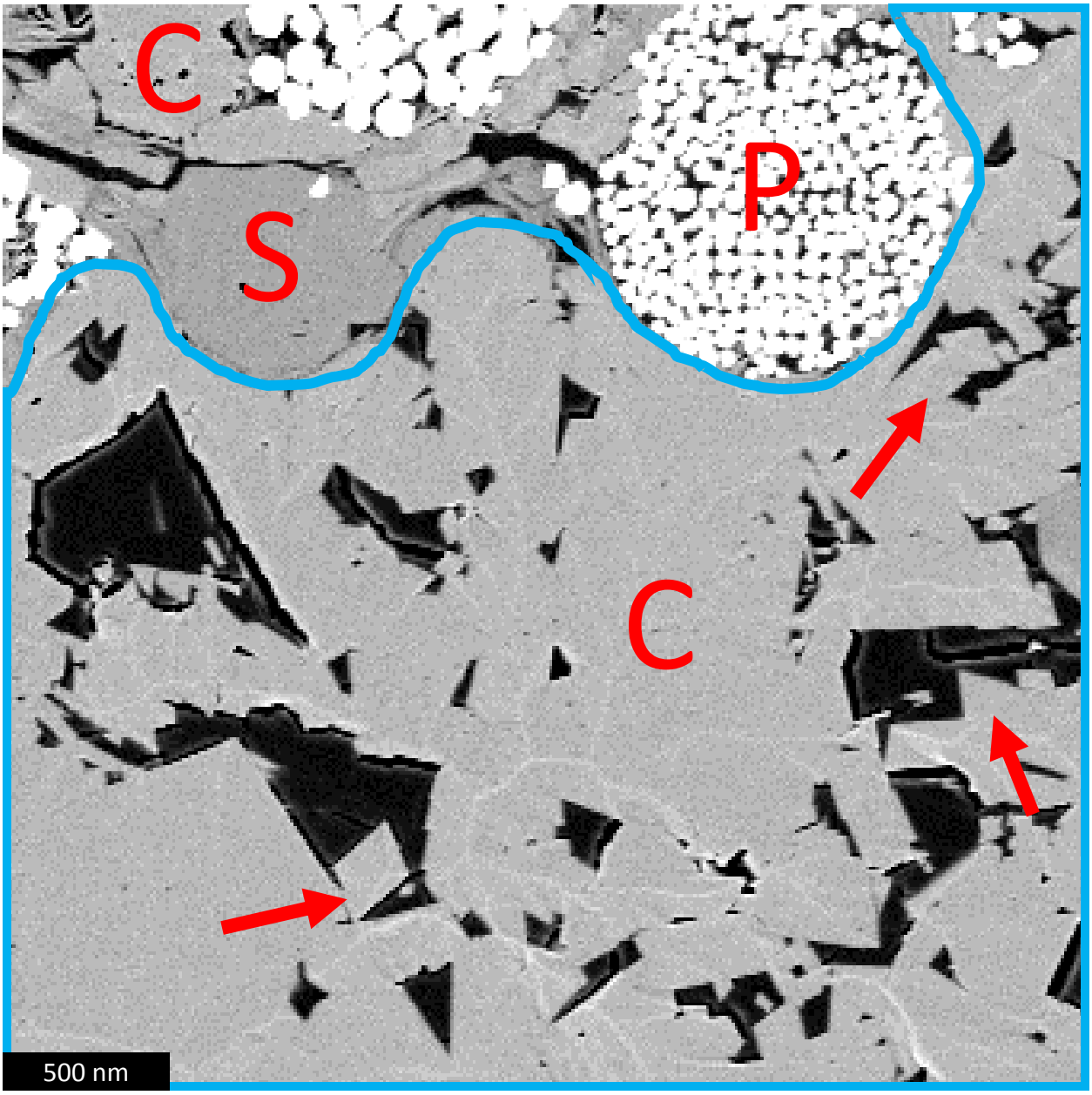

Figure 20. Backscattered SEM image of a peloid (outlined in blue) in a marly chalk sample (Timbro, 5666). Red arrows point to several of the many calcite rhombs that grew into open intercrystalline pores that were subsequently partially filled with migrated hydrocarbon. Also annotated are pyrite (P), a siliciclastic mineral (S), and calcite (C).

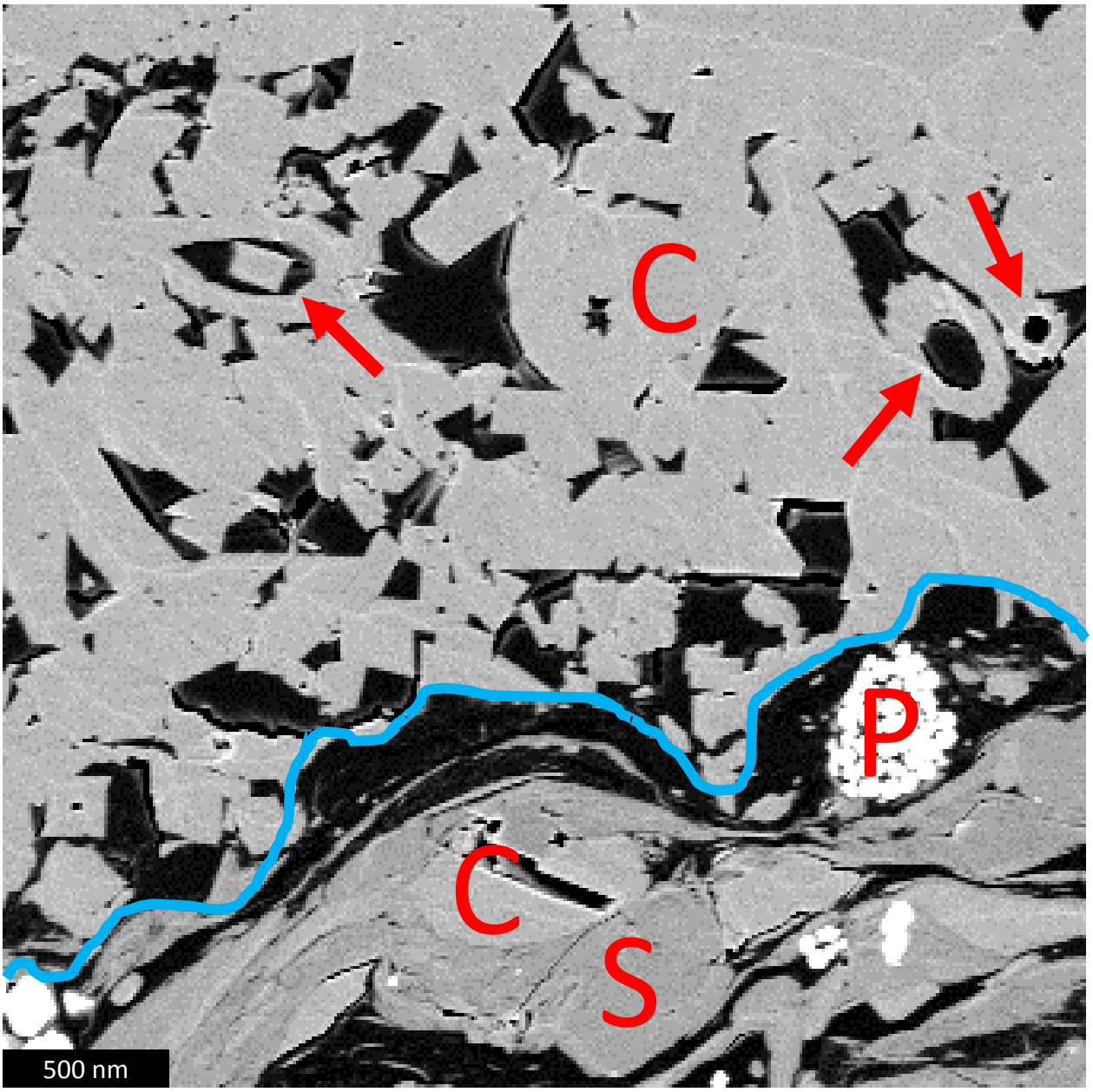

Figure 21. Backscattered SEM image of a peloid (above blue line) in Timbro, 5666. Red arrows point to intraparticle pores within cocclithophore spines. The intraparticle pore in the spine in the top left shows partial filling by a calcite crystal. Also annotated are the three different mineralogies shown: pyrite (P), a siliciclastic mineral (S), and calcite (C).

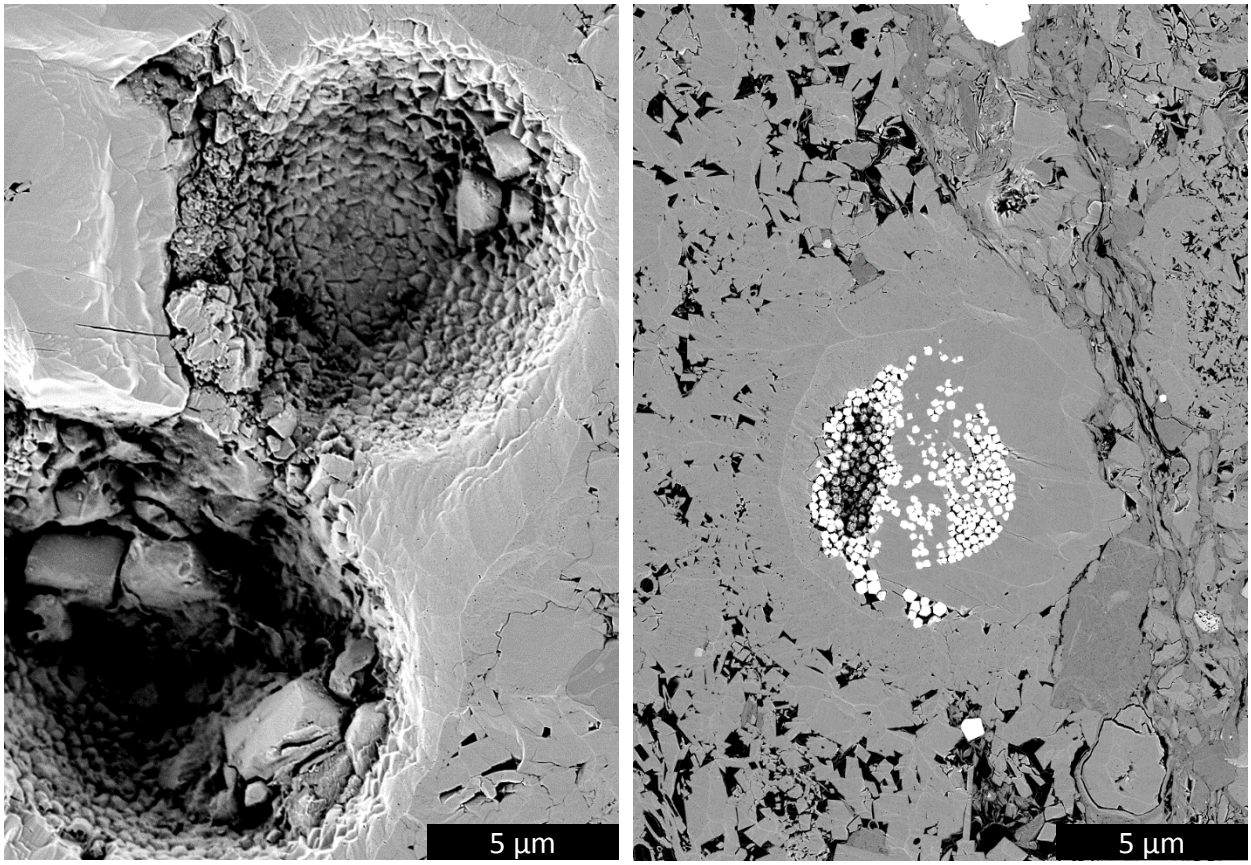

Figure 22. Backscattered SEM images of intraparticle porosity inside foram tests in Timbro, 5902 (left) and Timbro, 5835 (right). The left image shows a nearly completely intraparticle pores in a foram with only minor calcite cement lining the inside of the shell. The right image shows a foram partially filled with calcite and pyrite. A small amount of intraparticle porosity remains between crystals of calcite cement.

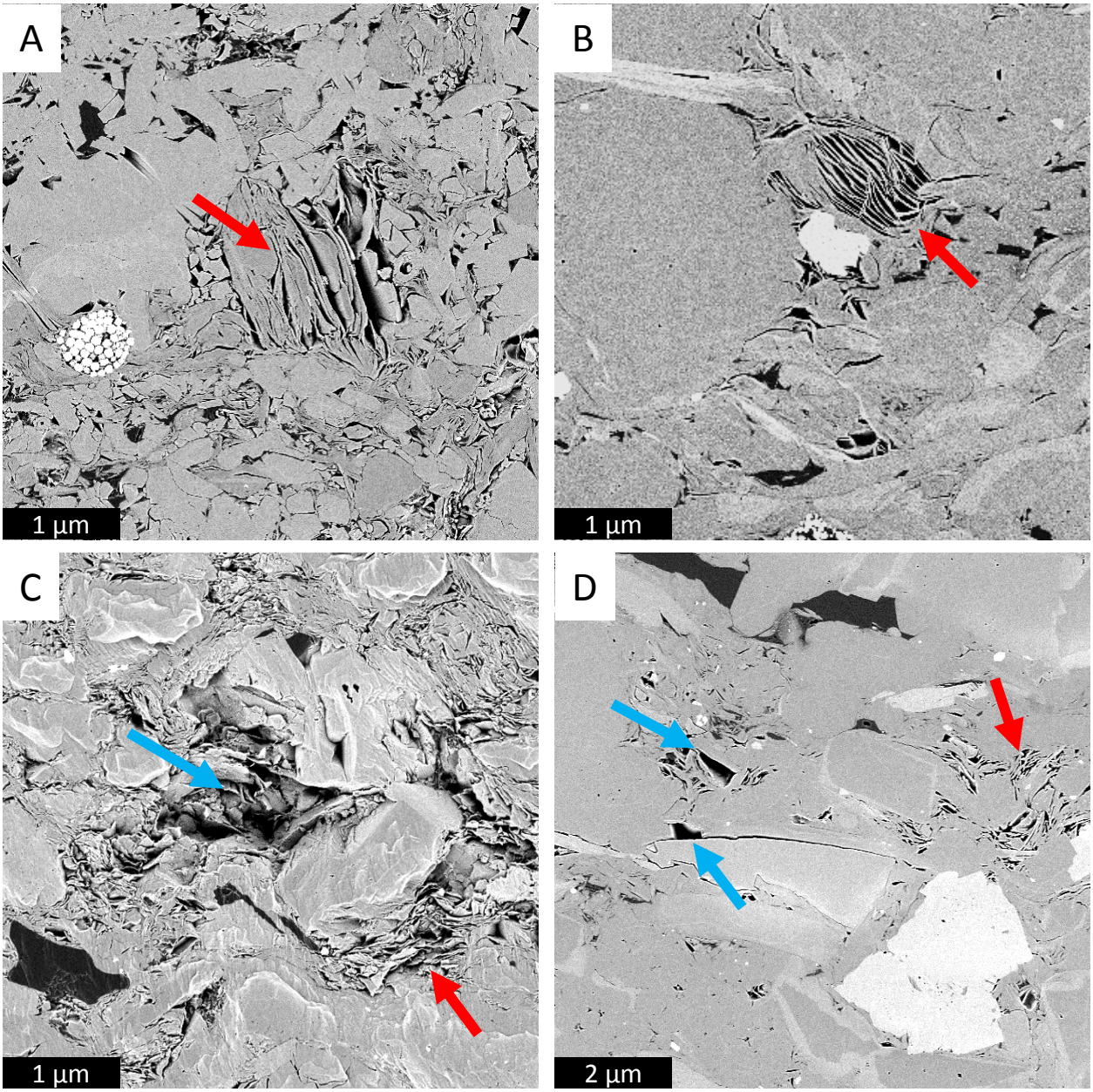

Figure 23. Backscattered SEM images of interparticle porosity between clay minerals and silt grains. Red arrow indicate clay-related porosity and blue arrows indicate silt-related porosity. A) Timbro, 5813, marl B) well #4, 10142, marly shale C) well #5, 7750, marly shale D) well #4, 10045, marl.

abundance of siliciclastic material increases in the matrices, the clay-related pores become visibly more elongate, and preferentially more horizontal.

Median pre-migration pore characteristics for each sample, subdivided into peloid and matrix elements, are displayed in Table 3. Those values show that pre-migration pores in peloids (dominantly calcite) are bigger (Fig. 24), less anisotropic (Fig. 25), and less likely to have a strong horizontal component (Fig. 26) relative to pre-migration pores in matrices (mixed mineralogies). The average of median equivalent circular diameters (ECD) across all samples in matrix pores is 150.2 nm for group A and 230.5 nm for group B whereas in peloids average median ECD is 177.2 nm group A and 278.6 nm for group B[1]. Average median anisotropy is also greater in matrix pores (group A = 0.90; group B = 0.77) relative to average median peloid pore anisotropy (group A = 0.83; group B = 0.73). Pre-migration matrix pore horizontal preference has a range of 22.9% and average median values (group A average = 52.3%; group B average = 51.3%) that are greater than the range of and averages of peloid pores (range of 8.1%; group A average = 46.5%; group B average = 46.4%).

Pore Network Variability by Lithology

Total Pre-Migration Porosity

Total imaged 2-D pre-migration porosity varies significantly with lithology. It ranges from 3.41% to 11.77% and increases with total calcium content (the lithology proxy; Fig. 27) with a correlation coefficient of 0.85 (R^2= 0.72) when all imaged samples are considered. Samples from group A exhibit a correlation coefficient of 0.93 (R^2 = 0.87) and samples imaged in group B display the same trend with a slightly weaker correlation coefficient of 0.76 (R^2 = 0.58). Matrix

[1] As noted in the methods, the group B samples were not imaged as sharply as the group A samples. The poorer focus resulted in poorer resolution, thus pore metrics for group B have systematically larger values than group A.

Table 3. Complete list of 21 high-graded samples, their lithologies, microfacies, sampling group, median equivalent circular diameter (ECD), width, and anisotropies for each fabric element.. PW = Peloidal Wackestone PP = Peloidal Packstone SW = Silty Wackestone SP = Silty Packstone C = Chalk MC = Marly Chalk M = Marl MS = Marly Shale * No discernable peloids in this sample

						Total			Matrix			Peloid		
Basin	Well	Depth	Lithology	Microfacies	Group	ECD	Width	Anisotropy	ECD	Width	Anisotropy	ECD	Width	Anisotropy
DJ	Timbro	5666	MC	PW	A	149.7	120.6	0.88	149.7	120.0	0.89	174.8	160.0	0.83
DJ	Timbro	5680.7	MC	PP	B	246.1	204.0	0.76	234.8	203.0	0.77	304.9	257.0	0.75
DJ	Timbro	5703.3	C	PP	B	330.5	277.8	0.69	267.1	233.1	0.73	336.9	286.8	0.68
DJ	Timbro	5724.2	C	PW	B	265.1	229.3	0.74	265.1	230.0	0.74	256.8	216.4	0.72
DJ	Timbro	5758	M	PP	A	156.4	135.3	0.89	156.4	135.3	0.89	162.7	158.8	0.85
DJ	Timbro	5799.5	MC	PP	A	156.4	129.4	0.87	156.4	129.4	0.88	149.7	129.4	0.84
DJ	Timbro	5813.6	M	PW	A	180.5	160.0	0.84	156.4	137.9	0.89	196.7	185.3	0.82
DJ	Timbro	5823.4	MC	PW	B	246.1	204.0	0.76	243.9	204.0	0.76	261.0	222.6	0.75
DJ	Timbro	5835.7	M	SW	A	156.4	144.1	0.87	156.4	139.8	0.88	174.8	160.0	0.84
DJ	Timbro	5902	MC	PW	A	201.9	170.7	0.83	201.9	170.7	0.83	*	*	*
Piceance	#5	7638	M	SP	B	218.1	175.7	0.77	208.0	174.8	0.80	232.5	204.0	0.73
Piceance	#5	7750	MS	SP	A	142.7	120.0	0.91	142.7	120.0	0.91	149.7	135.3	0.83
Piceance	#5	7645	M	SW	B	246.1	197.5	0.79	227.8	192.8	0.81	250.4	204.0	0.73
Piceance	#5	8000	M	SP	A	149.7	138.3	0.88	149.7	128.4	0.90	174.8	160.0	0.80
Piceance	#5	8382	MS	PP	A	162.7	151.2	0.85	156.4	137.9	0.90	196.7	177.9	0.80
Piceance	#5	8390	MS	SW	B	210.5	174.8	0.79	200.0	170.9	0.80	303.1	257.0	0.74
Piceance	#4	10010.66	MS	SW	A	142.7	120.0	0.91	142.7	120.0	0.92	168.9	160.0	0.82
Piceance	#4	10045.13	M	PP	A	156.4	140.8	0.87	142.7	120.0	0.90	186.1	165.5	0.82
Piceance	#4	10142.78	MS	SP	A	149.7	120.0	0.90	142.7	120.0	0.91	186.1	160.0	0.83
Piceance	#4	10251.92	M	PP	A	162.7	150.2	0.85	149.7	120.0	0.89	180.5	160.0	0.82
Piceance	#4	10380.3	MS	PW	B	227.8	204.0	0.76	205.3	197.1	0.78	275.1	233.5	0.72

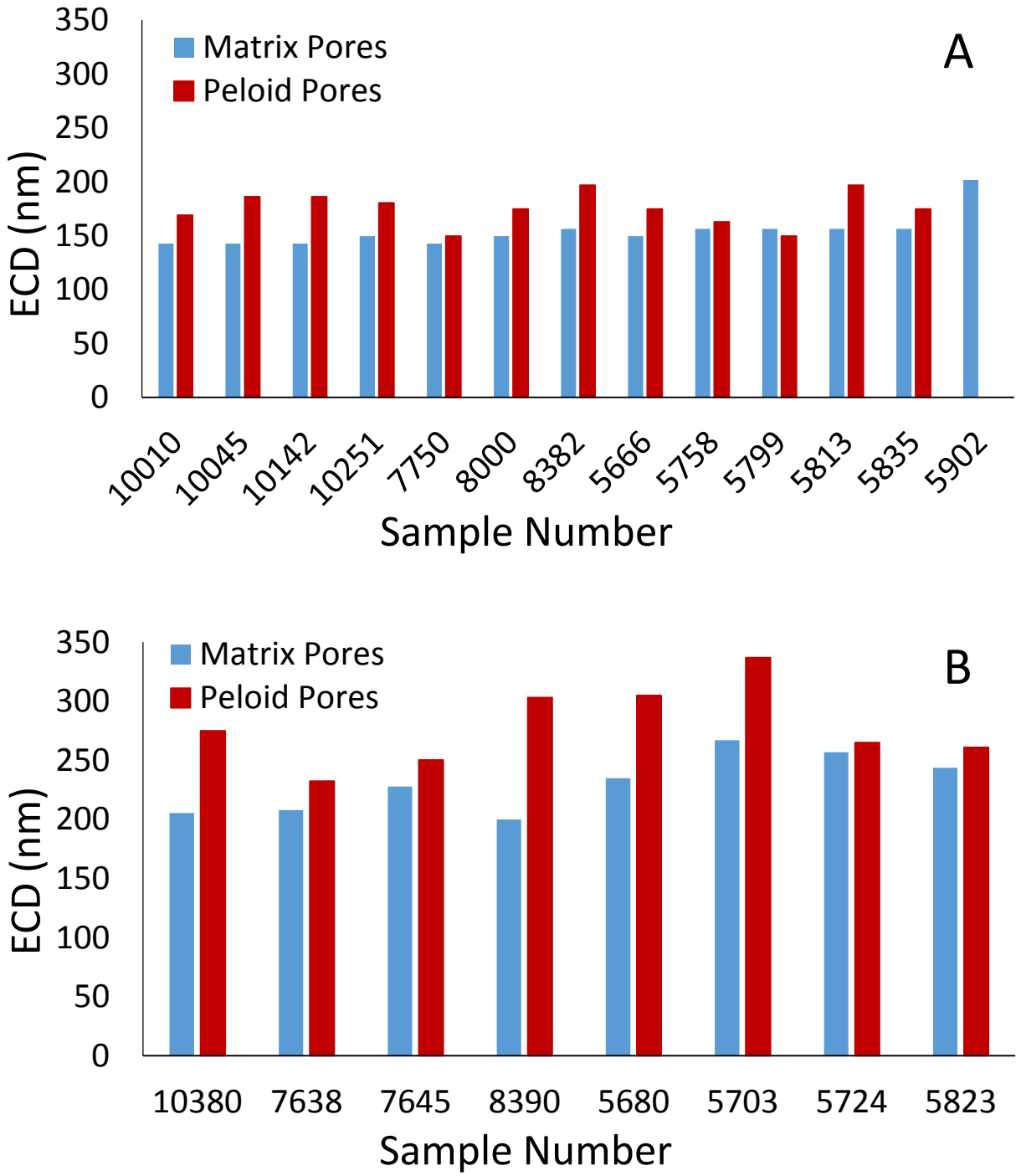

Figure 24. Median equivalent circular diameter (ECD) for pre-migration matrix and peloid pores. Group A samples (A) display lower average sizes than group B samples (B), but both groups show that peloid pores in every sample have higher median ECD than matrix pores. Peloids were indistinguishable from matrix in sample 5902 of group A, thus only a matrix value is shown for that sample.

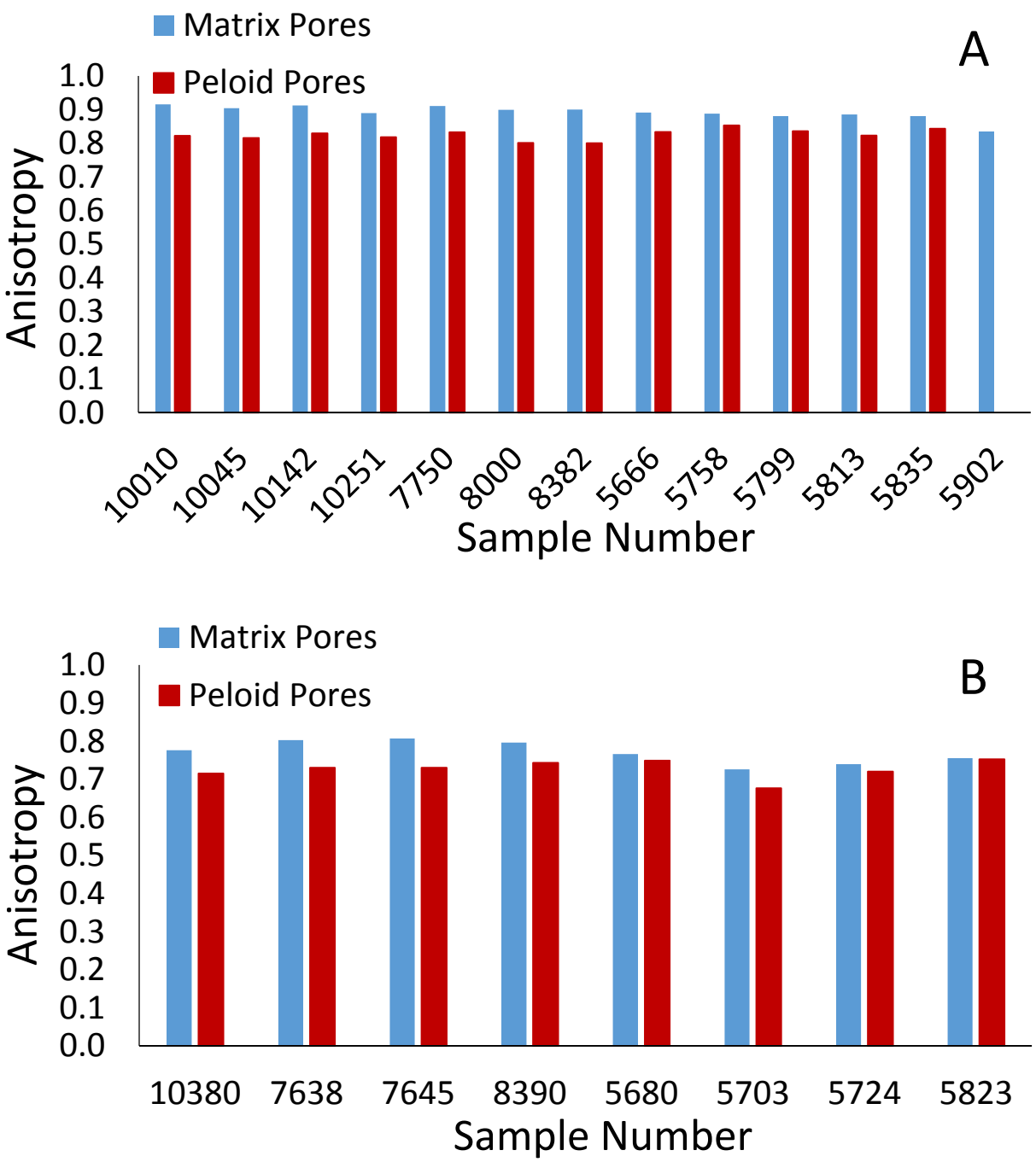

Figure 25. Median anisotropy values for for pre-migration matrix and peloid pores. Group A samples (A) display higher anisotropies than group B samples (B), but both groups show that peloid pores have lower anisotropy than matrix pores. Peloids were indistinguishable from matrix in sample 5902 of group A, thus only a matrix value is shown for that sample.

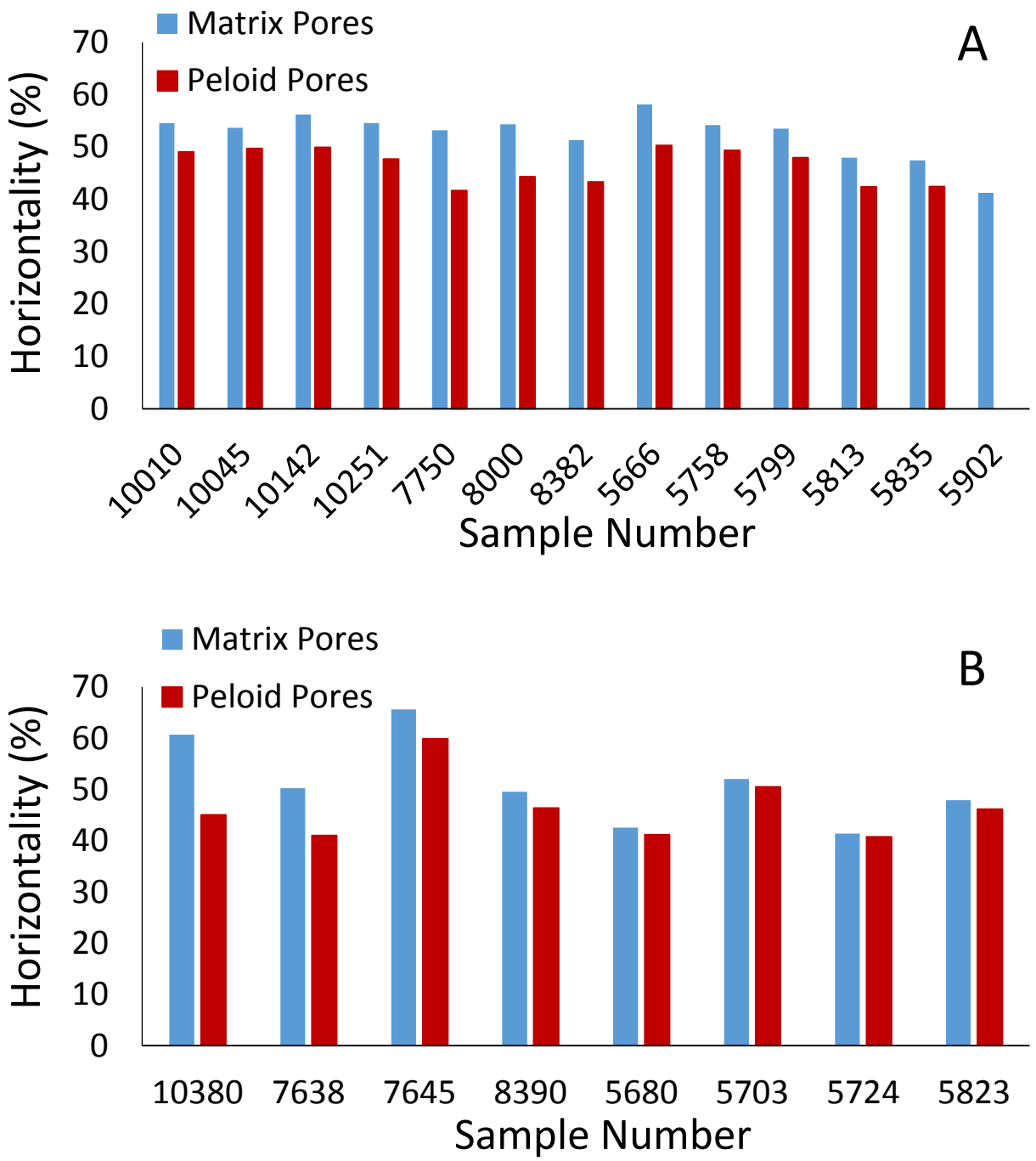

Figure 26. Median horizontality for pre-migration matrix and peloid pores. In both group A (A) and group B (B) samples, peloid pores are less likely to be oriented horizontality than matrix pores. Peloids were indistinguishable from matrix in sample 5902 of group A, thus only a matrix value is shown for that sample.

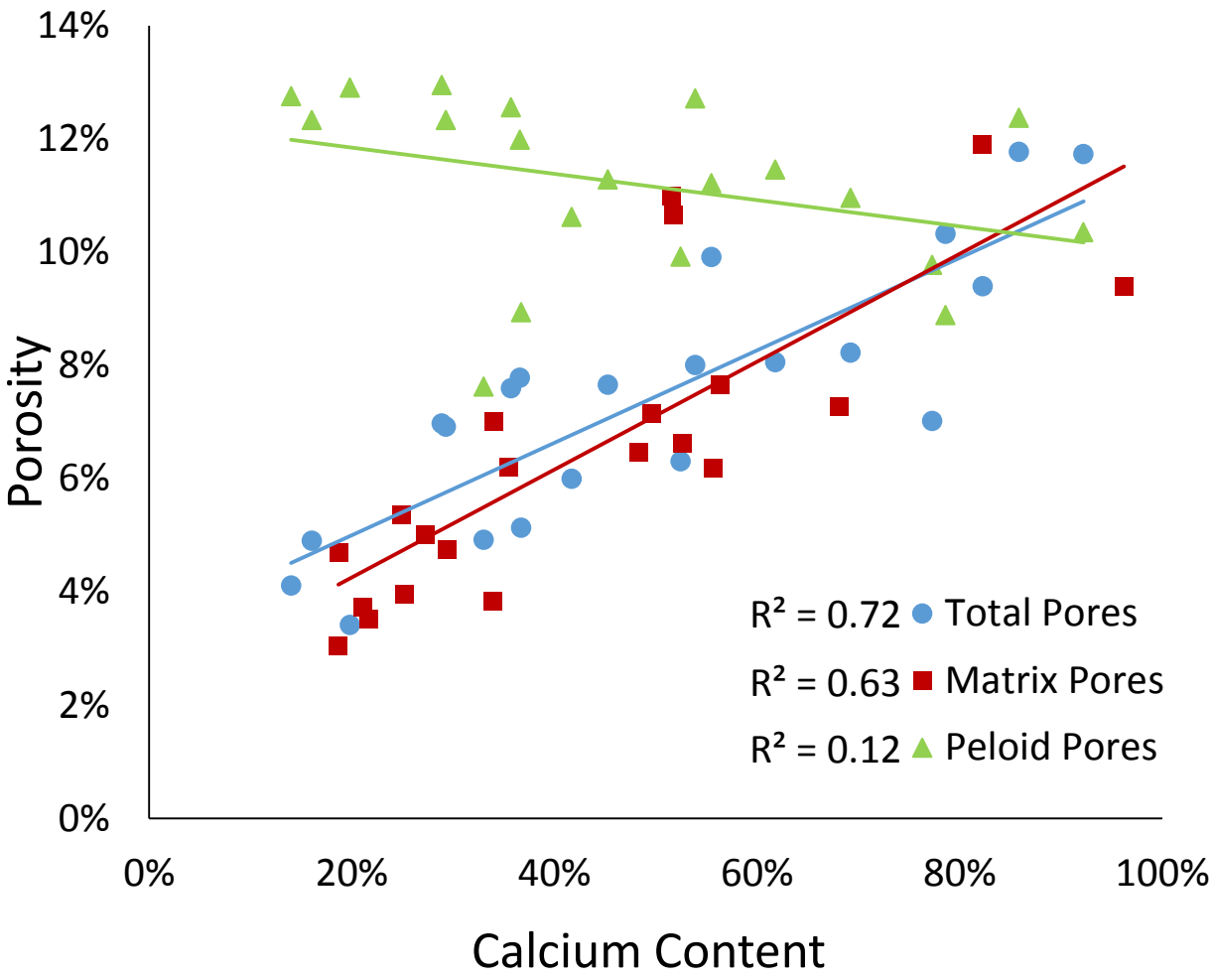

Figure 27. Total pre-migration porosity in all 21 samples from both basins and both sample groups. Blue circles represent total (matrix plus peloid) pores. Red squares are matrix pores and green triangles are peloid pores. Lines are best fit linear regressions with correlation coefficients shown in the key.

porosity also displays a strong correlation coefficient of 0.79 ($R^2 = 0.63$) and increases with matrix carbonate content. Peloids however, show a slight decrease in porosity with increasing total sample calcium but with correlation coefficient of only 0.35 ($R^2 = 0.12$).

Pre-Migration Pore Size

All pre-migration pore-size histograms for group A samples display a similar trend. In every sample, the 100-200 nm equivalent circular diameter is the most common size bin (44.6%-59.6%) for all pores (matrix and peloid together; Fig. 28A), peloid pores (Fig. 29A), and matrix pores (Fig. 30A), with the 200-300 nm size bin the second most populous (16.6%-23.7% of all pores). Variation based on lithology is minor, with larger variation within lithologies than between them. However, on average, when considering all pores in a sample, marly chalk samples show the smallest proportion in the smallest size ranges (44.6%-56.7%), marly shales show the largest proportion of pores in this range (53.9%-58.7%), and marls plot between the two end members (46.4%-58.2%) (Fig. 28).

Pore sizes in group B display the same trend in pore sizes as group A, but show a smaller proportion of all pores in the 100-200 nm bin (18.7%-33.5%; Fig. 28B) than do the group A samples and the same is true for peloid pores (Fig. 29B) and matrix pores (Fig. 30B). This smaller proportion of smaller pores is considered an artifact of relative image quality between the two groups, as discussed in Chapter 3. As in group A samples, the chalkiest group B samples plot with the smallest proportion of pores in the 100-200 nm range while the shaliest samples show the highest proportion of these small pores. In both groups, pore equivalent diameters in the 0-100 nm and 100-200 nm bins were more common in the matrix than in peloids.

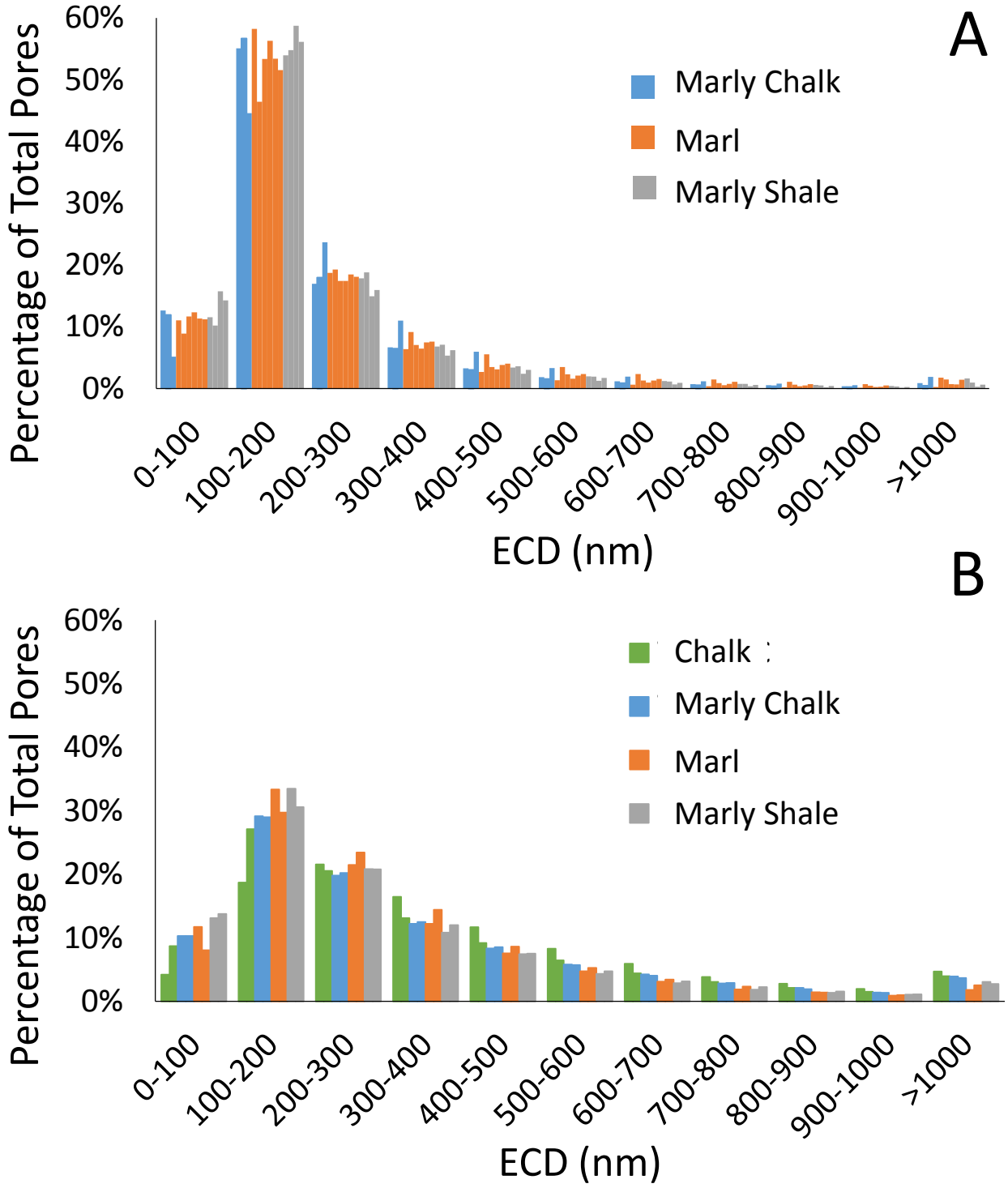

Figure 28. Histograms of percentage-normalized pre-migration pore-size (ECD) distributions for all pores in group A (A) and group B samples (B). Green bars are chalks, blue bars are marly chalks, orange bars are marls, and gray bars are marly shales.

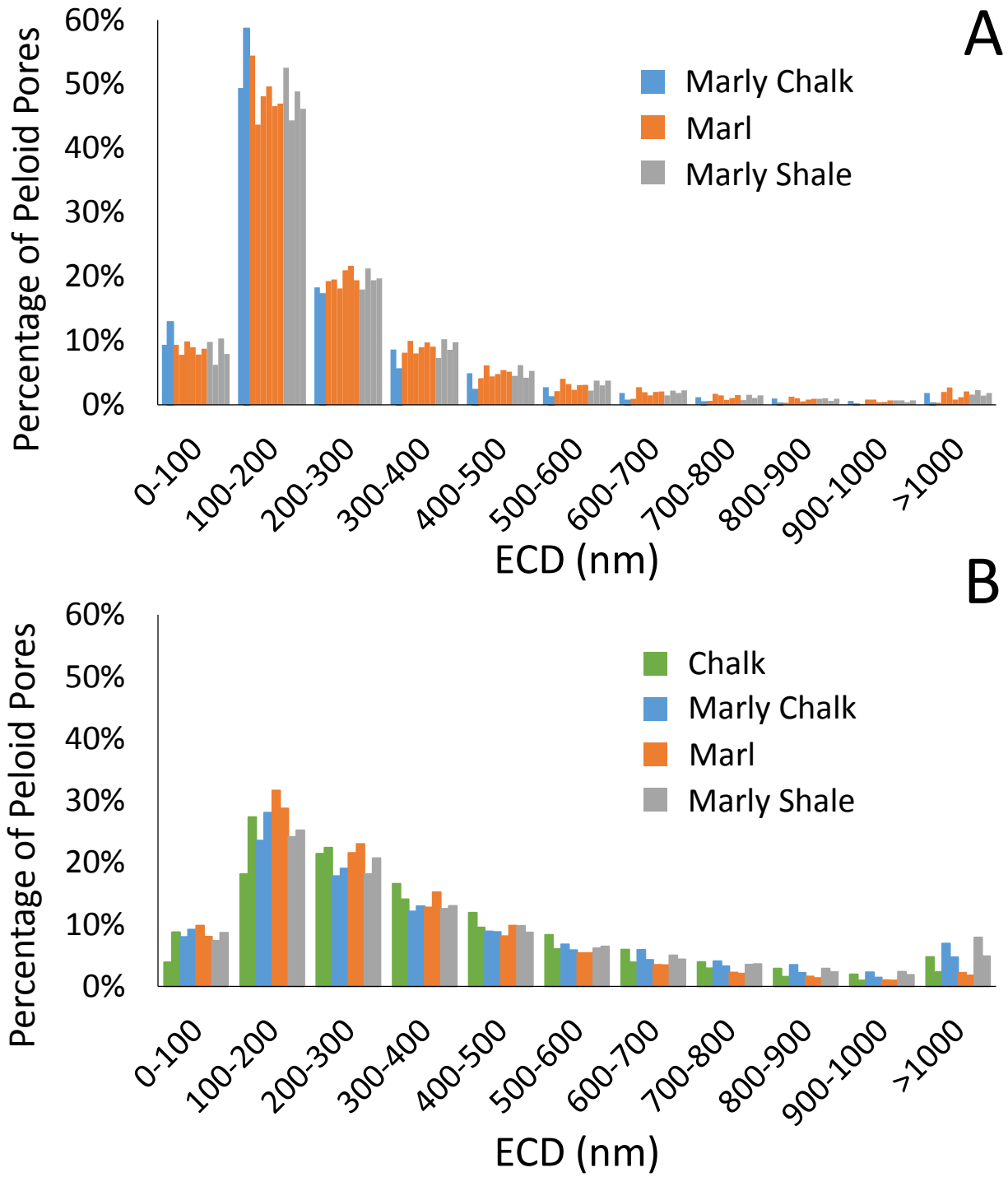

Figure 29. Histograms of percentage-normalized pre-migration pore-size (ECD) distribution for peloid pores in group A (A) and group B samples (B). Green bars are chalks, blue bars are marly chalks, orange bars are marls, and gray bars are marly shales.

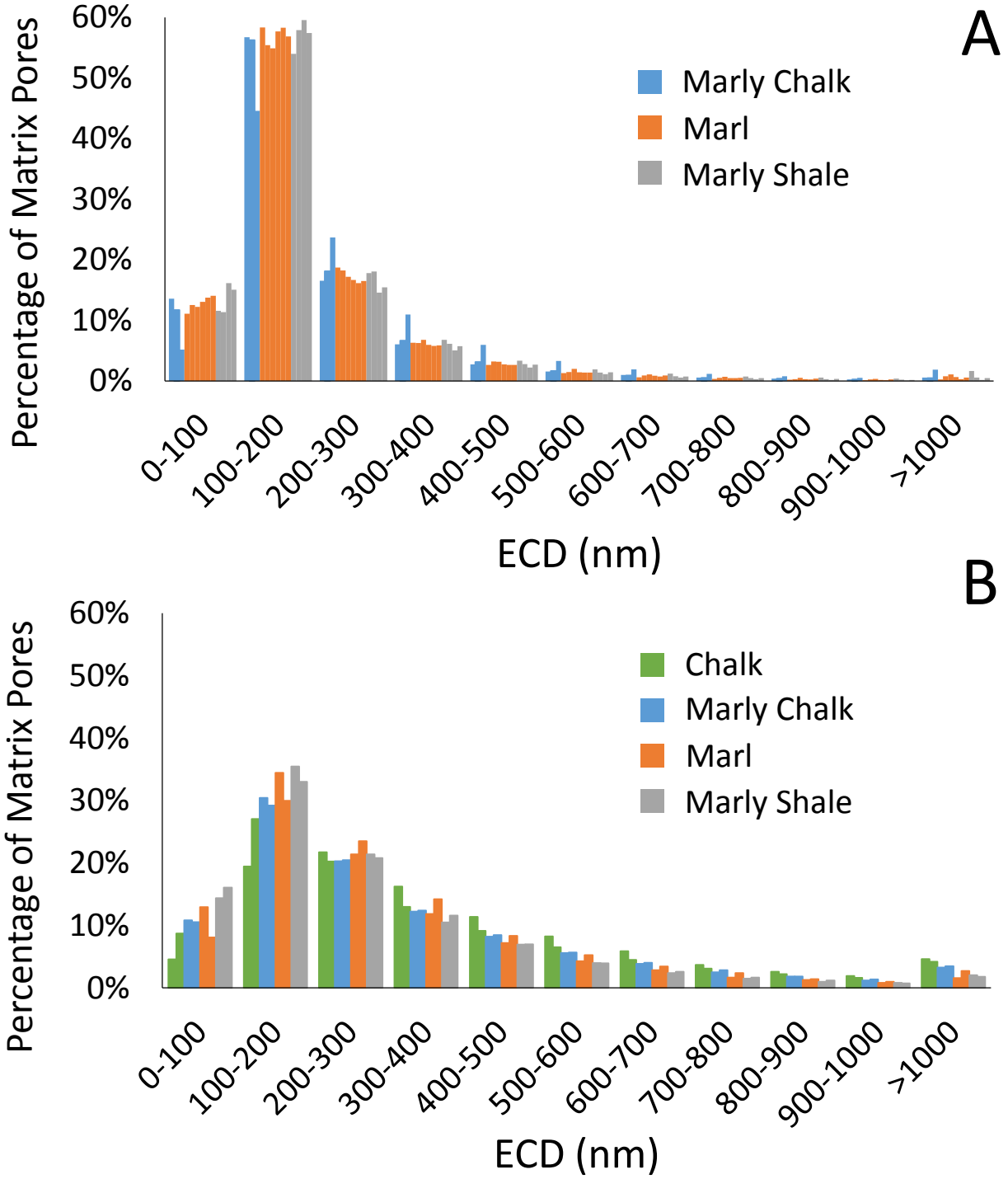

Figure 30. Histograms of percentage-normalized pre-migration pore-size (ECD) distribution for matrix pores in group A (A) and group B samples (B). Green bars are chalks, blue bars are marly chalks, orange bars are marls, and gray bars are marly shales.

Pre-migration median pore sizes (equivalent circular diameter) by fabric element (matrix, peloid) and for all pores in a sample are used for comparison with lithology (percent calcium) rather than mean pore size due to the skewness of the populations displayed in the pore-size histograms (Figs. 28-30). Pre-migration median pore size for all pores (matrix plus peloid) is plotted against total calcium from XRF measurements whereas pre-migration median matrix pore sizes are plotted against matrix calcium. The latter is calculated by subtracting area of peloid material (assumed to be 100% calcite) from total area of calcite observed in a sample's elemental map (Fig. 17). All pre-migration median pore sizes for all pores, matrix pores, and peloid pores in each sample are shown in Table 3.

Samples from groups A and B show little covariance between peloid pore sizes and lithology (Fig. 31; group A $R^2 = 0.02$, group B $R^2 = 0.09$), which is not surprising given that peloids consistently show an almost complete calcite mineralogy independent of total sample mineralogy (Fig. 17). Any covariance is considered to be noise derived from the varying matrix calcite signature. In contrast, there is a positive correlation between lithology and pre-migration median equivalent circular diameter of all pores and matrix pores (Fig. 32). For all pre-migration pores in a sample, the group A materials show an increase in median equivalent circular diameter with increasing calcite with a correlation coefficient of 0.53 ($R^2 = 0.28$). Group B samples show a similar trend with pre-migration median pore sizes for all pores in a sample increasing with calcium but with a steeper slope and a slightly higher correlation coefficient of 0.76 ($R^2 = 0.58$). Matrix pores show the same trends, group A samples with a correlation coefficient of 0.87 ($R^2 = 0.62$) and group B samples with a correlation coefficient of 0.81 ($R^2 = 0.65$).

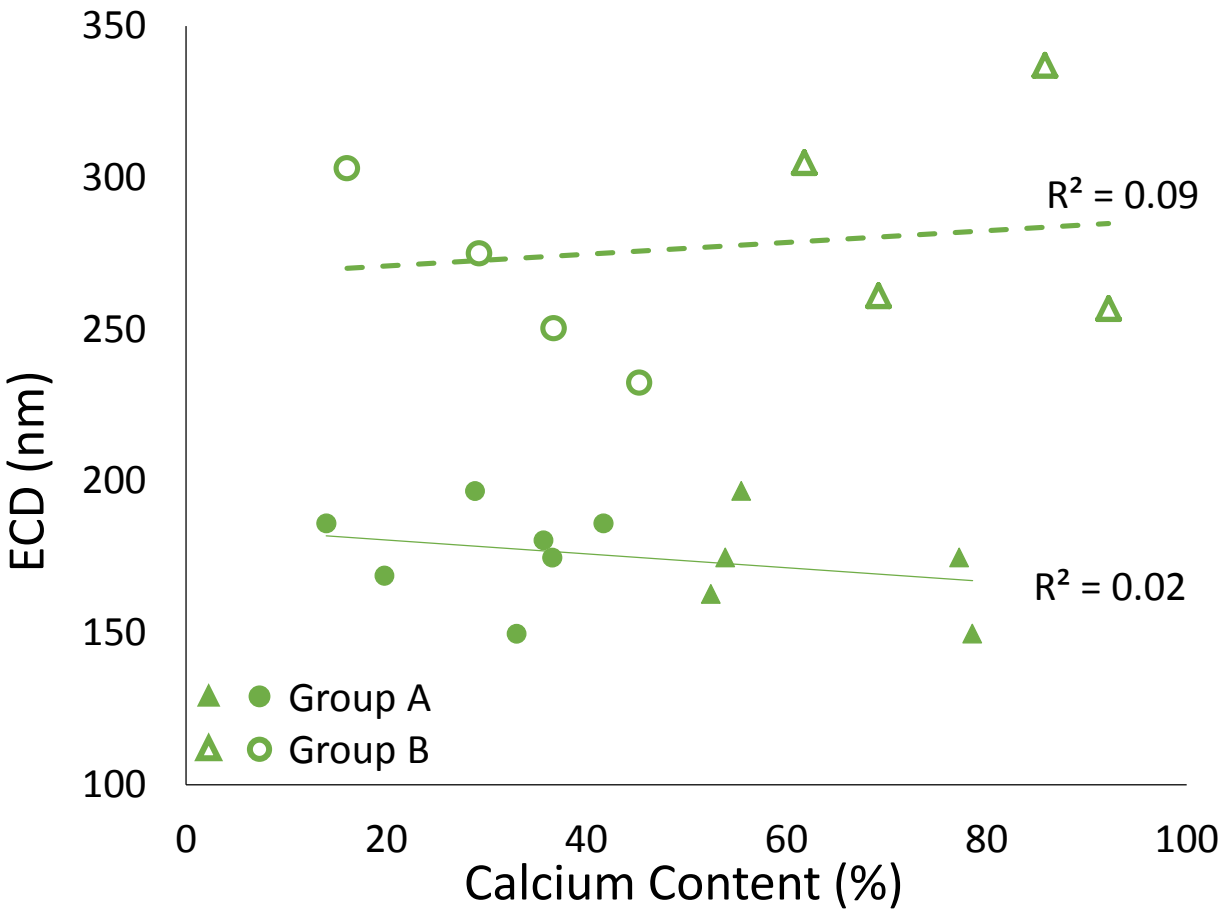

Figure 31. Median ECD of pre-migration peloid versus percent calcium (lithology). Hollow shapes for both graphs are group B samples and filled shapes are group A samples. Circles represent Piceance Basin samples and triangles represent DJ Basin samples. Lines through the data sets are best fit linear regressions.

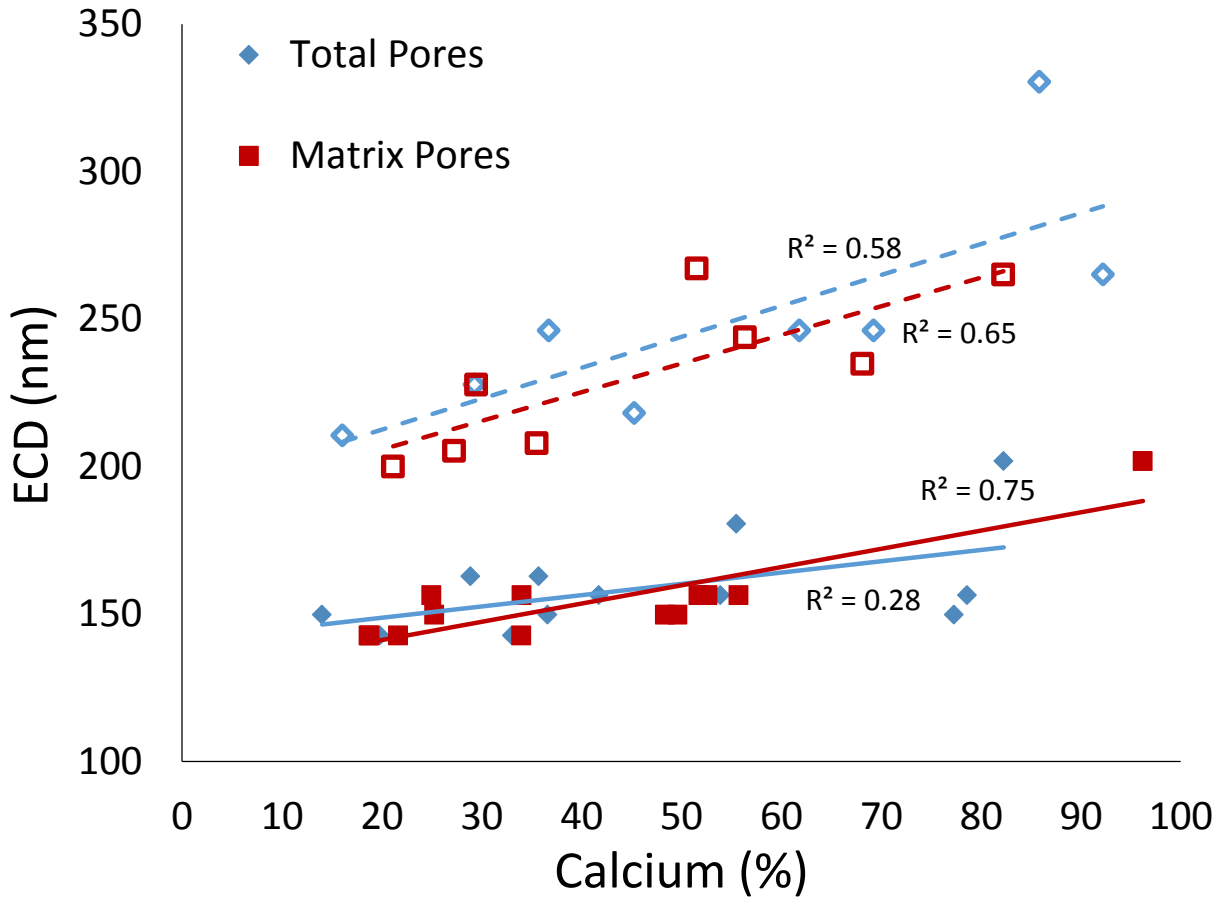

Figure 32. Median ECD of pre-migration matrix and total (matrix plus peloid) pores versus percent calcium (lithology). Hollow shapes for both graphs are group B samples and filled shapes are group A samples. . Lines through the data sets are best fit linear regressions.

Pre-migration pore widths measure the length of the shortest vector that can be drawn within the bounds of a pore and therefore are a proxy for pore-throat diameter. Again, matrix and all pores show a positive covariance between widths and lithology (Fig. 33), but peloid pores do not (Fig. 34). Matrix pores show the strongest correlations (group A, R = 0.81, R^2 = 0.65; group B, R =0.74, R^2 = 0.55). When considering all pores, the group A samples have a weaker correlation between pre-migration widths and lithology (R = 0.35, R^2 = 0.12), but group B samples show a strong correlation (R = 0.75, R^2 = 0.57).

Pre-Migration Pore Shape

The shape of pores is characterized by anisotropy, the ratio of the shortest vector inside a pore to the longest vector normal to the shortest vector. Objects with lower anisotropy value are less elongate (more equant) than objects with large anisotropy values.

As with pore sizes, samples from groups A and B show similar population distributions of pre-migration pore shape, but absolute values differ between the two groups (Fig. 35). Group A samples are more negatively skewed (more values with larger anisotropy) and exhibit stronger kurtosis than group B samples. In both the group A and group B samples, the greatest percentage of pre-migration pores (about 30% to 40%) occur within the 0.8-1.0 anisotropy ranges. Samples in group A show a consistent trend of increasing pore anisotropy with shalier lithologies with proportions in the 0.9-1.0 bin of 28.4%-34.4% for marly chalk samples, 28.1%-37.5% for marl samples, and 30.1%-41.6% for marly shale samples (Fig. 35A). Samples in group B also show a consistent trend of increasing pore anisotropy with shalier lithologies with proportions in the 0.8 to 1.0 bins of 26.3% to 33.8% for chalks, 29.9% to 34.0% for marly chalks,

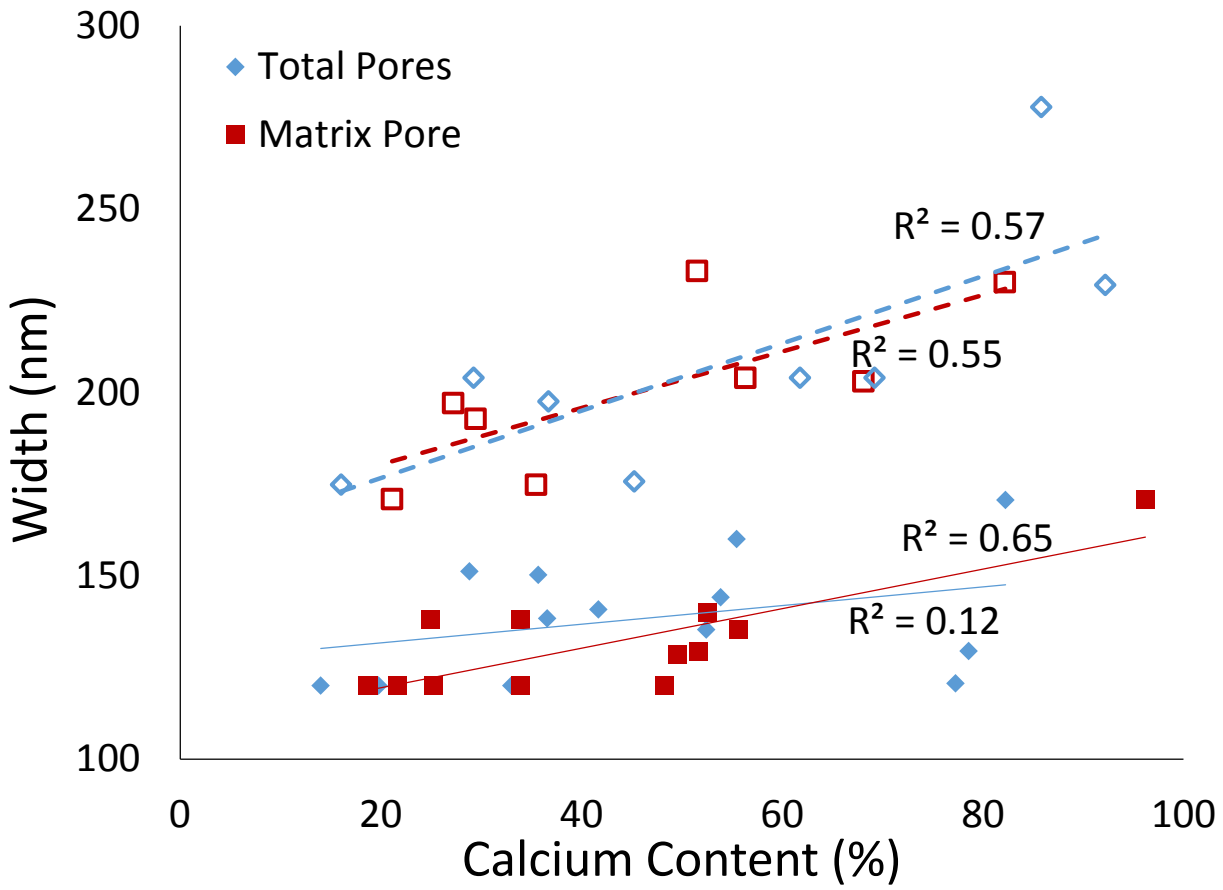

Figure 33. Median widths of pre-migration matrix and total (matrix plus peloid) pores versus percent calcium (lithology). Hollow shapes for both graphs are group B samples and filled shapes are group A samples. Lines through the data sets are best fit linear regressions.

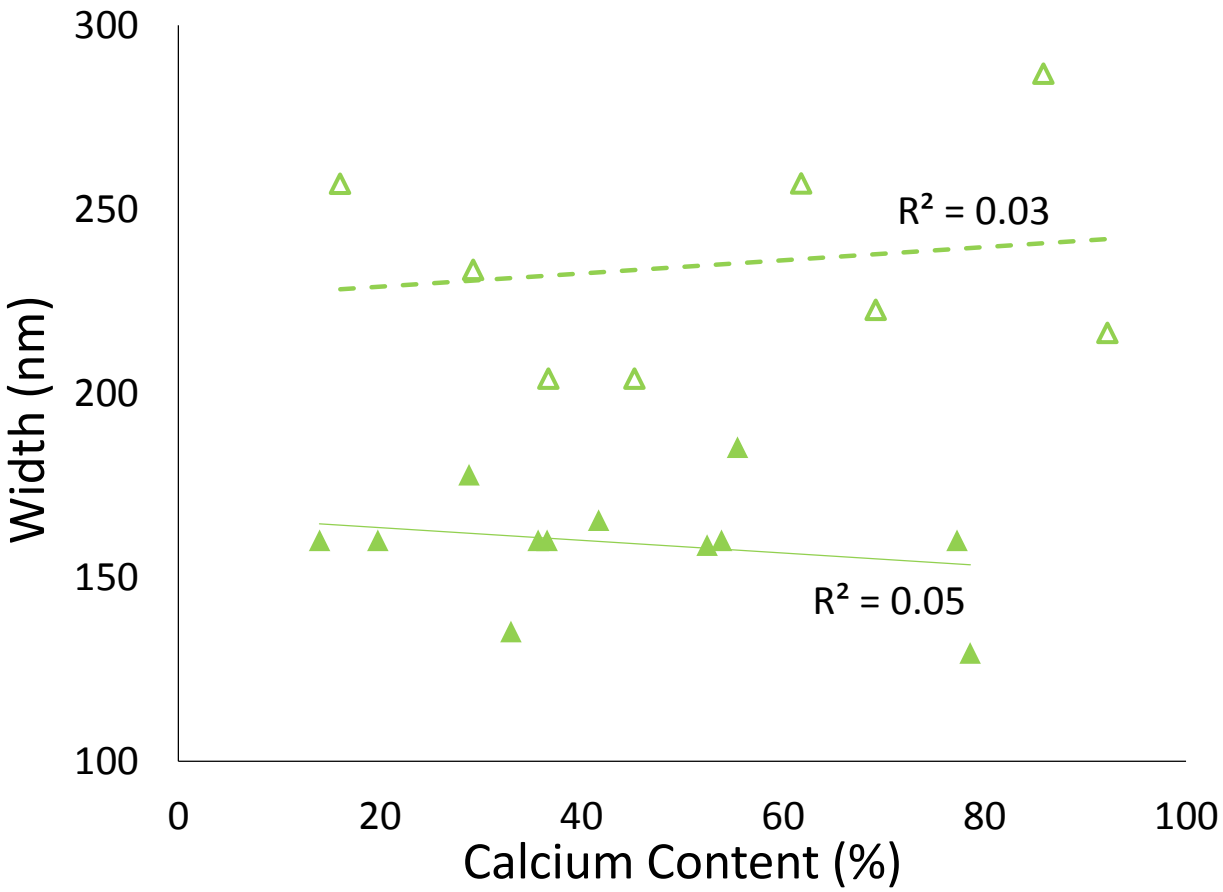

Figure 34. Median pre-migration pore widths of peloid pores versus percent calcium (lithology). Hollow shapes for both graphs are group B samples and filled shapes are group A samples. Lines through the data sets are best fit linear regressions.

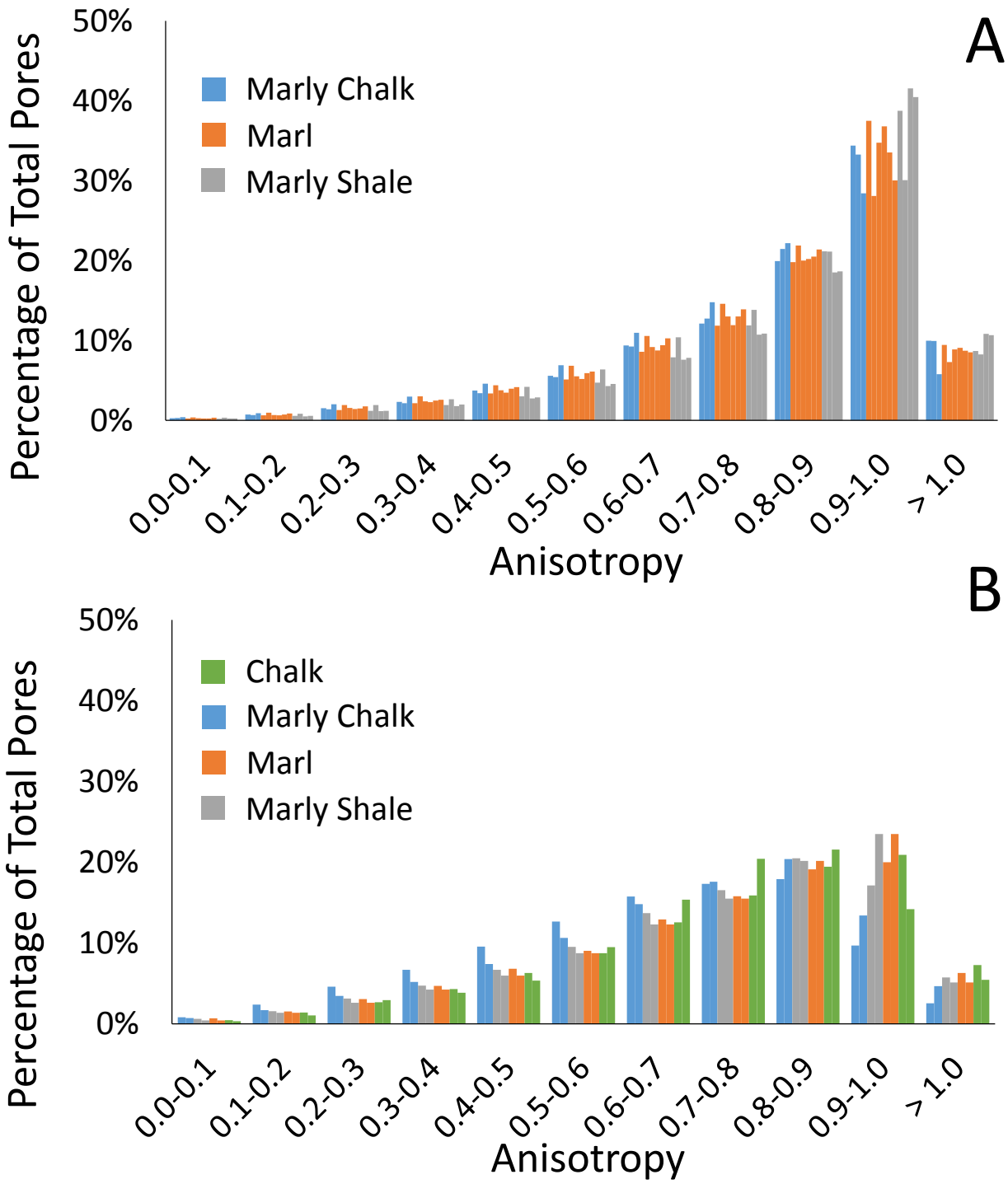

Figure 35. Histograms of percentage-normalized pre-migration pore-shape (anisotropy) for total (peloid plus matrix) pores in group A (A) and group B samples (B). Green bars are chalks, blue bars are marly chalks, orange bars are marls, and gray bars are marly shales.

33.8% to 35.1% for marls, and 31.2% to 37.1% for marly shales (Fig. 35B). In both groups, peloids (Fig. 36) show greater proportions of equant pores than matrix material (Fig. 37).

Median pre-migration anisotropy values of all pores and matrix pores exhibit more equant pore shapes with increasing calcite (Fig. 38). Group A matrix pores show a very strong inverse correlation between anisotropy and matrix calcite ($R = 0.91$, $R^2 = 0.82$). Group B matrix pores show a similar trend with a slightly smaller correlation coefficient of 0.73 ($R^2 = 0.53$). All pores in group A samples show only a moderate correlation to lithology with a correlation coefficient of 0.48 ($R^2 = 0.23$). All pores in group B samples exhibit a better correlation to lithology with a correlation coefficient of 0.76 ($R^2 = 0.58$). Pre-migration peloid pore shape variation is not correlated to lithology (Fig. 39) which is not surprising given that pores types in the calcitic peloids are consistently the same intercrystalline network in all lithologies.

Pre-Migration Orientation

Rose diagrams for pre-migration pore orientations in representative samples of a chalk, marly chalk, marl, and shaly marl matrices (Fig. 40) show an increasing abundance of near horizontal pores with increasing shaliness. Every sample has pores orientated in every possible direction, but chalk samples are more likely to have <50% of all pores near horizontal, whereas shaley marls are most likely to have >55% of all pores near horizontal. These lithologic differences are seen more clearly when the percentage of pores orientated within 30° of horizontal (referred to here as horizontality) are compared to total calcium and matrix calcium for groups A and B (Fig. 41, Table 4). Decreasing horizontality occurs with increasing calcium. Group A shows correlation coefficients of 0.41 ($R^2 = 0.17$) and 0.69 ($R^2 = 0.48$) for all pores and matrix pores, respectively. Group B shows correlation coefficients of 0.49 ($R^2 = 0.24$) and 0.74

Table 4. Complete list of 21 high-graded samples, their lithologies and horizontality measurements by fabric element. * No discernable peloids in this sample. C = Chalk MC = Marly Chalk M = Marl MS = Marly Shale

			Horizontality		
Well	Depth	Lithology	Total	Matrix	Peloid
Timbro	5666	MC	56.91%	58.11%	50.30%
Timbro	5680.7	MC	42.31%	42.56%	41.21%
Timbro	5703.3	C	51.26%	52.09%	50.56%
Timbro	5724.2	C	40.84%	40.76%	41.41%
Timbro	5758	M	54.04%	54.20%	49.37%
Timbro	5799.5	MC	52.49%	53.51%	47.95%
Timbro	5813.6	M	43.69%	47.97%	42.41%
Timbro	5823.4	MC	47.64%	47.95%	46.17%
Timbro	5835.7	M	46.27%	47.43%	42.46%
Timbro	5902	MC	35.17%	35.17%	*
#5	7638	M	46.69%	50.28%	41.04%
#5	7750	MS	52.72%	53.20%	41.67%
#5	7645	M	64.65%	65.68%	59.94%
#5	8000	M	54.34%	54.34%	44.31%
#5	8382	MS	48.09%	51.33%	43.34%
#5	8390	MS	49.05%	49.62%	46.42%
#4	10010.66	MS	54.13%	54.55%	49.05%
#4	10045.13	M	49.71%	53.64%	49.71%
#4	10142.78	MS	55.48%	56.19%	49.92%
#4	10251.92	M	50.86%	54.54%	47.71%
#4	10380.3	MS	54.82%	60.72%	45.07%

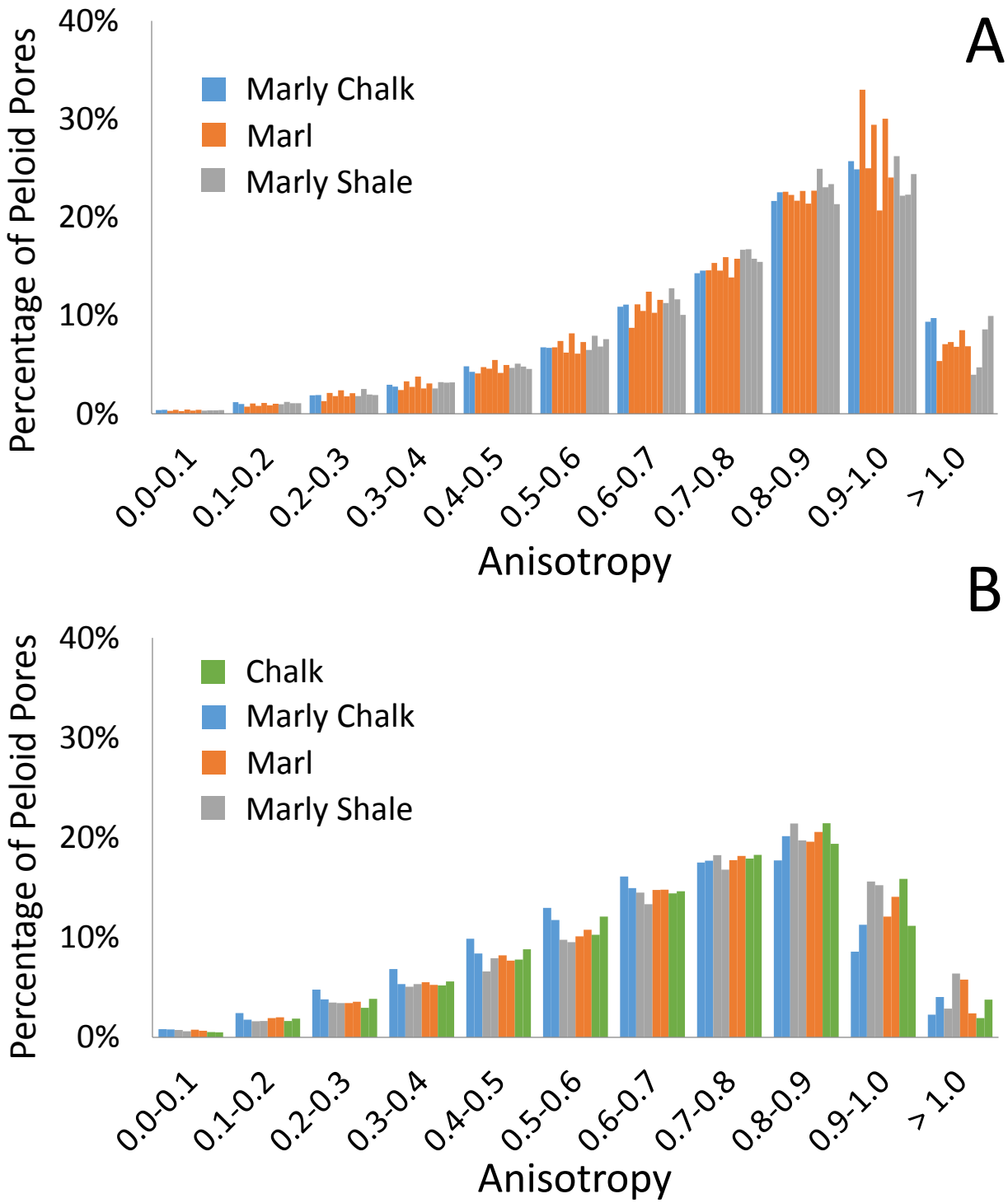

Figure 36. Histograms of percentage-normalized pre-migration pore-shape (anisotropy) for peloid pores in group A (A) and group B samples (B). Green bars are chalks, blue bars are marly chalks, orange bars are marls, and gray bars are marly shales.

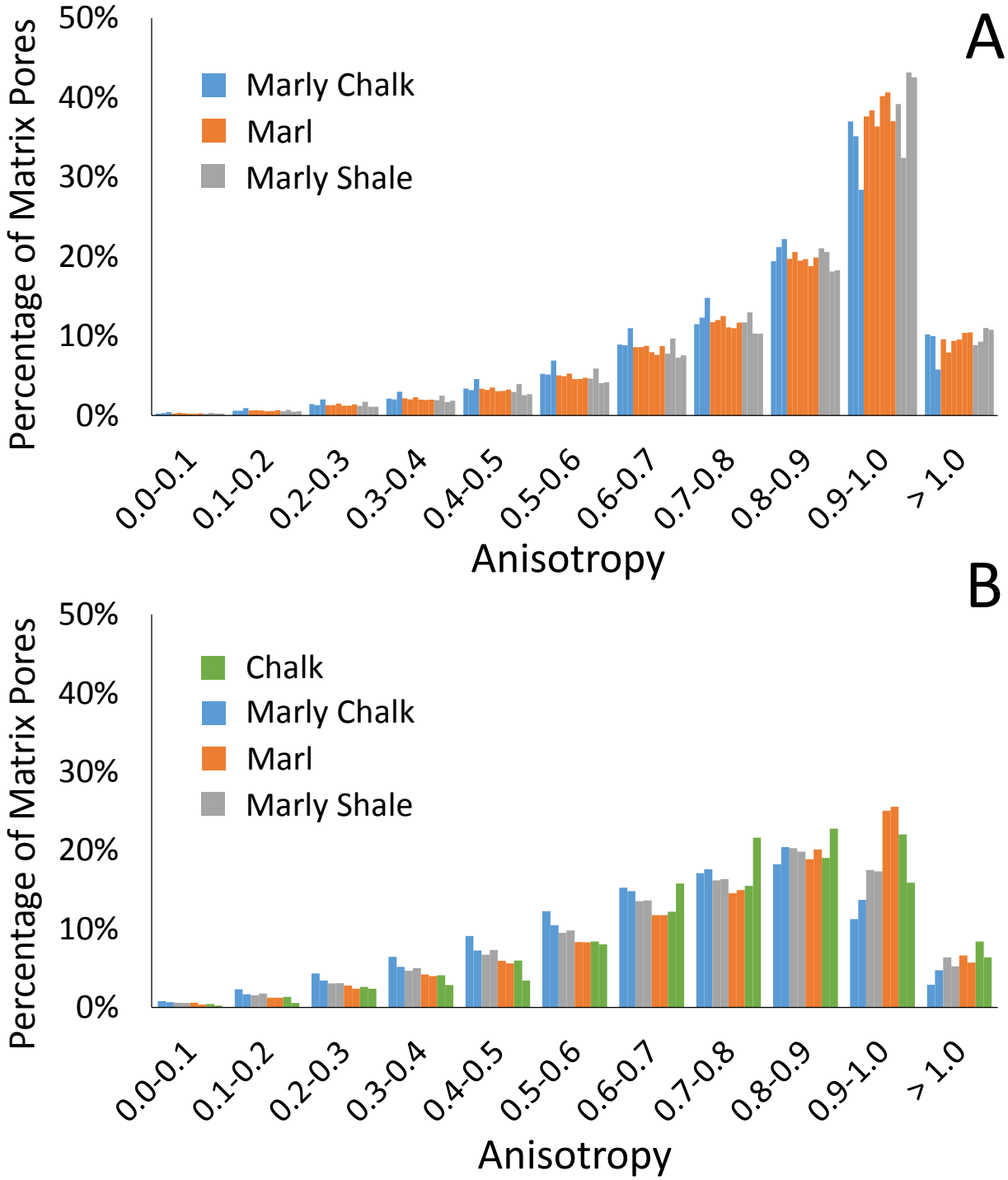

Figure 37. Histograms of percentage-normalized pre-migration pore-shape (anisotropy) for matrix pores in group A (A) and group B samples (B). Green bars are chalks, blue bars are marly chalks, orange bars are marls, and gray bars are marly shales.

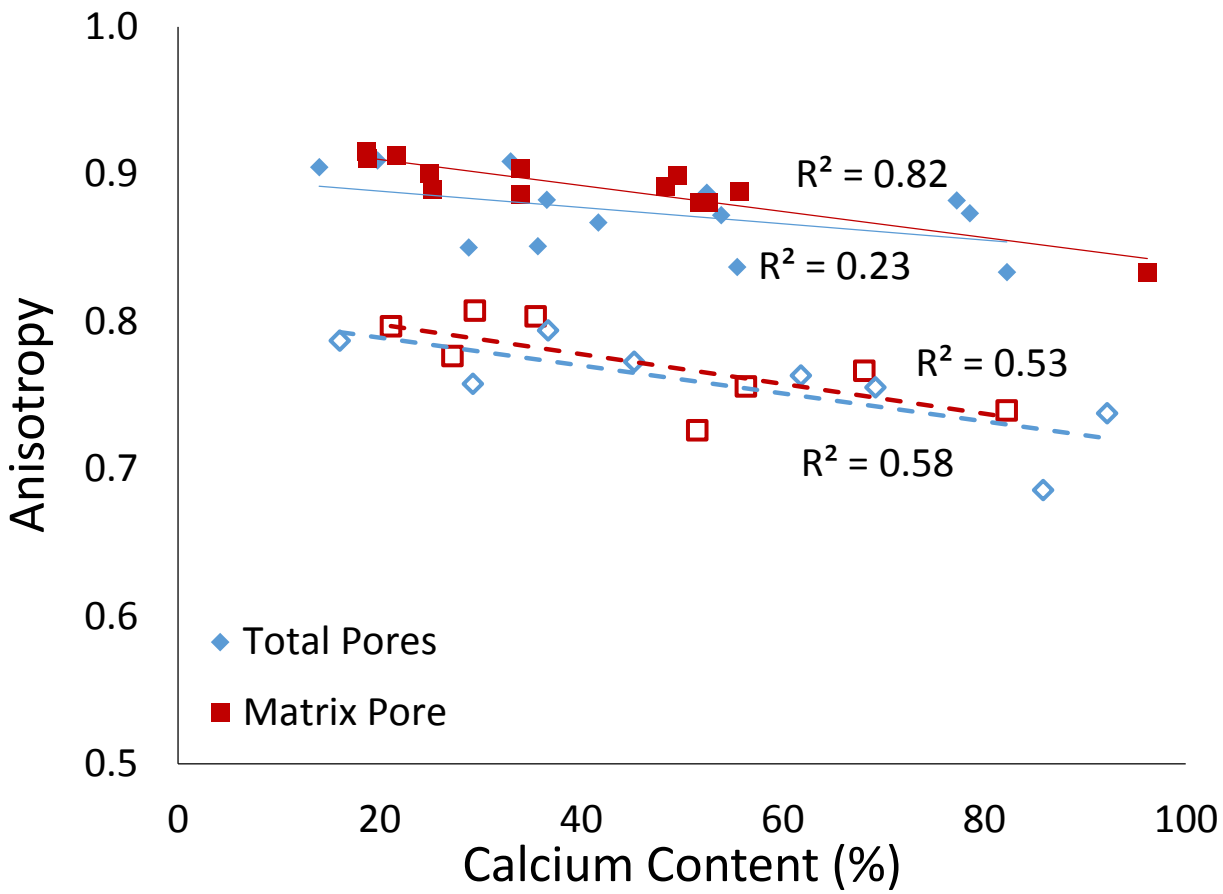

Figure 38. Median pre-migration matrix and total (matrix plus peloid) pore shapes (anisotropy) versus percent calcium (lithology). Hollow shapes are group B samples and filled shapes are group A samples. Lines through the data sets are best fit linear regressions.

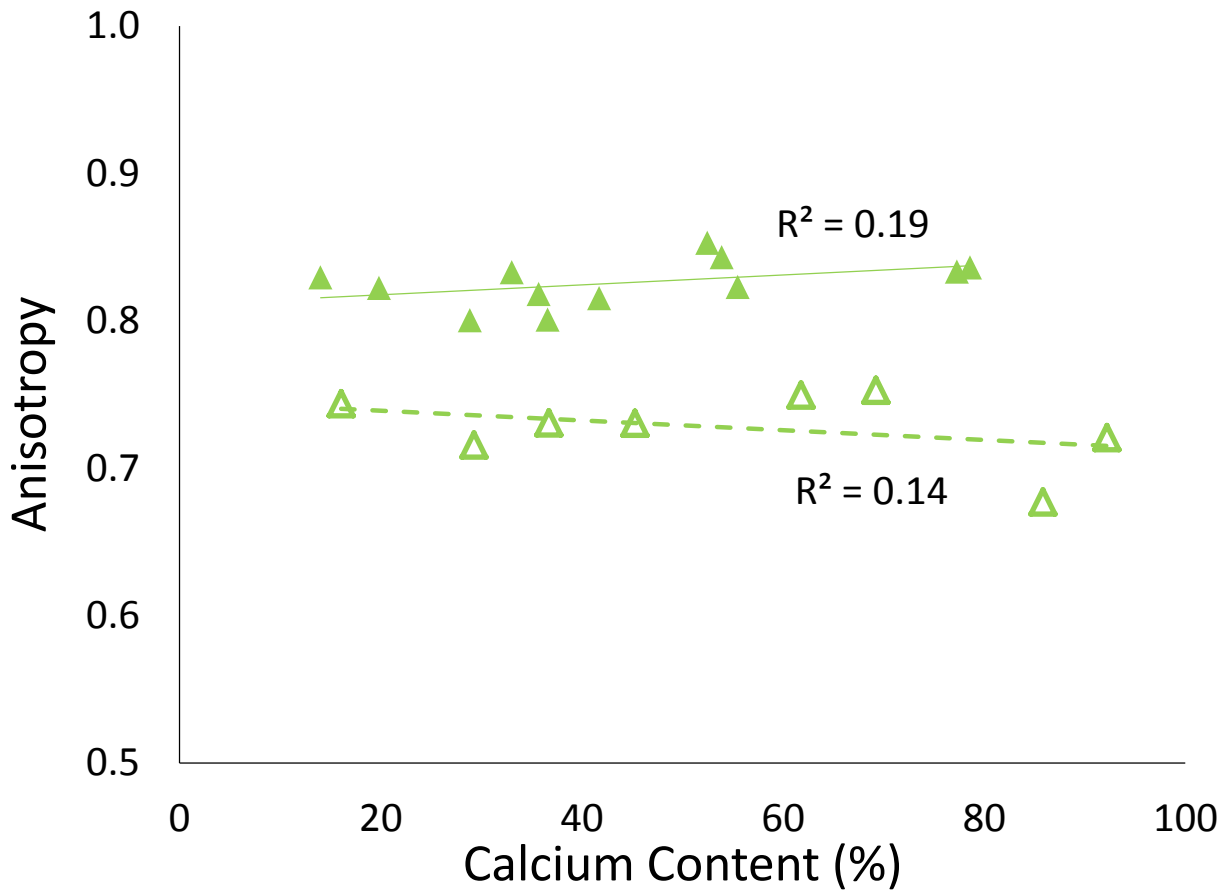

Figure 39. Median pre-migration peloid pore shapes (anisotropy) versus percent calcium (lithology). Hollow shapes for both graphs are group B samples and filled shapes are group A samples. Lines through the data sets are best fit linear regressions.

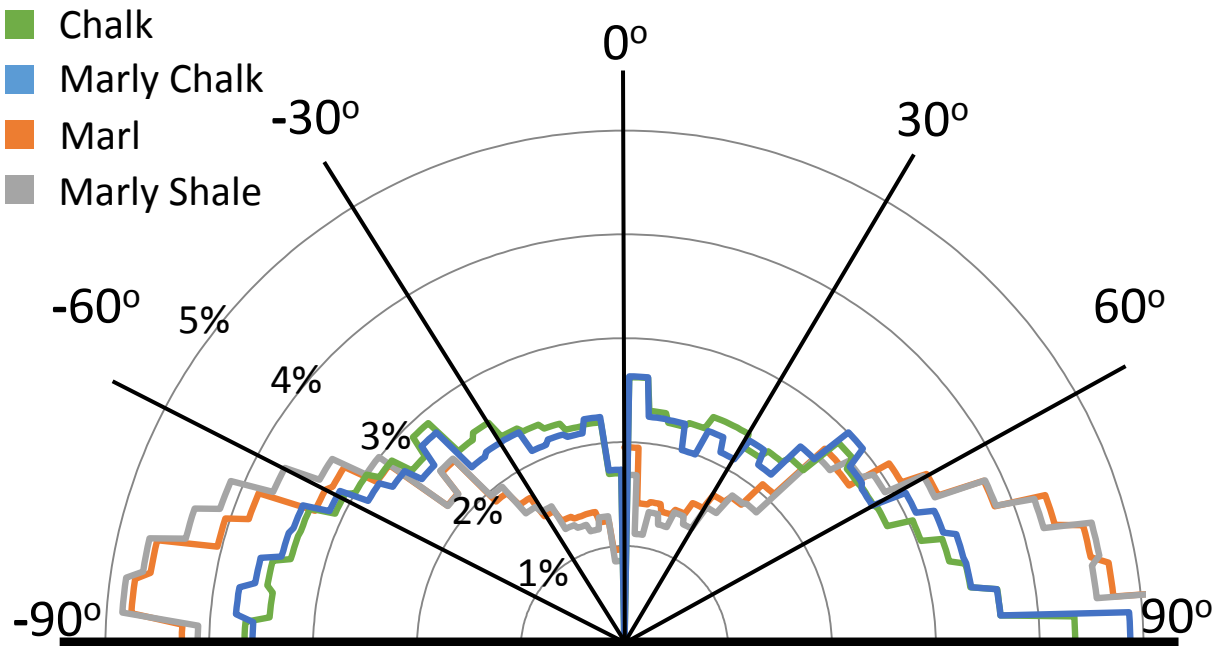

Figure 40. Half-rose diagram of preferred pre-migration matrix pore orientations in representative samples of each lithology. Radial values show the orientation of the longest pore axis (normalized to percent of all measured axes in the sample) binned in 5° increments. The chalk sample is Timbro, 5724. The marly chalk sample is Timbro 5680. The marl sample is well #4, 10251. The shaley marl sample is well #4, 10142.

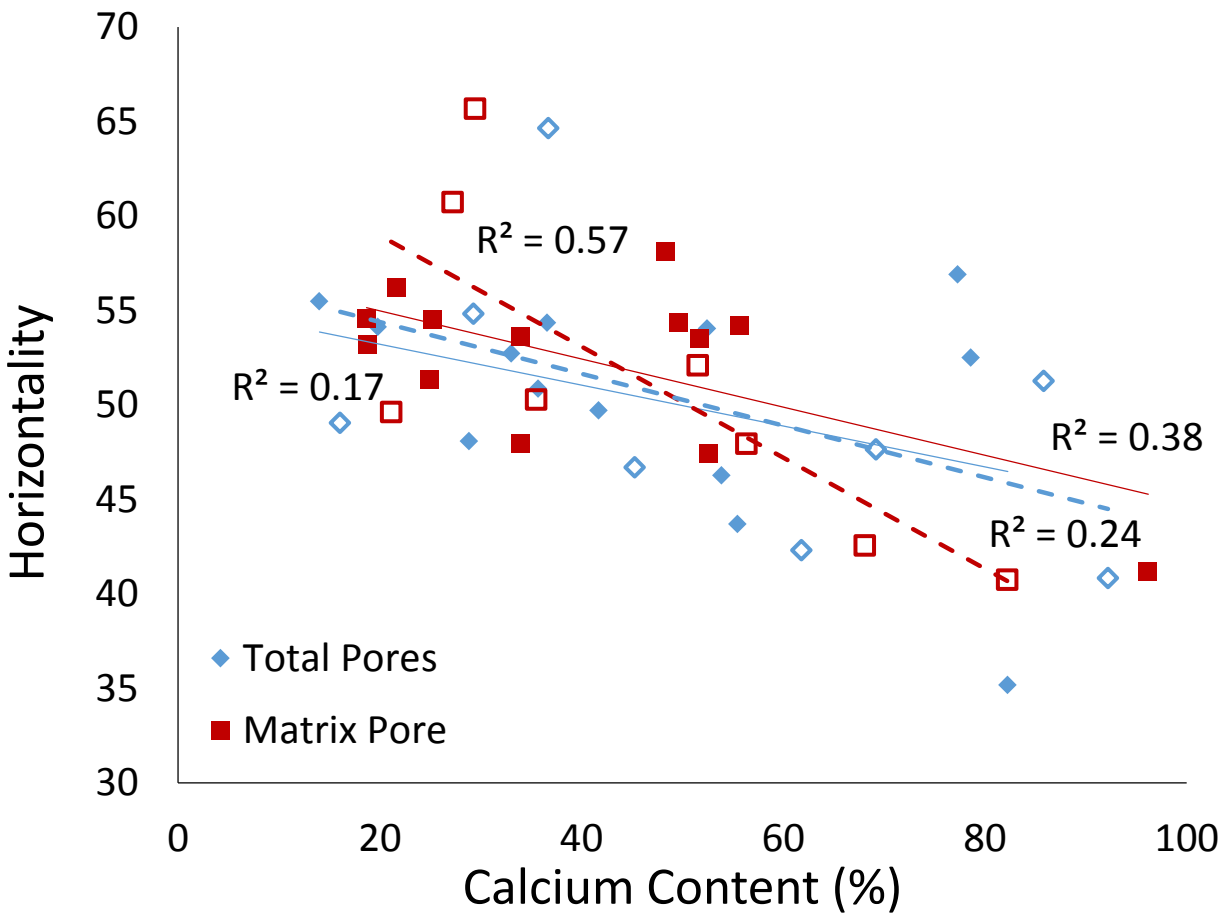

Figure 41. Median pre-migration matrix and total (matrix plus peloid) pore horizontality versus percent calcium (lithology). Hollow shapes for both graphs are group B samples and filled shapes are group A samples. Lines through the data sets are best fit linear regressions.

(R^2 = 0.57) for all pores and matrix pores, respectively. In both groups, the strong correlations between lithology and orientation in the matrix reflects the abundance of clay-related pores in the matrix. The correlations diminish in strength (lower r values) for all pores because that categorization includes pores in peloids which are not as preferentially horizontal. Peloid pores, in fact, show a relatively consistent horizontal preference regardless of lithology (Fig. 42; group A R^2 = 0.00, group B R^2 = 0.05).

Pore Variability by Microfacies

Microfacies do not correlate well to lithology; meaning a single microfacies may associate with two or even three different lithologies (Fig. 43). This occurs because mineralogy was not considered in the definition of microfacies. They were defined on the basis of visually estimated proportions of sand, silt and clay (Fig. 18). Yet the results presented above show that pore network attributes are highly sensitive to lithology. Thus, assessing whether or not microfacies also influences pore network requires that lithology be controlled. The four dominant microfacies were each only sampled in two of the observed lithologies (marls and shaley marls, Fig. 43), thus only the pore attributes of those samples (lithologies) are considered in the assessment of microfacies' influence on pore attributes.

Median pre-migration pores sizes and shapes by microfacies are given in Table 3. Those attributes show very little variation as a function of microfacies in the marls and marly shales. When total pores (matrix plus peloid) are considered, median sizes (Fig. 44), shapes (Fig. 45), and horizontality (Fig. 46) almost completely overlap. The silty microfacies do display slightly smaller, more elongate, and more horizontally aligned pores relative to the peloid packstone samples, but these differences can be attributed to different peloid abundance, and hence

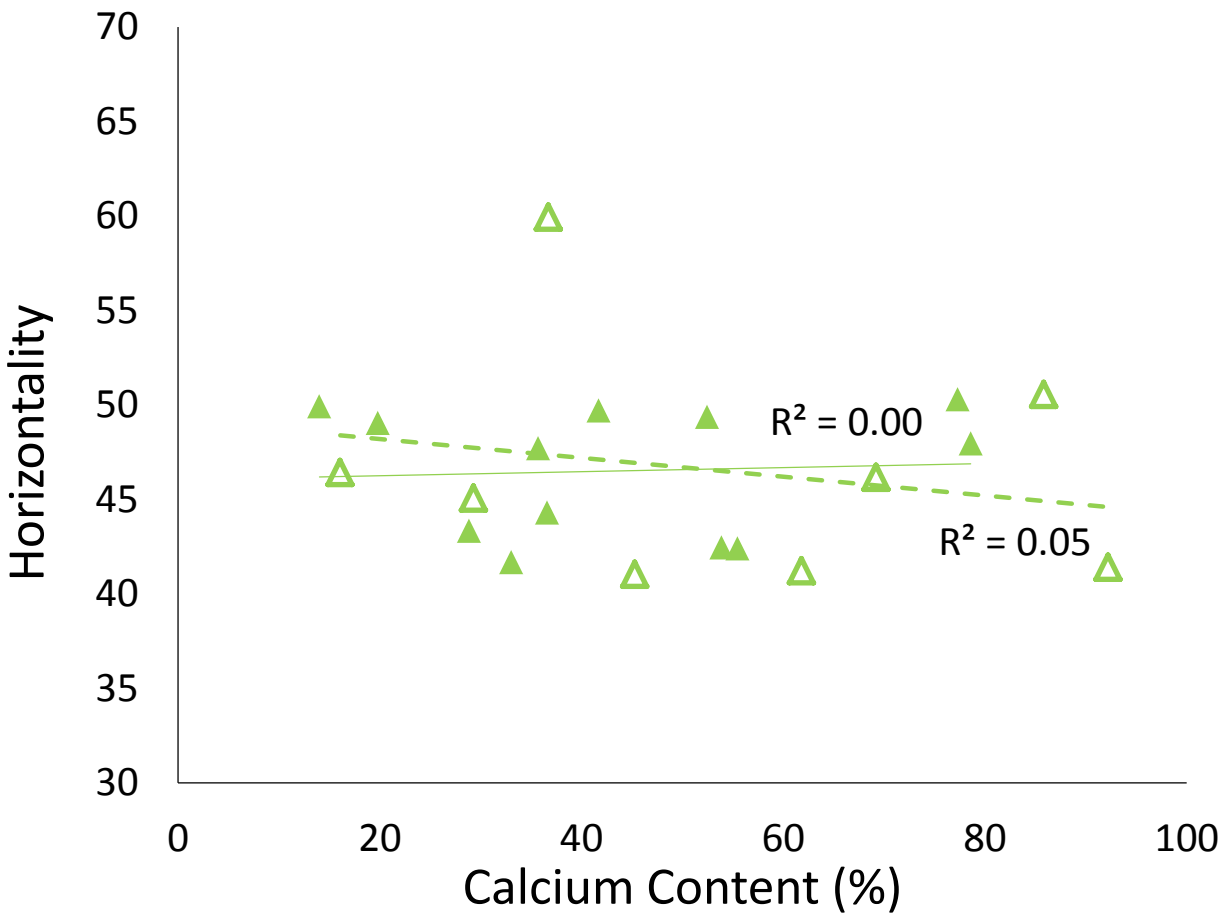

Figure 42. Median pre-migration peloid pore horizontality versus percent calcium (lithology). Hollow shapes are group B samples and filled shapes are group A samples. Lines through the data sets are best fit linear regressions.

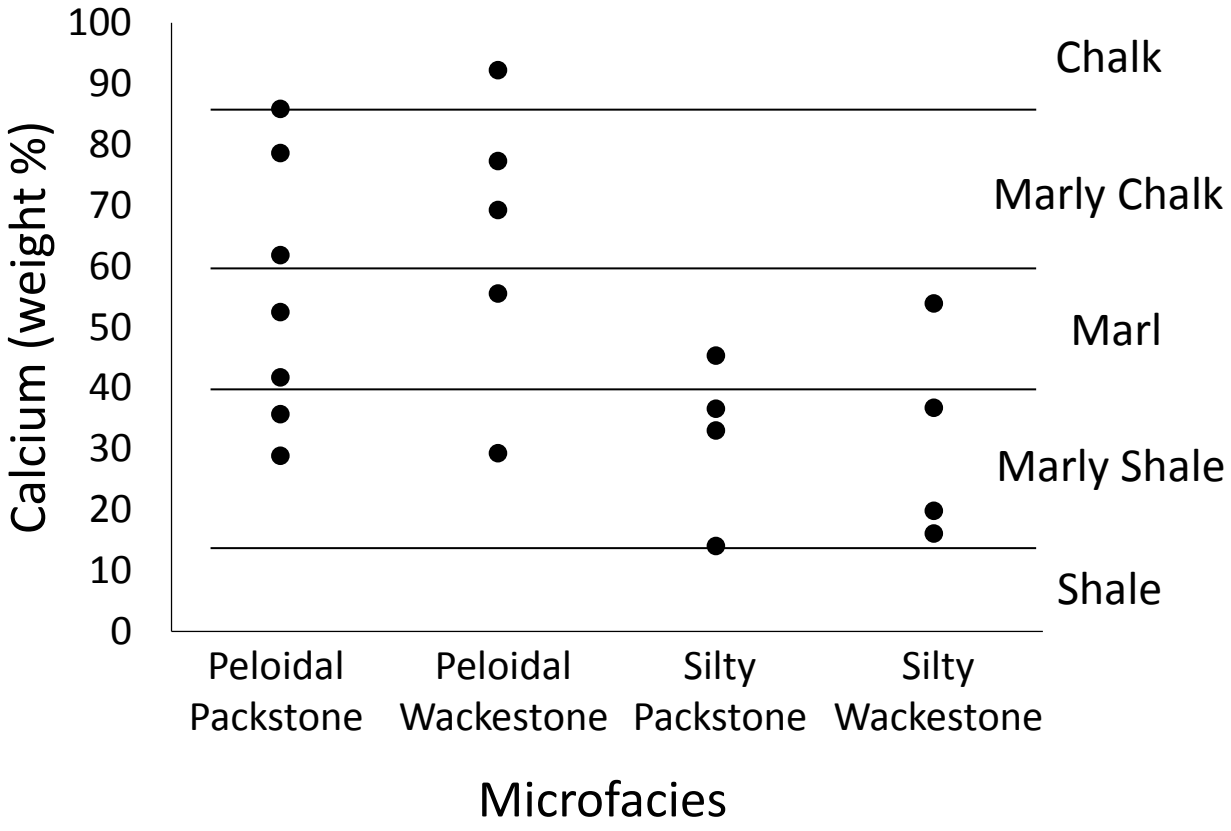

Figure 43. Microfacies distribution by lithofacies for the 21 SEM-highgraded samples. Only the marl and marly shale lithologies show a complete range of observed microfacies.

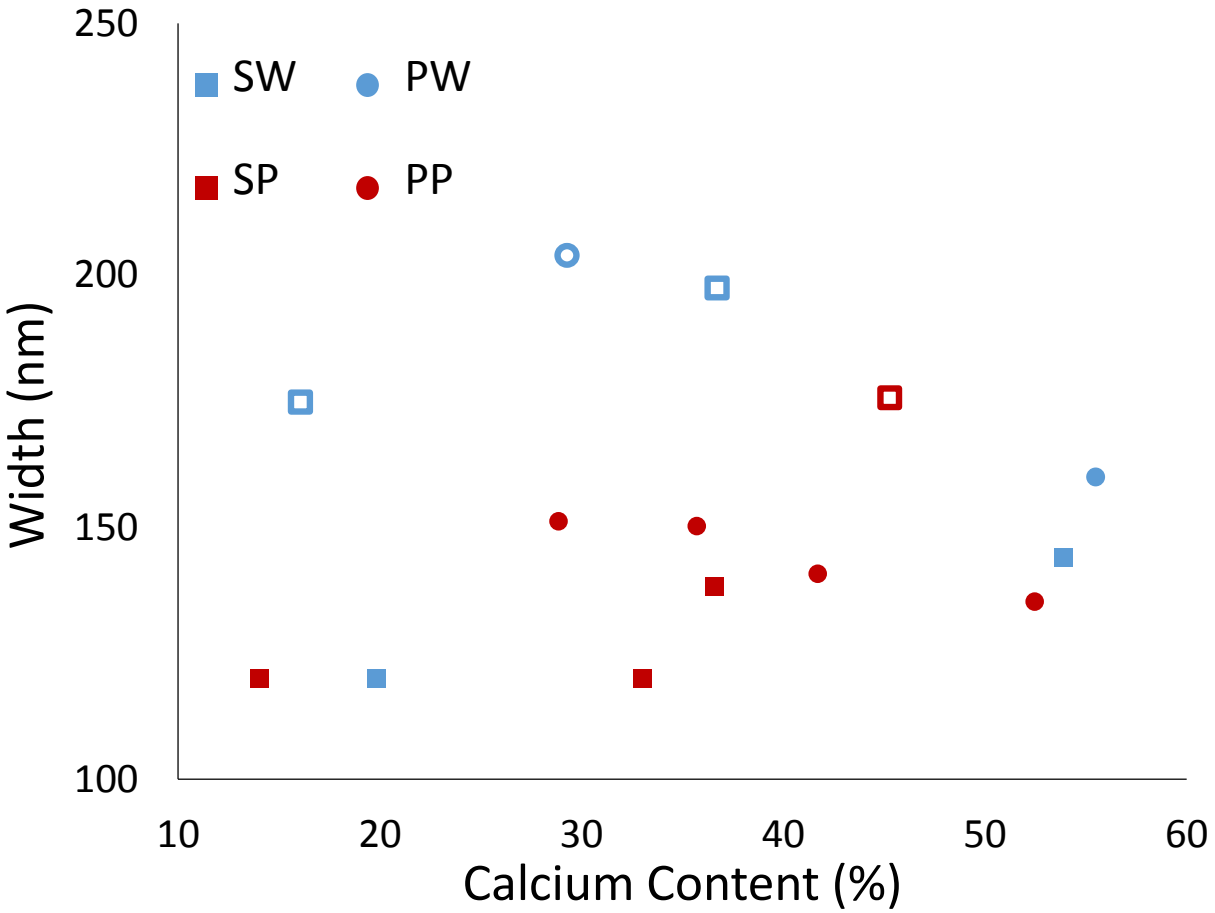

Figure 44. Median pre-migration total (peloid plus matrix) pore width versus percent calcium (lithology) for all marl and shaley marl samples. Hollow shapes are group B samples and filled shapes are group A samples. SW = silty wackestone. SP = silty packstone. PW = peloidal packstone. PP = peloidal packstone.

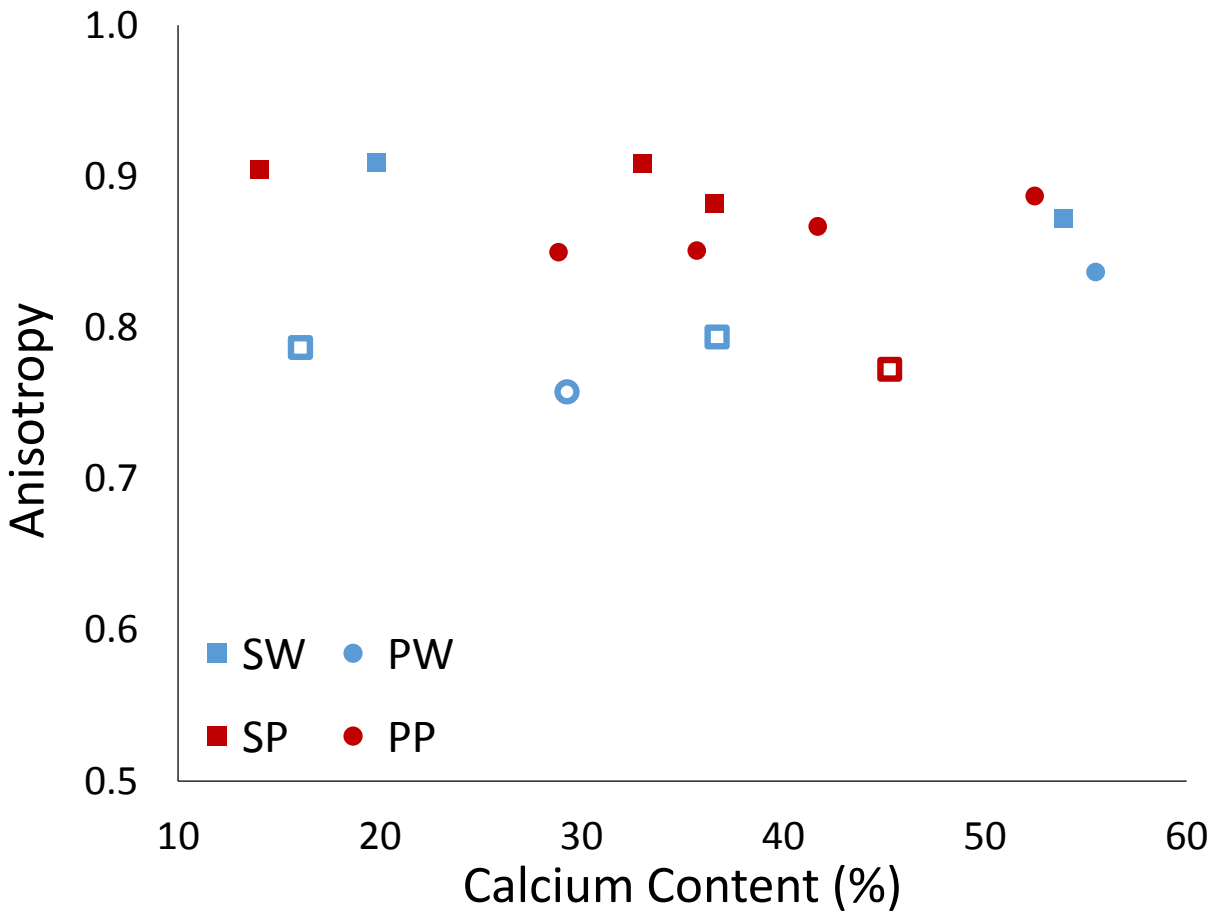

Figure 45. Median pre-migration total (peloid plus matrix) pore shape (anisotropy) versus percent calcium (lithology) for all marl and shaley marl samples. Hollow shapes are group B samples and filled shapes are group A samples. SW = silty wackestone. SP = silty packstone. PW = peloidal packstone. PP = peloidal packstone.

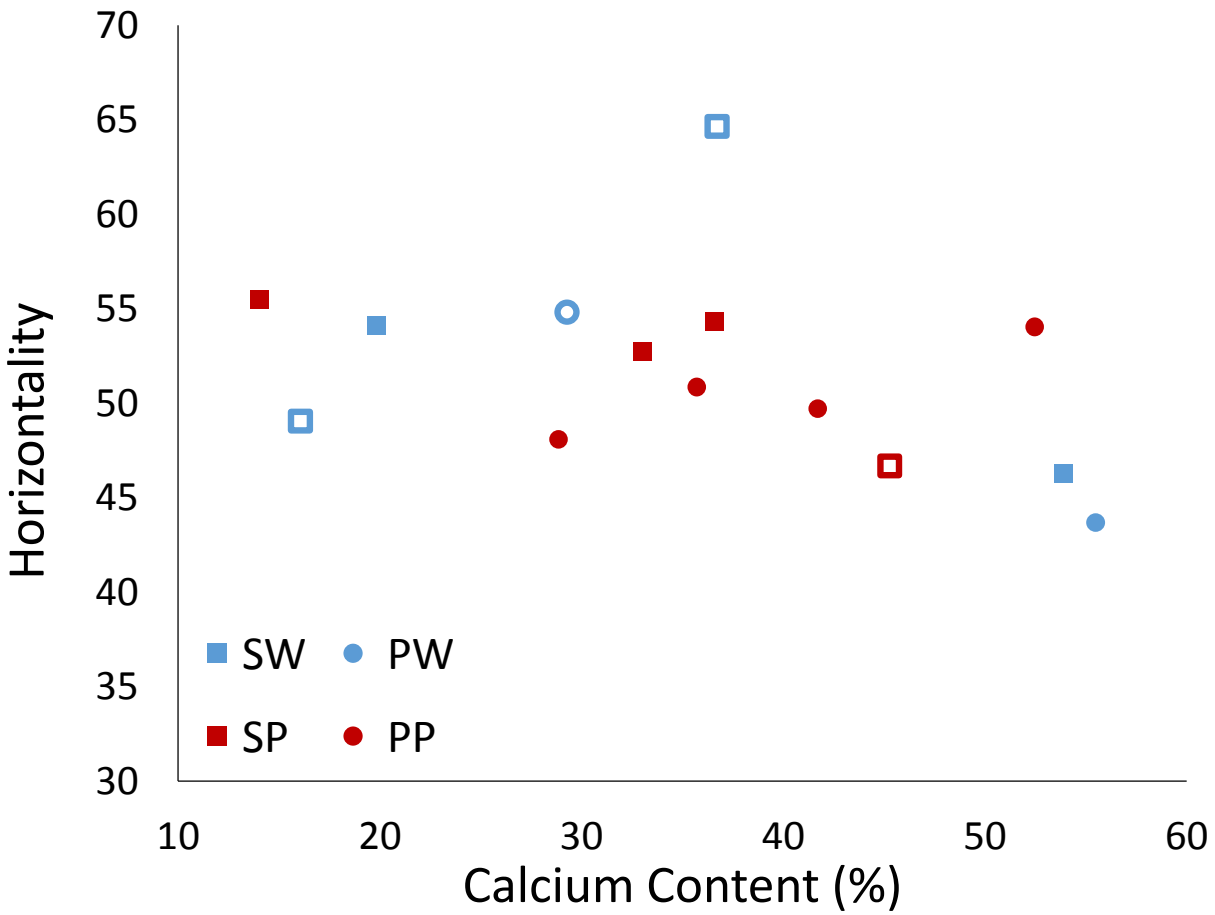

Figure 46. Median pre-migration total (peloid plus matrix) pore horizontality versus percent calcium (lithology) for all marl and shaley marl samples. SW = silty wackestone. SP = silty packstone. PW = peloidal packstone. PP = peloidal packstone.

calcite abundances. Thus pore network attributes vary more consistently with calcium percentage (Fig. 31-34, 38-39, 40-42) than with microfacies (Fig. 44-46). That is, peloid-dominated samples mimic characteristics of high calcium samples, do lithology, not microfacies is the controlling variable.

Current Porosity

Current porosity is defined for this study as the pore space not filled with migrated organic material. Its quantification requires that open pores space be easily segmented from the residual migrated hydrocarbons. That was not possible in 14 samples because gray-scale contrast between organic material and open porosity was insufficient (Fig. 47). Current porosity was thus calculated for just seven of the 21 samples (five Piceance Basin and two DJ Basin). Current porosity is compared to pre-migration and porosities for matrix, peloid, and total (matrix plus peloid) sample is shown in Table 5.

Differences between total pre-migration and current porosities represent a reduction in total porosity, assuming the residual migrated hydrocarbons are immobile, that range from 66.7% to 81.2% (average of 74.5%) of the pre-migration total porosity. Porosity reduction in peloid pores range from 51.2% to 90.0% (average of 74.2%) of the pre-migration values. In the matrix, porosity loss is 62.6% to 83.8% (average of 72.6%) of the pre-migration values. Pore sizes also change with median pore sizes (ECD) dropping 5% to 27% and median widths decreasing by 0% to 5% (Table 6). Pore shape is also affected slightly as anisotropy values for all but one of the seven samples become less equant by 1%-4% of the pre-migration values. Figures 48-50 show both the pre-migration and current porosity for the sub-set of samples as a function of lithology. Low correlation coefficients for the current porosity of the seven samples

Table 5. List of seven current porosity samples, their pre-migration, occluded, and current porosities for each fabric element. Also shown is the percentage of porosity reduction between pre-migration and current porosity.

		Pre-Migration			Occluded			Current			% Reduction		
Well	Sample	Total	Matrix	Peloid	Total	Matrix	Peloid	Total	Matrix	Peloid	Total	Matrix	Peloid
Timbro	5666	7.0%	6.5%	9.8%	5.7%	5.4%	7.1%	1.3%	1.0%	2.6%	81.2%	83.8%	73.0%
Timbro	5813	9.9%	7.0%	11.2%	7.7%	5.8%	8.6%	2.2%	1.3%	2.7%	77.6%	82.1%	76.3%
#5	8382	7.0%	5.4%	12.9%	5.6%	4.3%	6.6%	1.3%	1.1%	6.3%	80.8%	79.3%	51.2%
#4	10010	3.4%	3.0%	12.9%	2.3%	2.0%	10.6%	1.1%	1.0%	2.3%	68.6%	66.5%	81.9%
#4	10045	6.0%	3.8%	10.6%	4.0%	2.6%	6.9%	2.0%	1.2%	3.7%	66.7%	68.5%	65.2%
#4	10142	4.1%	3.5%	12.8%	2.9%	2.3%	11.5%	1.2%	1.2%	1.3%	70.4%	65.5%	90.0%
#4	10251	7.6%	3.9%	12.6%	5.8%	2.5%	10.3%	1.8%	1.5%	2.2%	76.1%	62.6%	82.1%

Table 6. List of seven current porosity samples, their total (matrix plus peloid) median pre-migration and current equivalent circular diameters (ECD), widths, and anisotropies. Also shown are the percent changes for each of these measurements from pre-migration to current pores..

Well	Sample	Median ECD	Median Current ECD	Change	Median Width	Median Current Width	Change	Median Anisotropy	Median Current Anisotropy	Change
#4	10010	142.7	135.4	5.1%	120.0	117.5	2.0%	0.91	0.92	-1.2%
#4	10045	156.4	142.7	8.7%	140.8	120.0	14.8%	0.87	0.85	1.8%
#4	10142	149.7	135.4	9.5%	120.0	120.0	0.0%	0.90	0.92	-2.0%
#4	10251	162.7	119.4	26.6%	150.2	114.1	24.0%	0.85	0.87	-2.1%
#5	8382	162.7	135.4	16.8%	151.2	120.0	20.6%	0.85	0.87	-2.2%
Timbro	5666	149.7	135.4	9.5%	120.6	115.1	4.6%	0.88	0.91	-3.7%
Timbro	5813	180.5	142.7	20.9%	160.0	120.0	25.0%	0.84	0.86	-2.5%

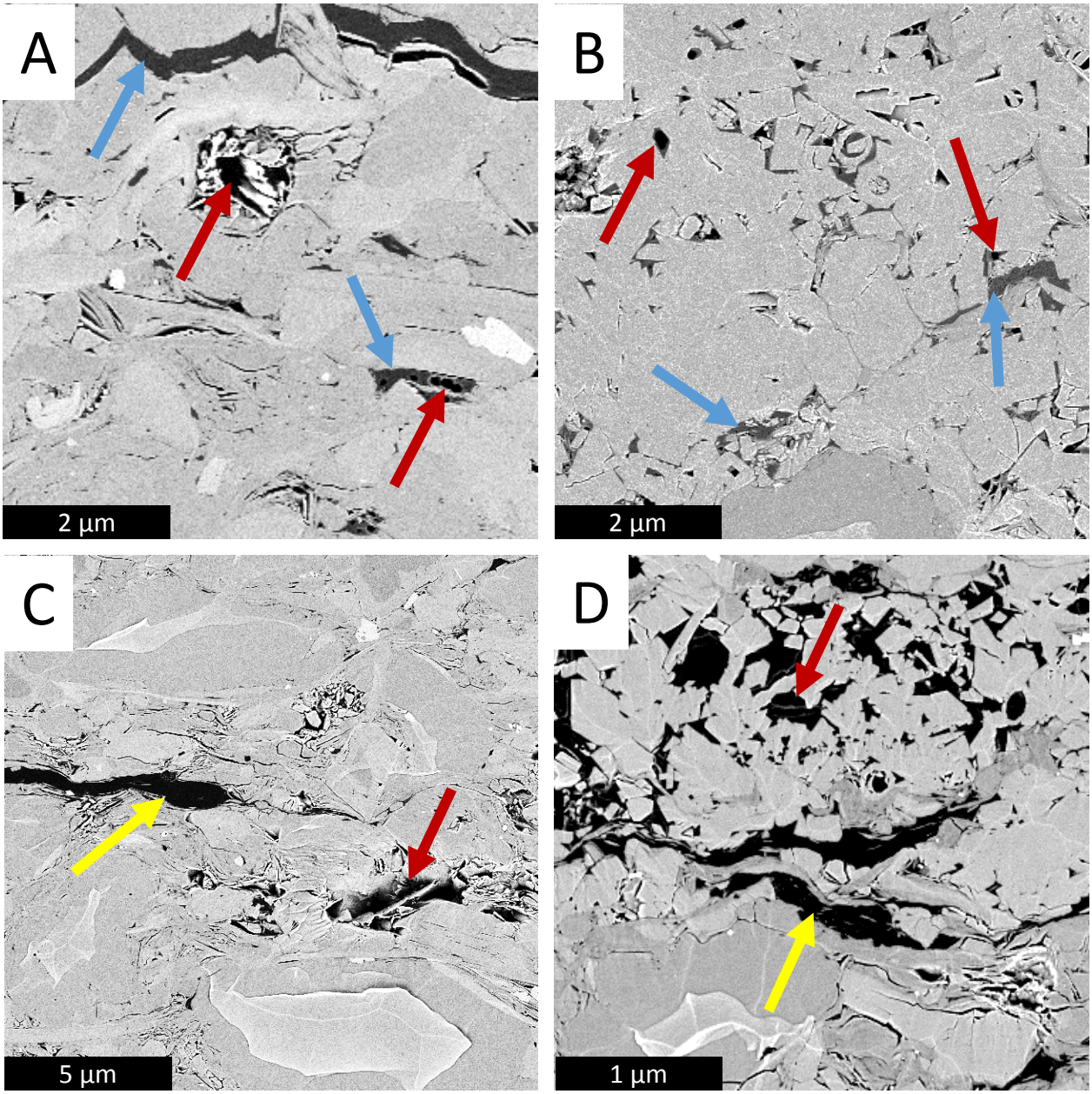

Figure 47. Backscattered SEM images of open and hydrocarbon-occluded pores from two samples in the Piceance Basin and two samples in the DJ Basin. Photos A (well #4, 10045) and B (Timbro, 5813) show adequate contrast between organic material (blue arrows) and open porosity (red arrows) to be used for segmentation of currently open pores. Photos C (well #5, 8000) and D (Timbro, 5835) display both detrital organic material, identified by morphology (yellow arrows), hydrocarbon-filled pores, and open pores. In these samples, however, there is no consistent gray-scale contrast between the three types of objects.

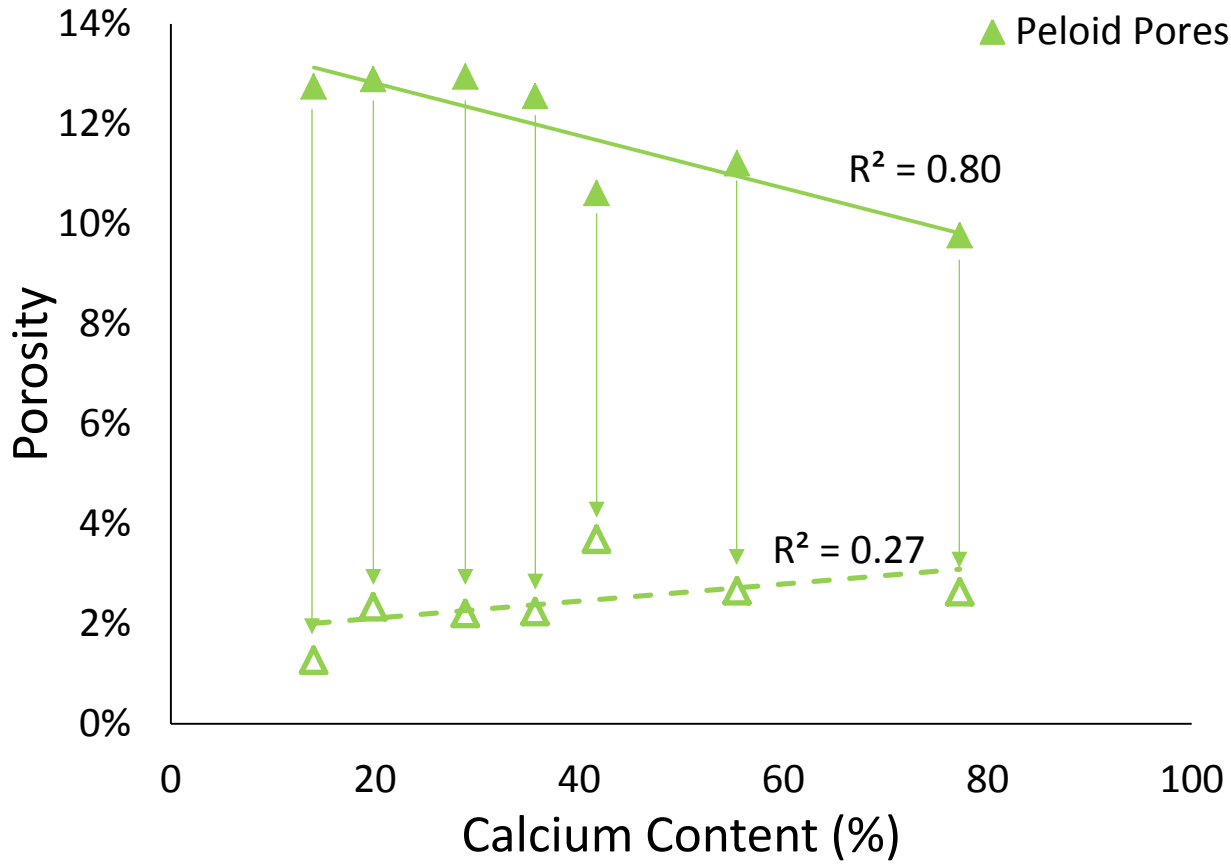

Figure 48. Pre-migration (filled symbols, solid line) and current porosity (open symbols, dashed line) for peloid material versus calcium content (lithology). Lines through the data sets are best fit linear regressions. Arrows show the change in porosity between pre-migration and post-migration. The pre-migration total porosity trend differs (in slope and correlation coefficient) from that shown in Figure 30 because of the difference in number of samples plotted (21 in Figure 27, only 7 here).

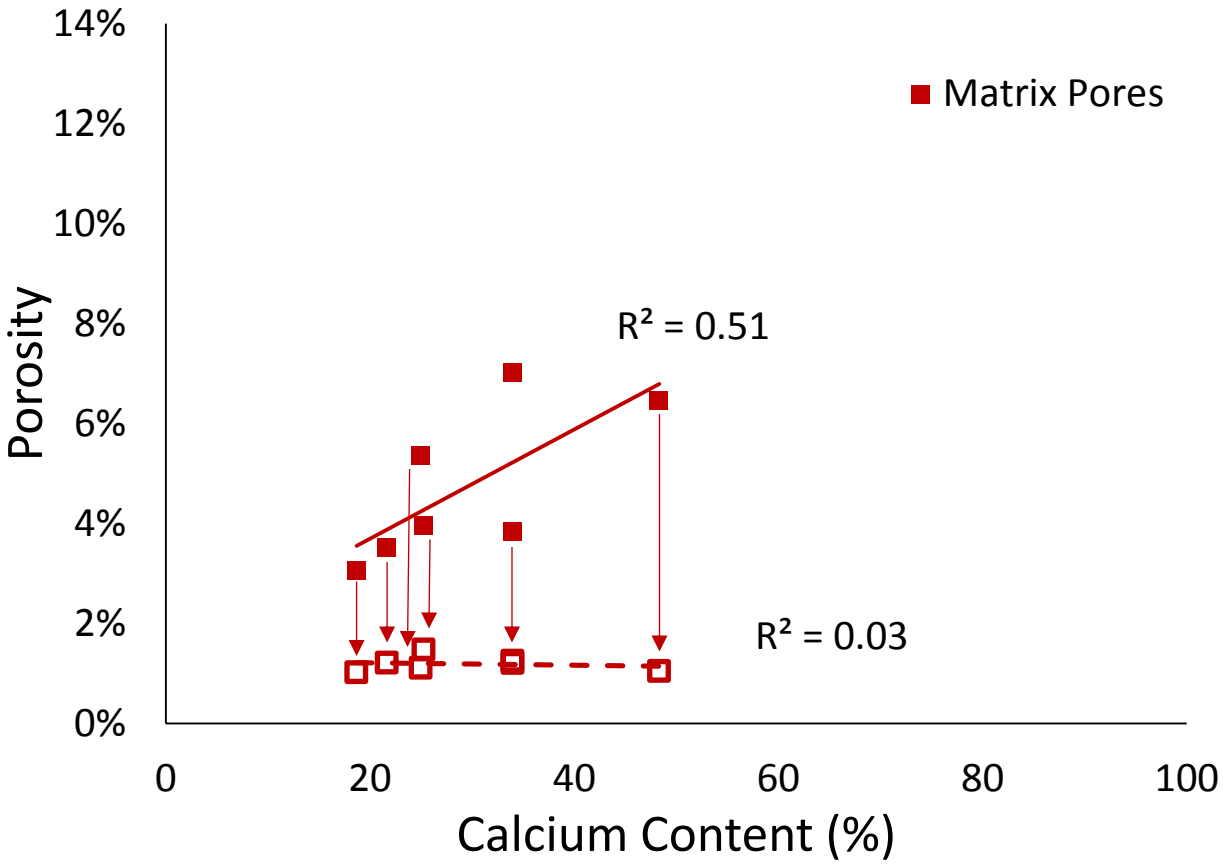

Figure 49. Pre-migration (filled symbols, solid line) and current porosity (open symbols, dashed line) for matrix material versus calcium content (lithology). Lines through the data sets are best fit linear regressions. Arrows show the change in porosity between pre-migration and post-migration. The pre-migration total porosity trend differs slightly (in slope and correlation coefficient) from that shown in Figure 30 because of the difference in number of samples plotted (21 in Figure 27, only 7 here).

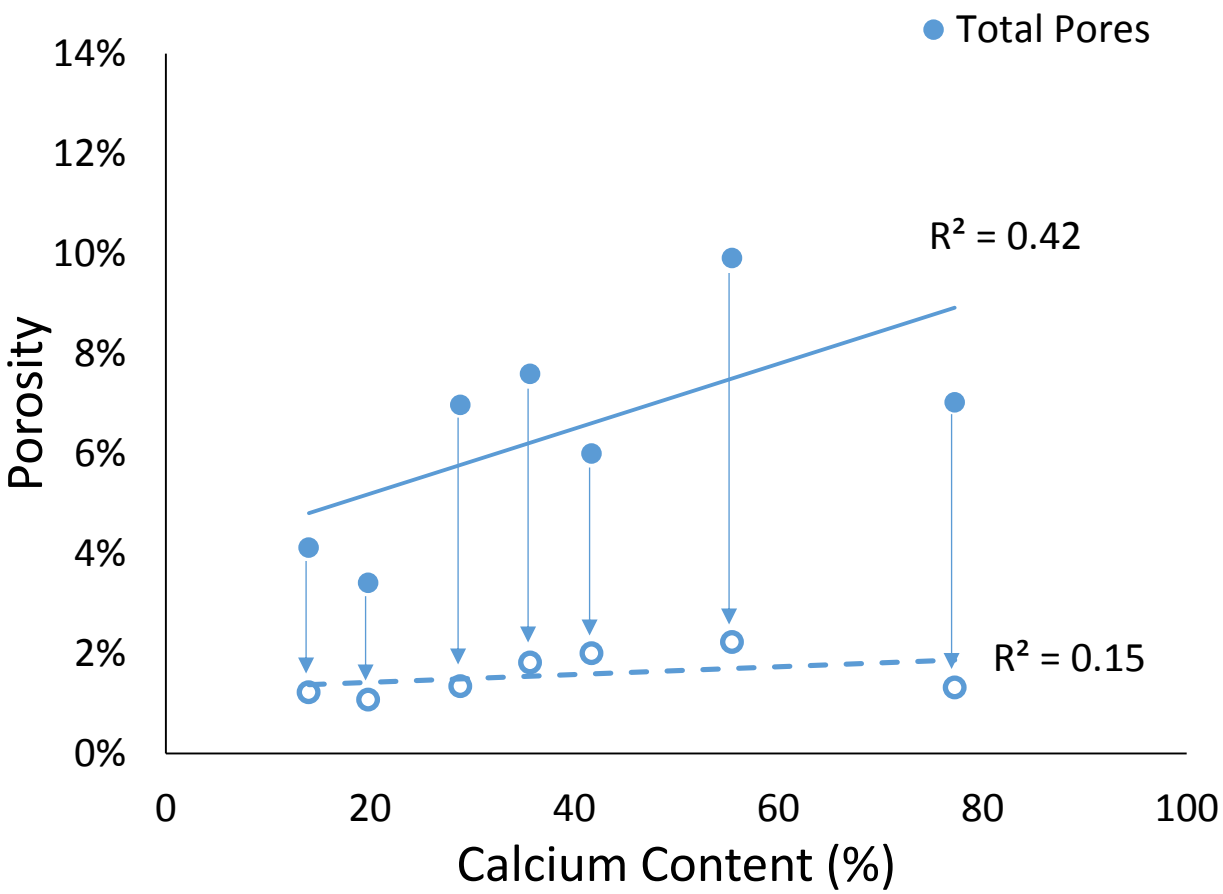

Figure 50. Pre-migration (filled symbols, solid line) and current porosity (open symbols, dashed line) for total pores (matrix plus peloid) versus calcium content (lithology). Lines through the data sets are best fit linear regressions. Arrows show the change in porosity between pre-migration and post-migration. The pre-migration total porosity trend differs slightly (in slope and correlation coefficient) from that shown in Figure 30 because of the difference in number of samples plotted (21 in Figure 27, only 7 here).

and lithology for peloid ($r = 0.52$, $R^2 = 0.27$; Fig. 48), matrix ($r = 0.17$, $R^2 = 0.03$; Fig. 49) and total pores ($r = 0.39$, $R^2 = 0.15$; Fig. 50) show that porosity with lithology trends seen in pre-migration porosity do not apply to current porosity on its own. However, porosity loss as a function of pre-migration porosity for total (matrix plus peloid), matrix, and peloid pores all show strong correlations with a greater proportion of lost porosity for the samples with the higher pre-migration porosity (Fig. 51). Total pores show a correlation coefficient of 0.65 ($R^2 = 0.42$), matrix pores have a correlation coefficient of 0.93 ($R^2 = 0.86$), and peloid pores have a correlation coefficient of 0.82 ($R^2 = 0.67$)

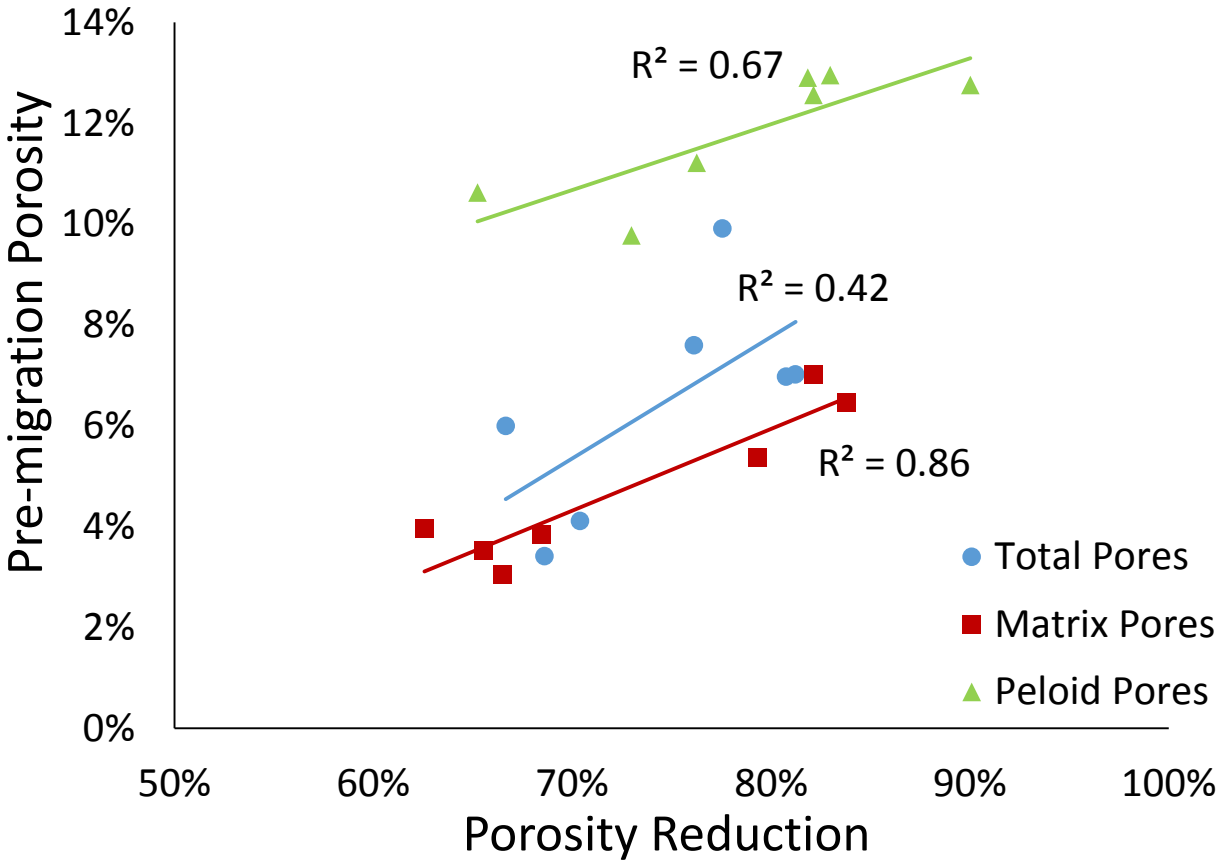

Figure 51. Pre-migration porosity versus percent reduction in porosity between pre-migration porosity and current (hydrocarbon occluded) porosity. Lines through the data sets are best fit linear regressions.

CHAPTER 6: DISCUSSION

Connectivity

The 2-D image analysis of this study cannot completely explain the 3-D interconnected nature of the observed pore systems. Nonetheless, connectivity between fabric elements (peloids and matrix) and across laminae can be inferred using pore widths, which serve as a proxy for pore-throat diameters. That is, if the minimum effective pore-throat diameter is x μm, then any 2-D pore with a width ≤ x μm is a constricting pore throat. Assuming each 2-D field of view is a representative cross section through each samples' 3-D pore network, then the loss of 2-D pores at specific width cutoffs should mimic the 3-D system. Qualitative observations in support of such an analysis can also be made using segmented images to assess the relative ease of migration between fabric elements.

The size of individual gas molecules, water, and hydrocarbon structures have been documented (Momper, 1978) and range from ~0.3 to ~0.4 nm (water and methane) up to 1000 nm for the most complex hydrocarbons. The diameters of the individual hydrocarbon molecules (i.e., paraffins to asphaltines) are below the minimum pore sizes detected in this study, thus all individual molecules would easily fit through the pore sizes discussed. However, aggregated asphaltines, kerogen particles, oil-in-water emulsions, and colloidal oil can form much larger structures with diameters between 50 nm and 1 um (Momper, 1978). If present in the Niobrara pore system, presumably due to continued catagenesis of originally smaller hydrocarbons that migrated into the pores, then those larger substances will not be able to migrate through all of the smaller pores (throats) observed.

In order to address a variety of limiting pore-throat sizes, effective minimum pore widths (throat diameters) for aggregate asphaltenes (50 nm), small kerogen particles (100 nm), oil-in-water emulsions (500 nm), and large oil colloids (1000 nm) were used to assess what percentage of the pre-migration pore system that would still be viable at those cut offs. Shown in Table 7 are the pre-migration porosities and percentages of that original pore area that remain if the minimum effective pore throat is 50 nm, 100 nm, 500 nm, and 1000 nm. Table 7 also shows the percent of individual pores in a sample that fit within those cut offs. Examples of the reduction in porosity with the progressively larger throat-size cutoffs is shown in Figure 52 for total pores (matrix plus peloid pores) in all samples. Reduction in porosity and number of effective pores are shown in Figures 53-56 for total, matrix, and peloid pores in representative chalk (Fig. 53), marly chalk (Fig. 54), marl (Fig. 55), and shaley marl (Fig. 56) samples.

The results of this analysis indicate that effective total porosity will decrease greater in shalier lithologies than chalkier lithologies. Absolute reductions in total porosity between no cut off and the 1000 nm cutoff range from approximately 11.4% to 3.8% in well-connected systems (chalks) and from approximately 5.2% to 1.2% in less favorable lithologies (marly shales). This reduction in total porosity is driven by large reductions in the number of effective pores between the 50 and 500 μm cutoffs, particularly in the matrix component of the more clay-rich samples (Figs. 53-56). High clay content associates with a larger number of small pores (e.g., Figs. 32-33), thus it is no surprise that the relatively smaller pore-size cutoffs result in a large decrease in the number of effective pores in the clay-rich samples.

Peloid-to-peloid fluid migration is likely the smoothest path for hydrocarbon movement, especially for the larger hydrocarbon complexes. Both the DJ and Piceance samples show an

Table 7. List of 21 high-graded samples, their percentage of porosity and percentage of individual pores remaining with increasingly larger effective pore throat (width) cutoffs total (matrix plus peloid) median pre-migration and current equivalent circular diameters (ECD), widths, and anisotropies. Data presented for total pores (matrix plus peloid), peloid pores, and matrix pores. C = Chalk MC = Marly Chalk M = Marl MS = Marly Shale * No discernable peloids in sample

			Effective minimum pore width = 50 nm (Asphaltene Aggregates)						Effective minimum pore width = 100 nm (Smallest Kerogen Particles)						Effective minimum pore width = 500 nm (Smallest oil/water emulsions)						Effective minimum pore width = 1000 nm (Largest colloidal oils)					
			Total Pore System		Peloid Pores		Matrix Pores		Total Pore System		Peloid Pores		Matrix Pores		Total Pore System		Peloid Pores		Matrix Pores		Total Pore System		Peloid Pores		Matrix Pores	
Well	Depth	Lithology	% of Pre-Migration Pores	Porosity	% of Pre-Migration Pores	Porosity	% of Pre-Migration Pores	Porosity	% of Pre-Migration Pores	Porosity	% of Pre-Migration Pores	Porosity	% of Pre-Migration Pores	Porosity	% of Pre-Migration Pores	Porosity	% of Pre-Migration Pores	Porosity	% of Pre-Migration Pores	Porosity	% of Pre-Migration Pores	Porosity	% of Pre-Migration Pores	Porosity	% of Pre-Migration Pores	Porosity
Timbro	5666	MC	100%	7.0%	100.0%	9.8%	100.0%	6.5%	28.1%	6.2%	42.7%	9.3%	26.2%	5.5%	1.8%	3.2%	4.9%	6.0%	1.5%	2.6%	0.3%	1.7%	1.2%	3.4%	0.2%	1.4%
Timbro	5680.7	MC	100%	8.1%	100.0%	11.5%	100.0%	7.3%	72.8%	8.0%	78.5%	11.4%	71.5%	7.2%	14.0%	5.5%	21.8%	8.8%	12.3%	4.7%	3.1%	2.6%	5.6%	4.6%	2.6%	2.2%
Timbro	5703.3	C	100%	11.2%	100.0%	12.2%	100.0%	11.2%	74.3%	10.3%	77.0%	10.9%	72.0%	10.0%	15.1%	7.2%	20.0%	9.2%	15.0%	8.3%	3.0%	3.7%	4.0%	5.7%	3.1%	2.3%
Timbro	5724.2	C	100%	11.7%	100.0%	10.3%	100.0%	11.9%	78.0%	11.6%	79.3%	10.3%	77.8%	11.8%	15.8%	8.0%	13.1%	6.1%	16.1%	8.2%	3.6%	3.9%	2.0%	2.3%	3.8%	3.9%
Timbro	5758	M	100%	6.3%	100.0%	9.9%	100.0%	6.2%	41.9%	5.6%	48.1%	9.1%	41.7%	5.4%	2.0%	1.9%	3.4%	3.7%	2.0%	1.8%	0.3%	0.7%	0.5%	1.4%	0.3%	0.7%
Timbro	5799.5	MC	100%	10.3%	100.0%	8.9%	100.0%	10.6%	36.8%	9.1%	36.2%	7.7%	36.9%	9.4%	2.3%	3.9%	1.9%	2.9%	2.3%	4.1%	0.4%	1.7%	0.3%	1.1%	0.4%	1.8%
Timbro	5813.6	M	100%	9.9%	100.0%	11.2%	100.0%	7.0%	43.8%	9.5%	50.1%	10.8%	29.9%	6.5%	6.0%	6.4%	7.9%	7.2%	1.9%	4.7%	1.5%	3.9%	2.0%	3.9%	0.4%	3.9%
Timbro	5823.4	MC	100%	8.2%	100.0%	11.0%	100.0%	7.6%	63.5%	8.1%	68.6%	10.9%	62.5%	7.6%	11.4%	5.4%	13.8%	7.7%	10.9%	5.0%	2.3%	2.7%	12.1%	4.1%	2.8%	2.4%
Timbro	5835.7	M	100%	8.0%	100.0%	12.7%	100.0%	6.6%	34.1%	7.4%	41.1%	12.2%	32.3%	6.0%	3.4%	4.8%	6.2%	9.2%	2.7%	3.6%	0.9%	3.2%	1.9%	6.3%	0.7%	2.3%
Timbro	5902	MC	100%	8.5%	*	*	100%	8.5%	67.8%	8.3%	*	*	67.8%	8.3%	8.6%	5.5%	*	*	8.6%	5.5%	2.3%	3.7%	*	*	2.3%	3.7%
#5	7638	M	100%	7.7%	100.0%	11.3%	100.0%	6.2%	63.6%	7.5%	72.7%	11.2%	58.7%	6.1%	7.5%	4.2%	10.9%	6.6%	5.7%	3.2%	1.3%	1.7%	1.9%	2.6%	0.9%	1.4%
#5	7645	M	100%	5.1%	100.0%	8.9%	100.0%	4.7%	76.0%	5.1%	77.9%	8.8%	75.6%	4.7%	9.0%	2.8%	10.5%	4.6%	8.7%	2.6%	1.5%	1.2%	1.6%	1.5%	1.5%	1.1%
#5	7750	MS	100%	4.9%	100.0%	7.6%	100.0%	4.7%	25.4%	3.9%	32.5%	6.6%	25.1%	3.7%	0.9%	1.0%	1.8%	2.6%	0.9%	0.9%	0.1%	0.3%	0.2%	0.9%	0.1%	0.2%
#5	8000	M	100%	7.8%	100.0%	12.0%	100.0%	7.1%	31.4%	6.9%	50.3%	11.4%	28.8%	6.2%	2.2%	3.6%	4.7%	6.0%	1.8%	3.2%	0.5%	2.1%	0.9%	2.8%	0.4%	2.0%
#5	8382	MS	100%	7.0%	100.0%	12.9%	100.0%	5.4%	41.3%	6.5%	61.2%	12.7%	37.3%	4.8%	2.9%	3.6%	8.4%	8.7%	1.8%	2.2%	0.7%	2.1%	2.1%	5.4%	0.4%	1.2%
#5	8390	MS	100%	4.9%	100.0%	12.3%	100.0%	3.7%	58.1%	4.8%	75.2%	12.3%	55.1%	3.7%	7.4%	3.1%	19.8%	9.8%	5.3%	2.0%	7.4%	1.7%	19.8%	6.1%	1.0%	1.0%
#4	10010.7	MS	100%	3.4%	100.0%	12.9%	100.0%	3.0%	22.2%	2.7%	46.0%	12.2%	21.1%	2.3%	0.9%	0.9%	5.2%	7.4%	0.7%	0.6%	0.1%	0.3%	1.1%	3.8%	0.1%	0.2%
#4	10045.1	M	100%	6.0%	100.0%	10.6%	100.0%	3.8%	36.8%	5.4%	56.6%	10.2%	28.4%	3.2%	2.9%	2.6%	6.7%	6.0%	1.2%	1.1%	0.5%	1.2%	1.3%	2.9%	0.2%	0.4%
#4	10142.8	MS	100%	4.1%	100.0%	12.8%	100.0%	3.5%	28.6%	3.5%	52.7%	12.3%	26.7%	2.9%	1.7%	1.7%	7.3%	8.0%	1.3%	1.2%	0.3%	0.8%	1.8%	4.4%	0.2%	0.6%
#4	10251.9	M	100%	7.6%	100.0%	12.6%	100.0%	3.9%	38.1%	7.1%	51.6%	22.0%	28.1%	15.6%	3.8%	4.4%	6.9%	8.3%	1.5%	1.5%	0.9%	2.5%	1.8%	5.0%	0.3%	0.8%
#4	10380.3	MS	100%	6.9%	100.0%	12.3%	100.0%	5.0%	25.1%	6.7%	59.9%	12.2%	19.6%	4.8%	3.4%	4.2%	12.6%	8.8%	2.0%	2.6%	0.7%	1.9%	3.0%	4.5%	0.3%	1.0%

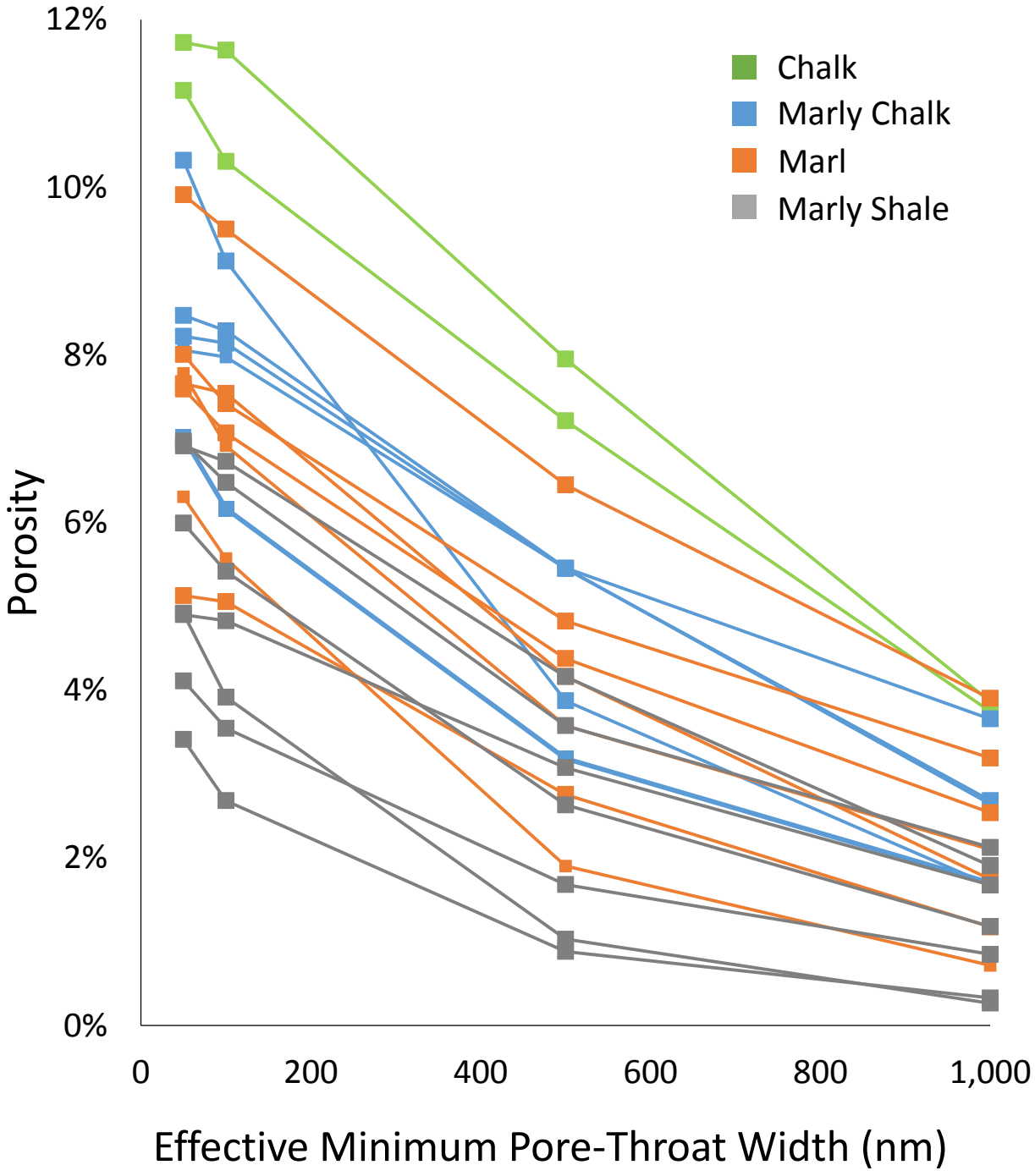

Figure 52. Effective porosity at various minimum effective pore widths for total pore system (matrix plus peloid pores) for each sample coded by lithology. Pore sizes cutoffs reflect common hydrocarbon molecule aggregates (50 nm for asphaltene aggregates 100 nm for small kerogen particles, 500 nm for small oil/water emulsions, and 1000 nm for large oil colloids.

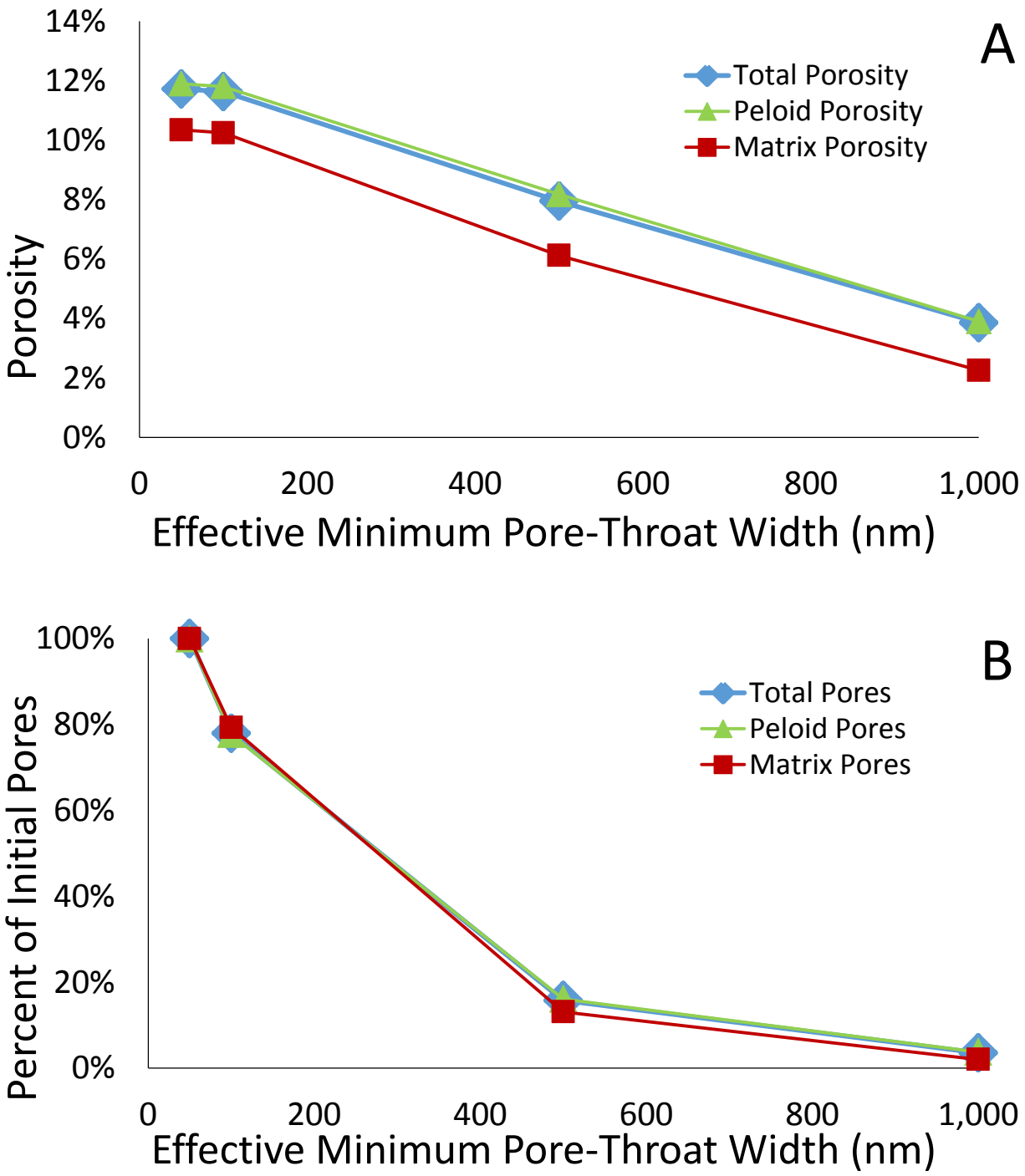

Figure 53. Effective porosity (A) and percent of effective initial pores (B) at various minimum effective pore widths for matrix, peloid, and total (matrix plus peloid) pores for a representative chalk (Timbro, 5724). Pore sizes cutoffs reflect common hydrocarbon molecule aggregates (50 nm for asphaltene aggregates, 100 nm for small kerogen particles, 500 nm for small oil/water emulsions, and 1000 nm for large oil colloids.

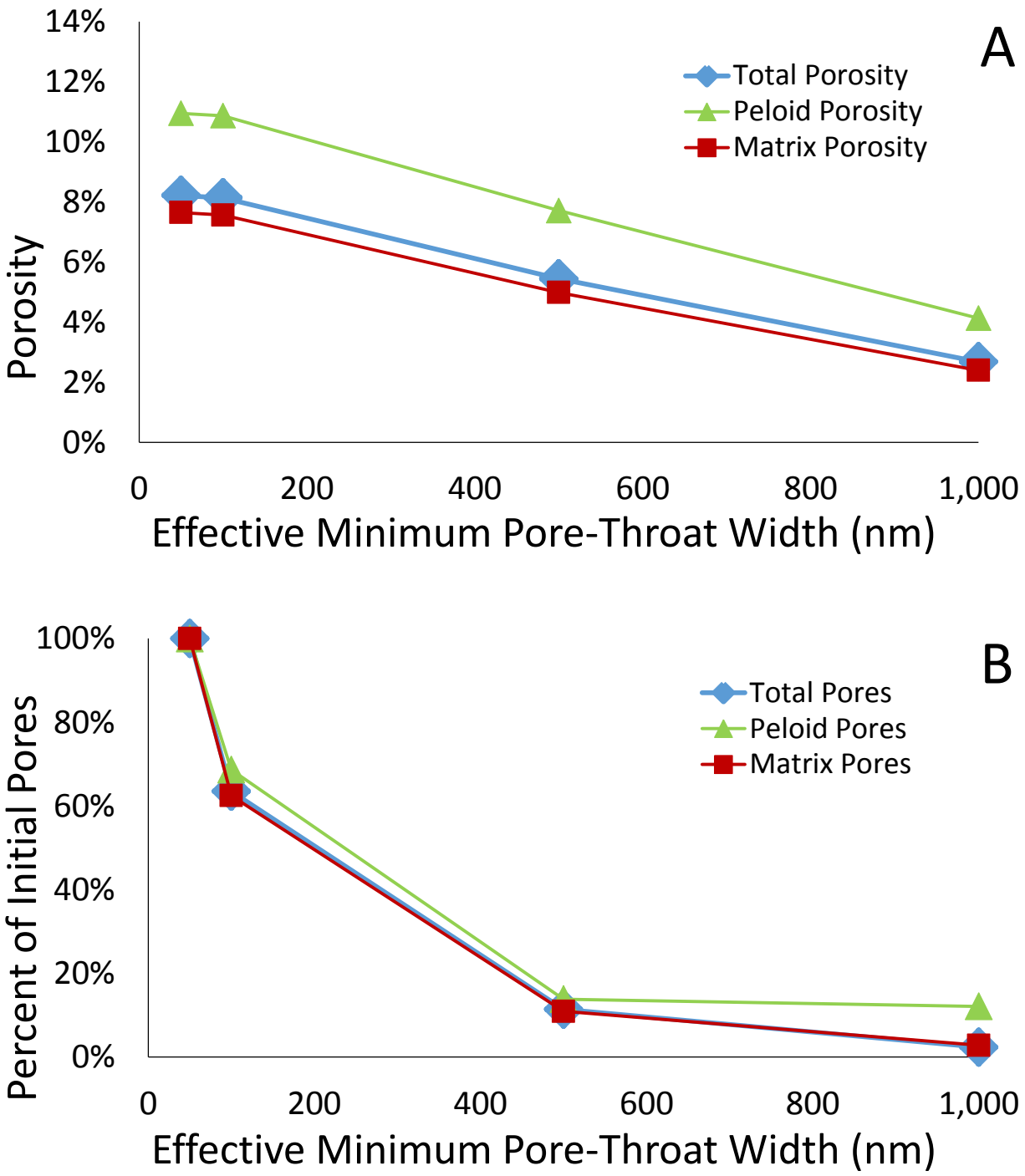

Figure 54. Effective porosity (A) and percent of effective initial pores (B) at various minimum effective pore widths for matrix, peloid, and total (matrix plus peloid) pores for a representative marly chalk (Timbro, 5823). Pore sizes cutoffs reflect common hydrocarbon molecule aggregates (50 nm for asphaltene aggregates, 100 nm for small kerogen particles, 500 nm for small oil/water emulsions, and 1000 nm for large oil colloids.

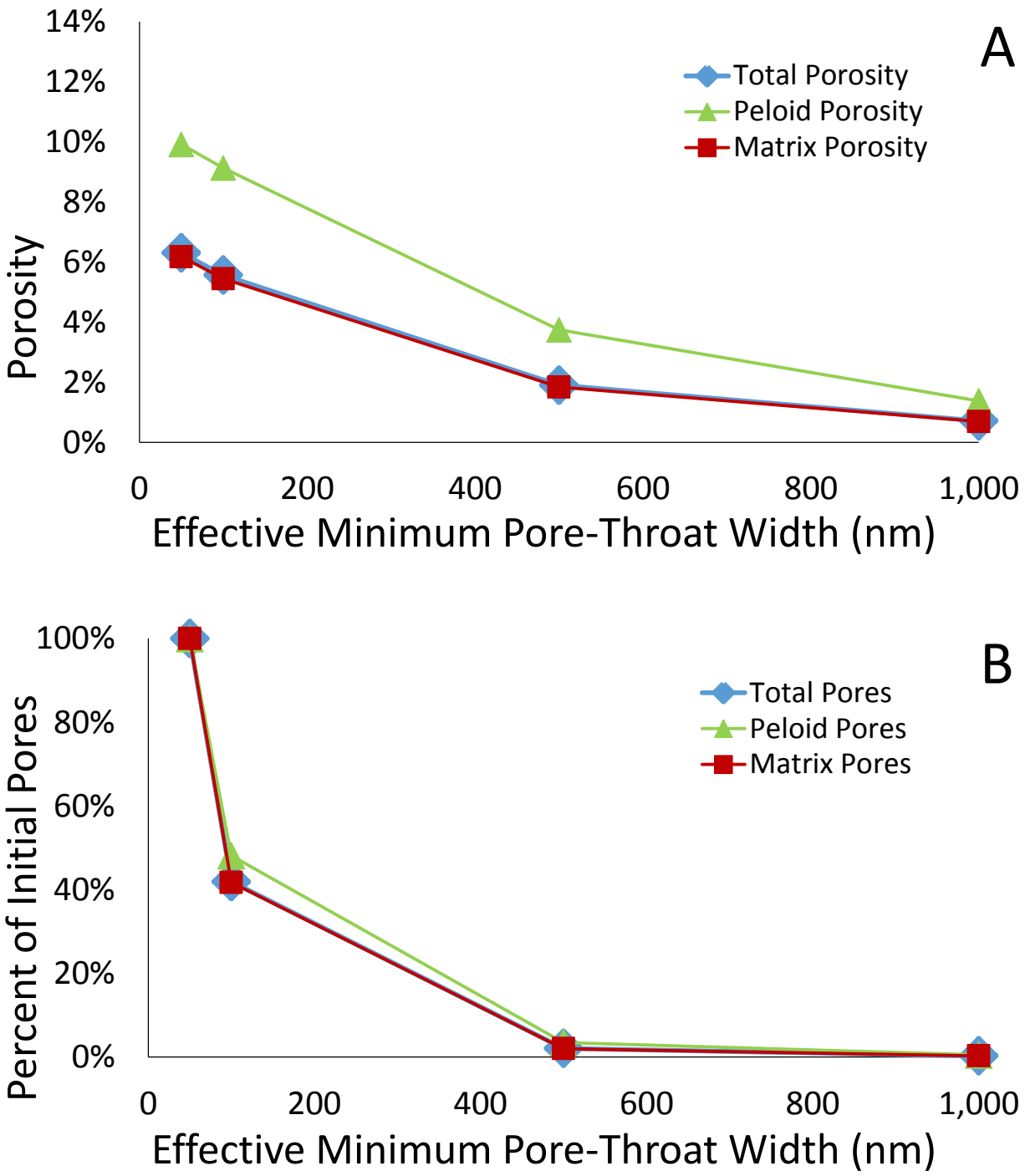

Figure 55. Effective porosity (A) and percent of effective initial pores (B) at various minimum effective pore widths for matrix, peloid, and total (matrix plus peloid) pores for a representative marl (Timbro, 5758). Pore sizes cutoffs reflect common hydrocarbon molecule aggregates (50 nm for asphaltene aggregates, 100 nm for small kerogen particles, 500 nm for small oil/water emulsions, and 1000 nm for large oil colloids.

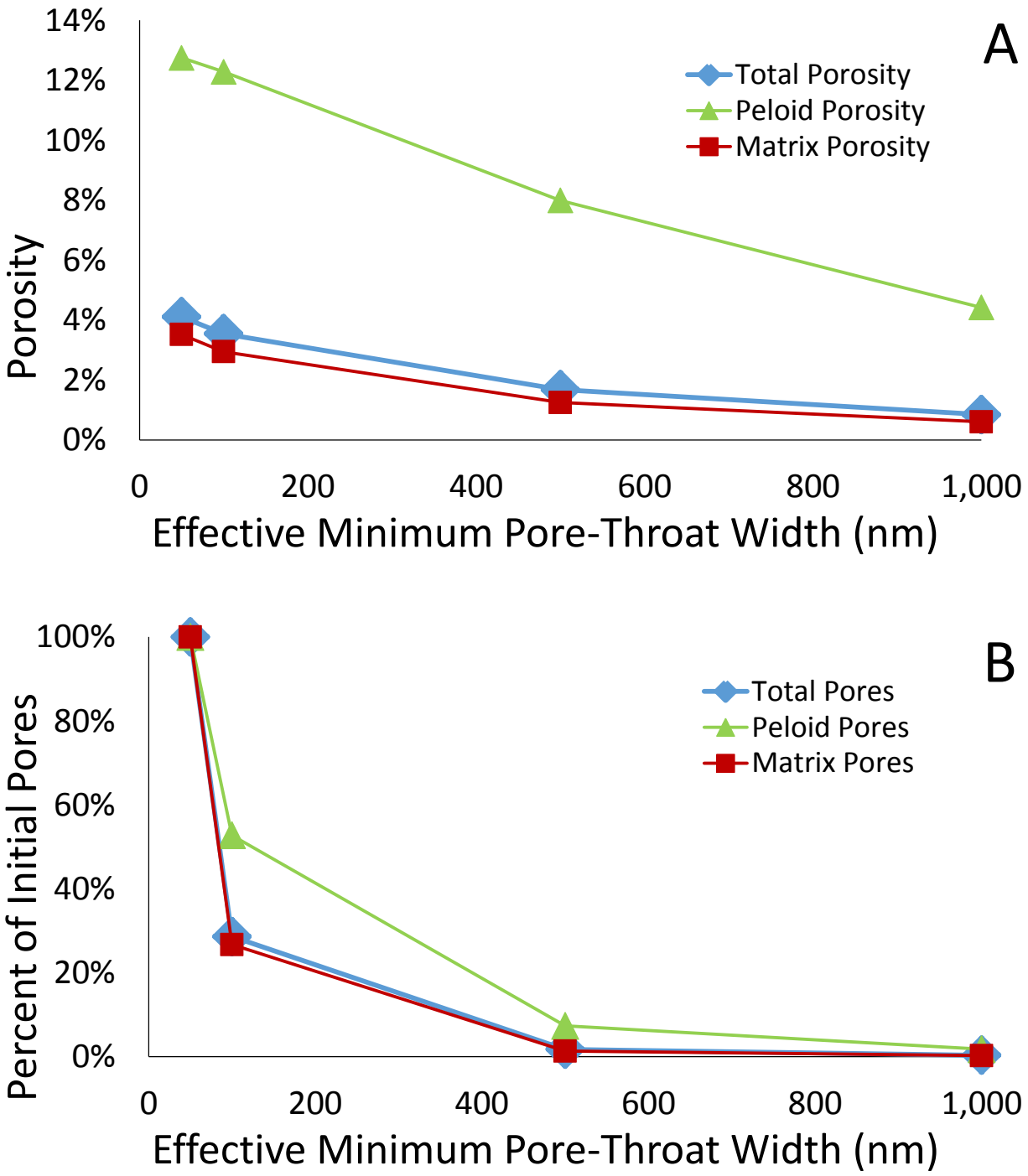

Figure 56. Effective porosity (A) and percent of effective initial pores (B) at various minimum effective pore widths for matrix, peloid, and total (matrix plus peloid) pores for a representative marly shale (well #4, 10142). Pore sizes cutoffs reflect common hydrocarbon molecule aggregates (50 nm for asphaltene aggregates, 100 nm for small kerogen particles, 500 nm for small oil/water emulsions, and 1000 nm for large oil colloids.

average effective peloid porosity for 1000 nm complexes of 3.6%. However, peloids in marly chalk and shalier samples are often isolated in our 2-D imagery and may not connect at all except in peloid-rich laminae. Where peloids are not in contact, migration through the matrix will be necessary. The efficiency of this migration will vary greatly with lithology as the median matrix pore width and matrix porosity drop significantly in marly shale samples compared to pure chalks and marly chalks. Chalk matrix porosity drops from 11.6% to 3.1% while marly shale matrix porosity drops from an average of 4.2% to 0.7% (Table 7) when comparing 50 nm pores and 1000 nm pores. A visual representation of the loss of effective porosity with increasing pore throat cutoffs, especially in the matrix between peloids, is seen for a marl sample in Figure 57. Whereas effective pores remain in the matrix at 50 and 100 nm (Fig. 57C, D), their numbers decrease and become increasingly more isolated at the 500 nm (Fig. 57E) and 1000 nm cutoffs (Fig. 57F). Pores still remain in the peloids, but those pores also become more isolated at the higher cutoffs.

One avenue for migration not thoroughly explored in this study that is likely responsible for much of the pre-hydraulically fractured hydrocarbon mobility is natural fractures. In the 21 large tiled mosaics collected for this study, 19 displayed fractures that cut across the entire FOV which ranged in width from roughly 0.5 to 1.0 µm. Of these 19, 15 of the samples' fractures were partially or completely filled with residual hydrocarbon like those shown in (Fig. 58), suggesting these fractures are not artifacts of the coring process but rather existed when initial hydrocarbon migration occurred.

Sedimentologic Influences on Pore Systems

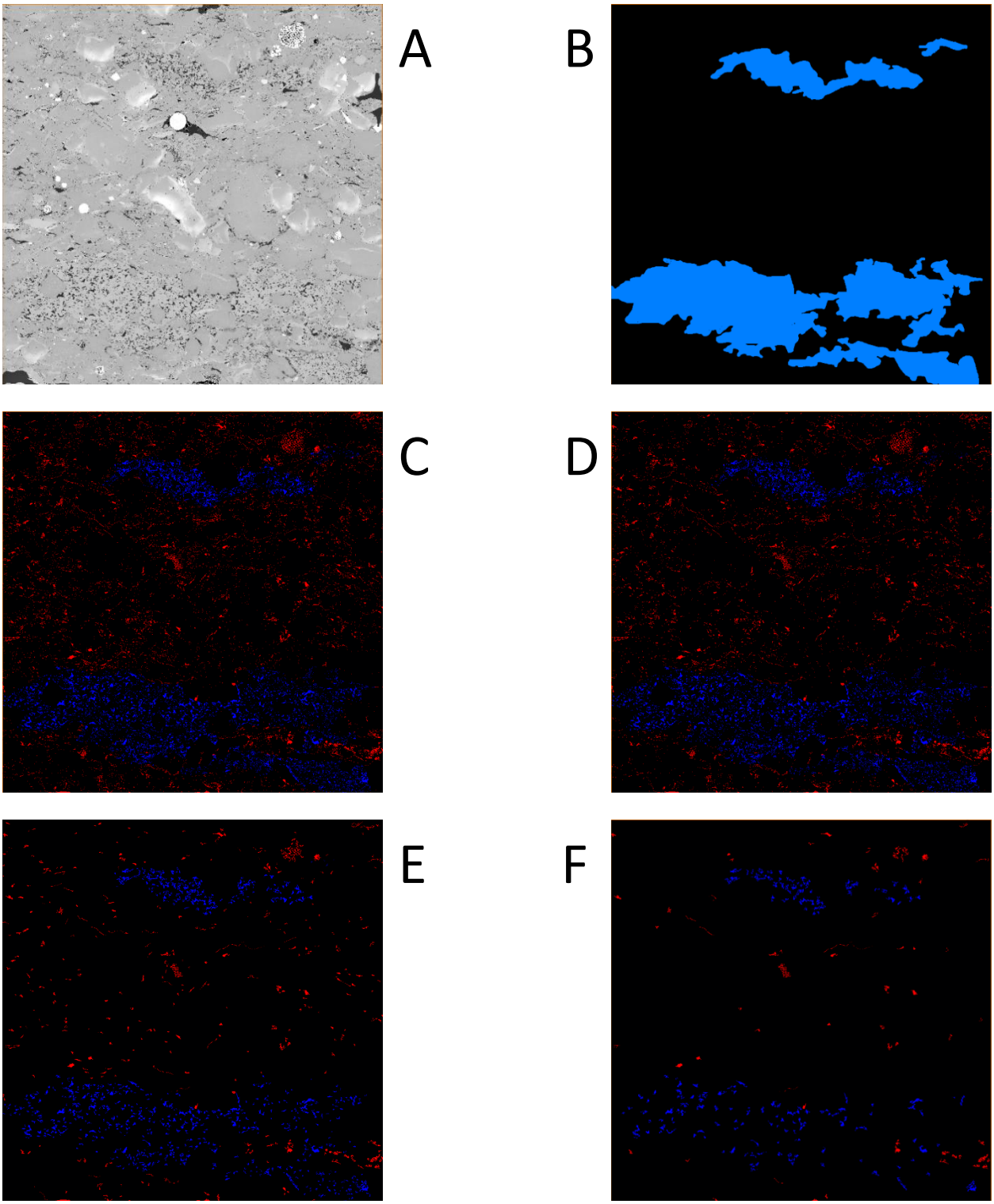

Figure 57. A) Backscattered SEM image of a representative marl sample (well #4, 10251). The field of view is 150 µm x 150 µm FOV and it shows a typical distribution of pores, minerals, and organic matter. Image B shows the same field of view with peloids segmented in blue. Images C through F are the same field of view showing effective pores in peloids (blue) and matrix (red) at various effective minimum pore widths. Minimum width cutoffs are 50 nm (C), 100 nm (D), 500 nm (E), and 1000 nm (F).

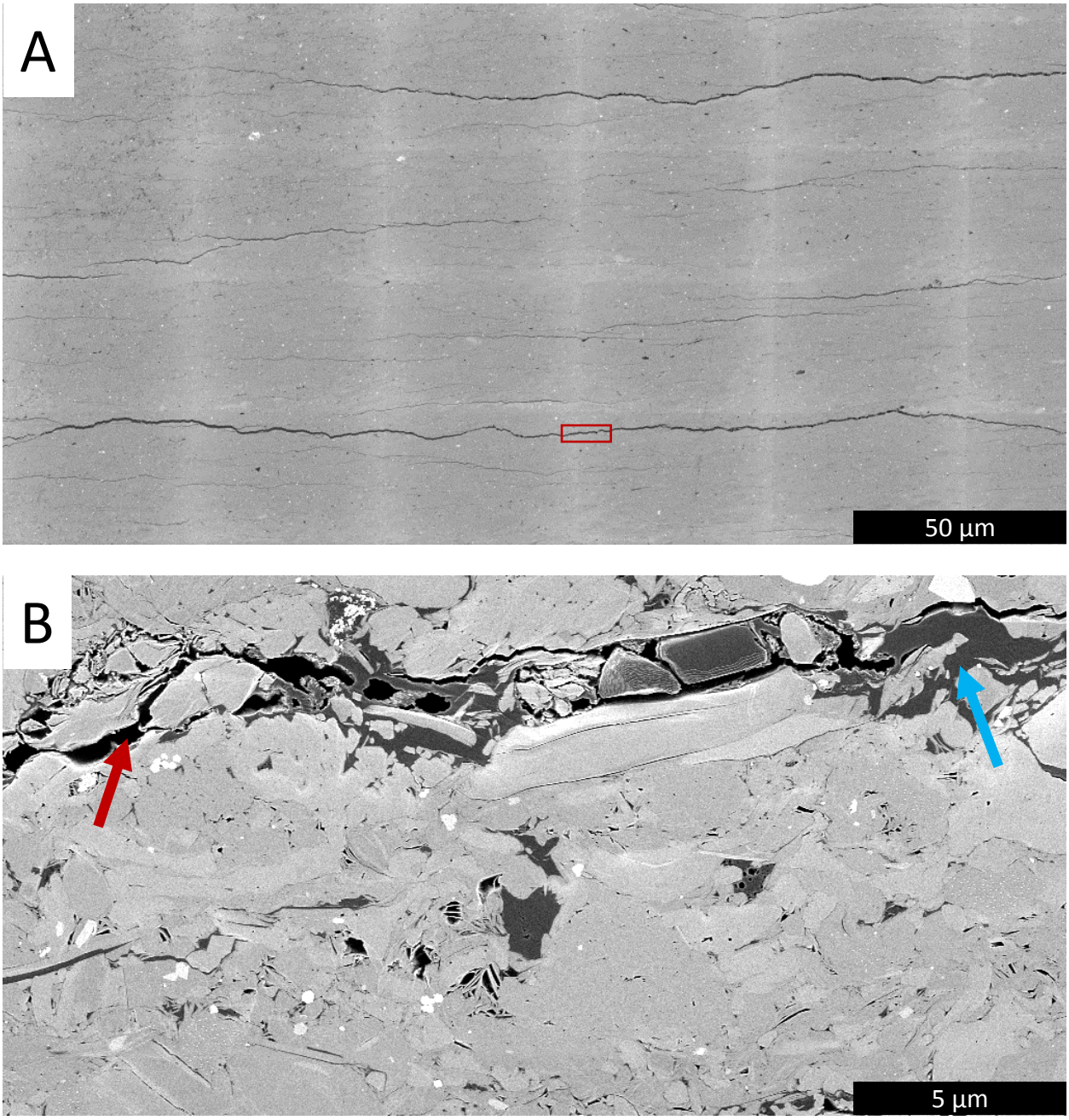

Figure 58. An example of fractures cross-cutting a large backscattered SEM image mosaic, ~~o~~f sample well #4, 10010 (A) and a higher magnification view of the partial hydrocarbon fill within the fracture (B). The red rectangle in A shows the approximate field of view shown in image B. The blue arrow points to hydrocarbon fill within the fracture and the red arrow points to remaining open porosity.

Petrographic observations made during microfacies characterization indicate the presence of a variety of sedimentary structures that likely have a significant impact on the millimeter to centimeter scale variability in pore systems and connectivity. Ripple laminations (Fig. 59A), graded bedding (Fig. 59B), burrows (Fig. 59C), and cryptic bioturbation (Fig. 59D) all play a role in the concentration and distribution of peloids, silt, and clay. These differing concentrations serve to separate both larger, presumably more connected and smaller, less well connected pore types into potentially isolated or homogenized zones. These zones can be seen in core as well as in thin sections or elemental microprobe maps ranging in scale from millimeters to decimeters. Greater research on the bed-scale distributions of lithologic components and how the nano-scale observations made in this study, Michaels (2014), and Burt (2014) are needed to fully understand the impact these features have on the overall pore system.

Pore systems may also be influenced, to lesser extents, by the presence, concentrations, and diagenetic states of siliciclastic silt and foraminifera shells. In some imaged fields of view, silt grains seem suitably concentrated to provide a grain-supported framework that inhibited compaction in localized areas, thus propping open pores partially filled with ductile clay (Fig. 60A). This may be an example of the pressure shadow effect discussed in Lash and Blood (2004) and Scheiber (2010). In other fields of view, silt concentrations do not exhibit this behavior and as the space between quartz silt grains themselves contain no appreciable porosity, these silt-grain concentrations act to completely block porosity (Fig. 60B). This may be influenced by the original nature of the uncompacted sediment. If the sediment was originally grain supported, it may undergo less compaction and therefore clay-related pores between grains is maintained. If

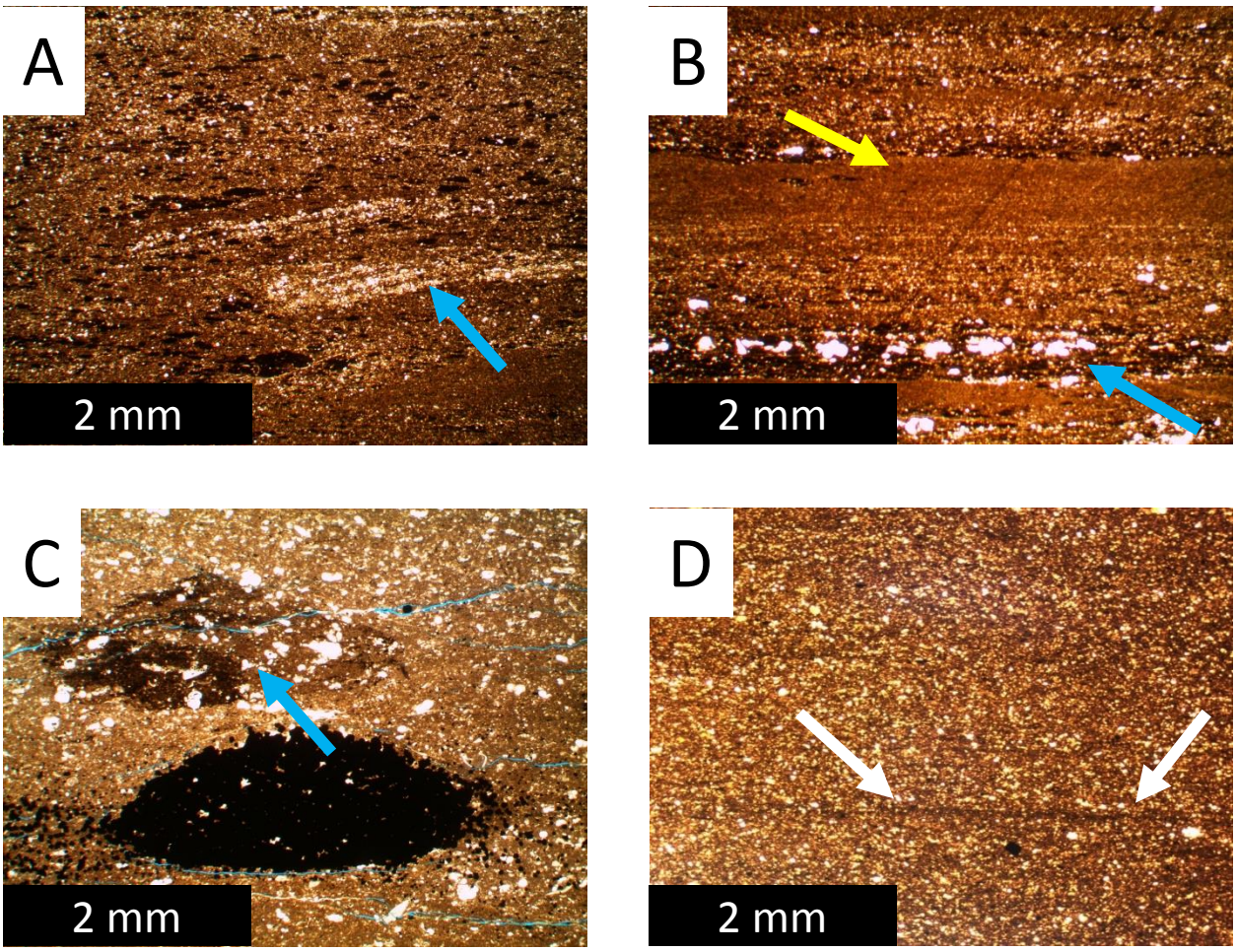

Figure 59. Thin-section photomicrographs with arrows pointing to examples of ripple laminations (A; #4, 10010), graded beds grading from clay material at the top (yellow arrow) to forams and peloids at the base (blue arrow) (B; #4, 8390), burrows (C; #5, 10251), and cryptic bioturbation (D; Timbro, 5835). The cryptic burrows are small – 10s of microns in size – and individual burrows are not visible. Their presence though is suggested by the faintness and disruption of physical laminations (white arrows).

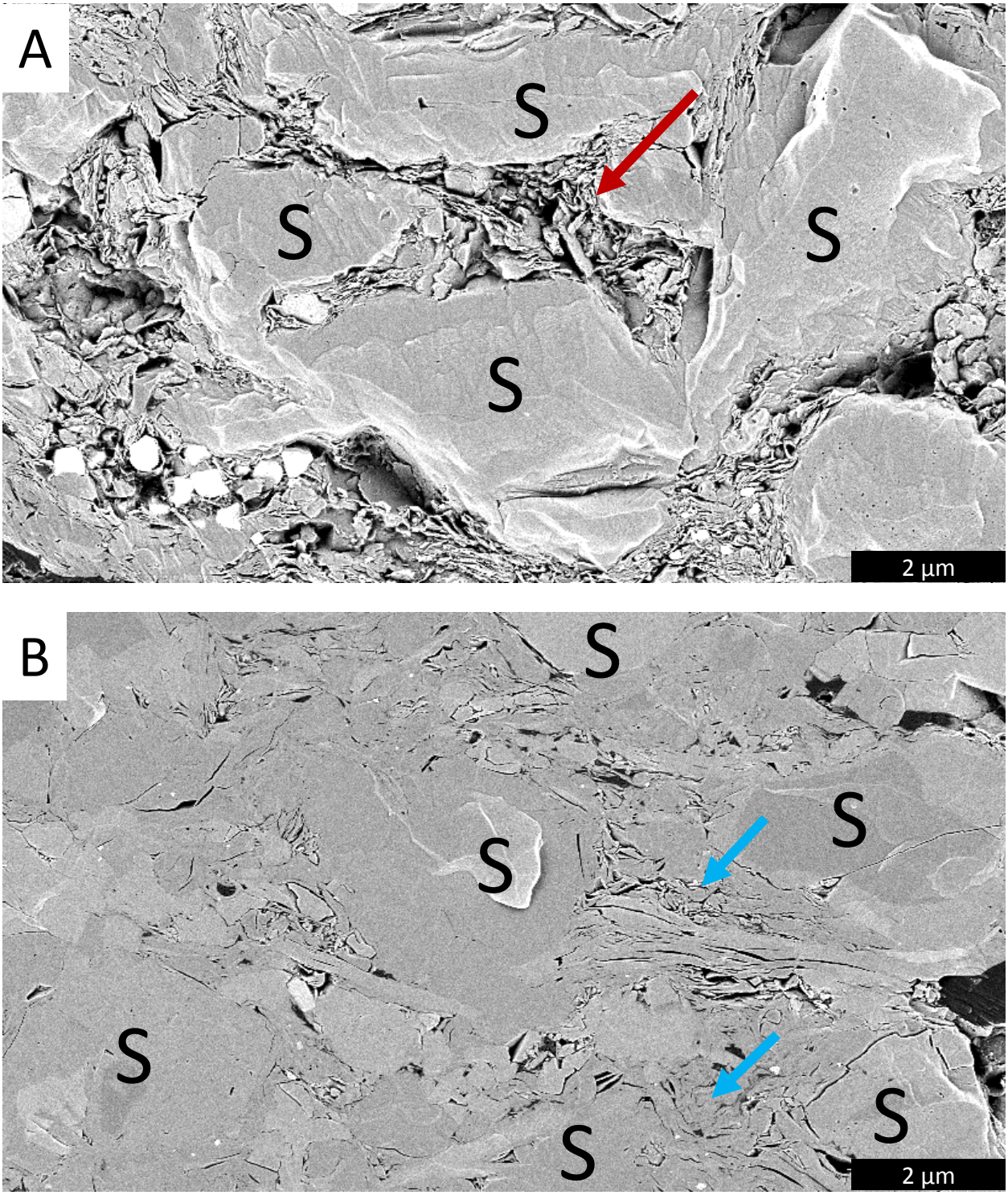

Figure 60. Backscattered SEM images of open (A; well #5, 7750) and compacted (B; well #5, 8382) clay porosity in between silt grains. Image A shows a silt-supported matrix wherein silt grains (S) provide a framework that shelters the clay floccule between them and kept open the pores within floccule (red arrow). Image B shows an instance of silt grains (S) and adjacent clay flocules that compacted together, resulting in the collapse and closure of the porosity originally in the floccule (blue arrow).

the sediment was originally matrix supported, it may compact and displace more ductile material into original pores, creating a much less porous rock.

Micron to 10s of micron-sized skeletal material derived from the disaggregation of coccolithophores make up most of the primary calcareous material in these samples and the dominant intercrystaline pores system associated with calcite is associated with this coccolithophore debris, be it in peloids or matrices. However, foraminifera tests are also present in varying abundances in many samples, particularly marly chalks and chalks as seen in the elemental microprobe maps. These foram tests do vary in their degree of diagenetic overprint. Individual tests can range from almost completely open to completely infilled with calcite cement (Fig. 22), dolomite cement (Fig. 61A), or in some instances clay cement (Michaels, 2014). In the latter case, there can be clay-related porosity associated with the clay cements (Fig. 61B).

Diagenetic Impacts on Pore Systems

After the biogenic and detrital material reach the seafloor three main factors influence the development of the pore systems: physical compaction, pressure solution, and maturation of organic material (Lockridge and Scholle, 1978; Hattin, 1981; Loucks et al., 2009, 2010, 2012; Heath et al., 2011; Slatt and O'Brien, 2011; Sonnenberg, 2011; Chalmers et al., 2012; Curtis et al., 2010, 2012; Fishman et al., 2012; May, 2013; Cumella et al., 2014; Lu et al., 2015). SEM photomicrographs from the Niobrara Formation in Kansas taken by Lockridge and Scholle (1978) and Hatttin (1981) provide a direct comparison to the western and eastern Colorado chalky Niobrara samples of this study (Fig. 6). These images, from rocks with maximum burial

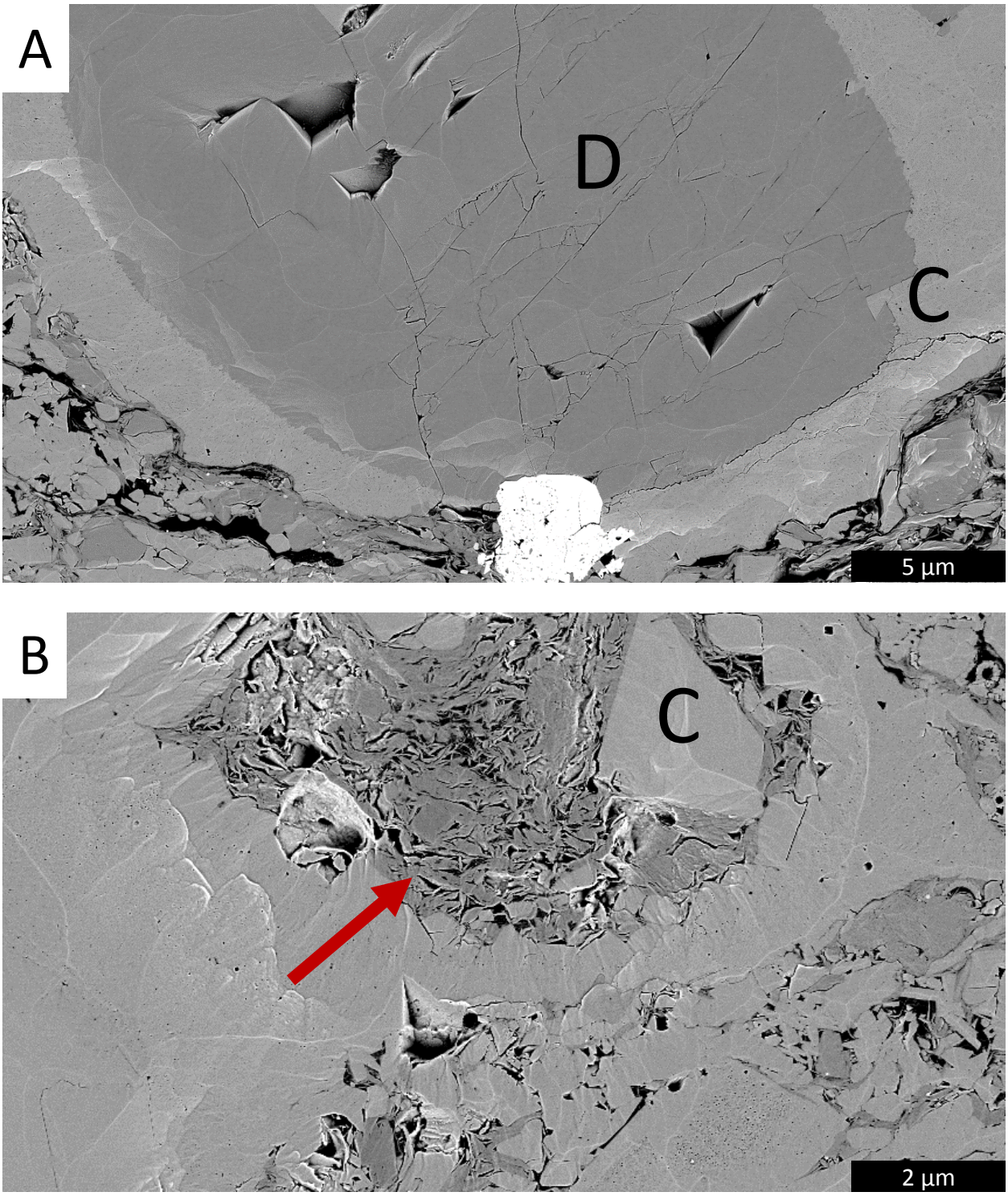

Figure 61. Backscattered SEM images of two foraminifera shells in the same sample (Timbro, 5758) but displaying two different cement infillings. Image A shows almost complete infill by dolomite (D) and calcite (C). Image B shows infill by calcite (C) and authigenic clay (red arrow).

depths < 2000 ft, show little evidence for physical compaction or cementation. In contrast, the Piceance and DJ samples exhibit more physical compaction and breakage (Fig. 6), evidenced by the greater presence of smaller, more collapsed shell fragments. The DJ and Piceance samples also exhibit a greater presence of calcite cement overgrown onto coccolithophore debris, with that authigenic calcite presumably derived from pressure solution (Murray, 1960). The abundance of rhombic terminations of calcite and generally horizontal alignment of both calcite (46.5% of all pores within 30° of horizontal) and siliciclastic-bounded pores (55.6% of shaley marl matrix pores) show the significance of both the physical and chemical changes burial has on these pore systems. In addition, in both basins, more ductile materials like organic material and clay minerals are observed bending around more physically stable minerals and filling what was probably original void space (Fig. 62).

The influences of compaction and burial diagenesis seen in mudstones (Loucks et al., 2009, 2010, 2012; Heath et al., 2011; Chalmers et al., 2012; Fishman et al., 2012) are also present in the samples used for this study. In particular, the images from the Piceance Basin samples show compaction of clay floccules (Fig. 60B), cleavage-sheet pores (Fig. 63A) similar to those described in Loucks et al. (2012), and overgrowths of secondary minerals (calcite or another mineral) on detrital siliciclastic minerals (Fig. 63B).

Upscaling

Upscaling nano- to micro-scale pore system observations to well or reservoir-scale questions and models is one of the most challenging problems in unconventional reservoirs like the Niobrara Interval. For the Niobrara Interval specifically, the multiple scales of heterogeneity

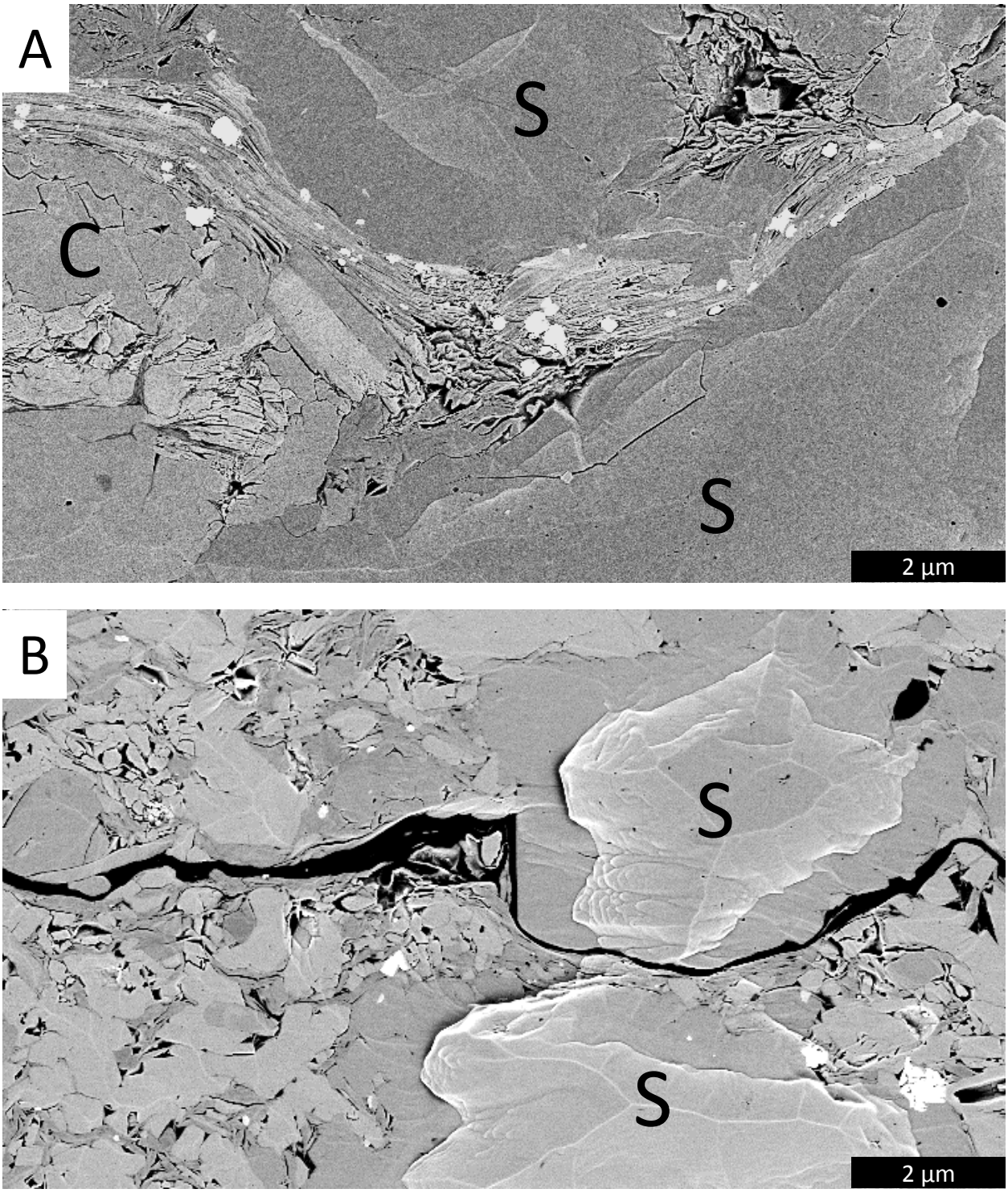

Figure 62. Backscattered SEM images of ductile materials being bent around more solid materials as a result of mechanical compaction in both the Piceance (A; well #5, 8000) and DJ (Timbro, 5758) basins. Image A shows a mineral grain (likely a mica) bent between two siliciclastic silt grains (S) and a mass of calcite (C). Photo B shows a string of detrital organic material compressed and bent between two silt grains (S).

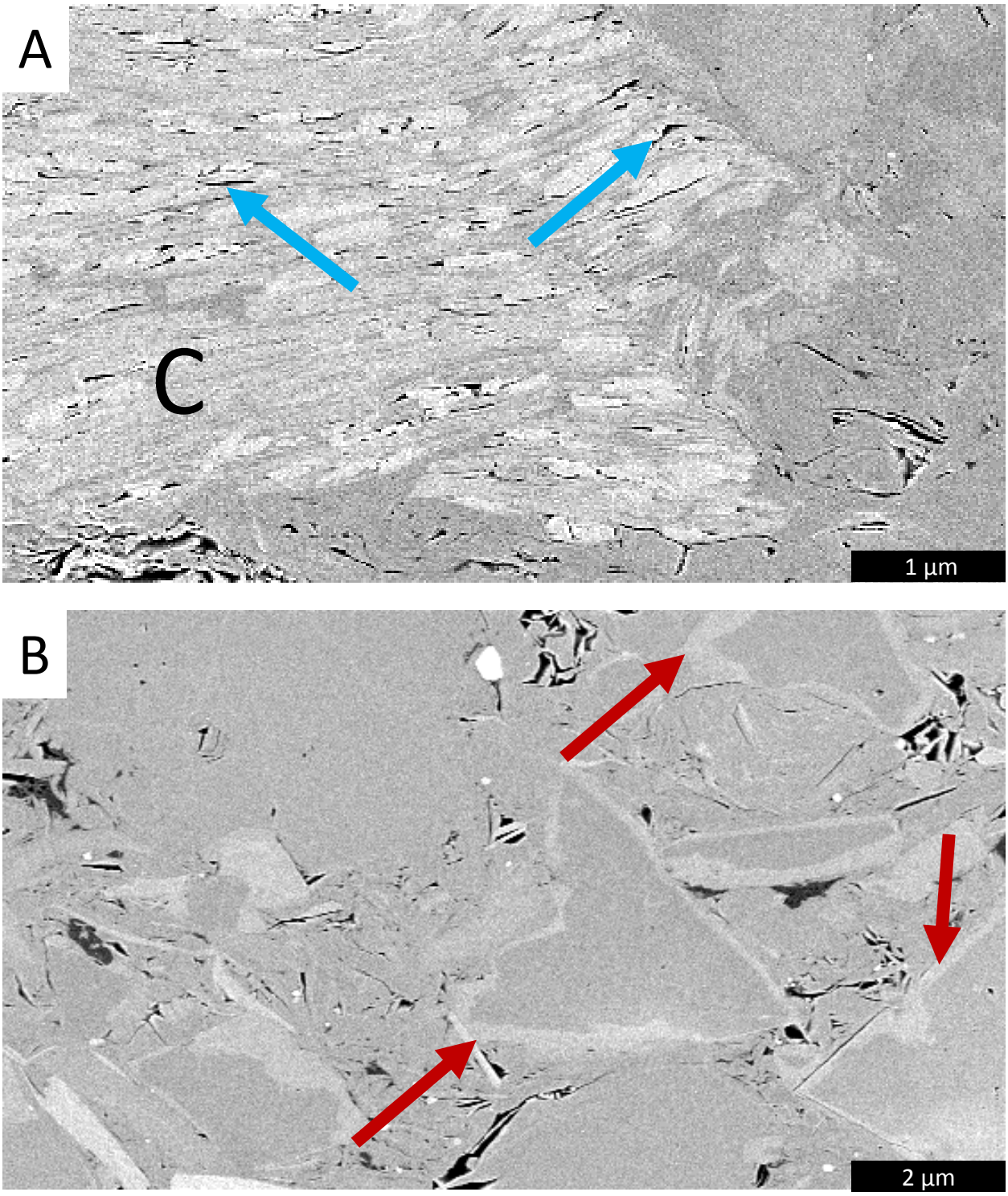

Figure 63. A) Backscattered SEM images of cleavage-sheet pores (blue arrows) in clay (C) in well #5, 8000. B) Cementation by secondary mineral (red arrows) on detrital siliciclastic material in well #4, 10251.

discussed by Michaels (2014) and Burt (2014) represent a significant challenge. Lithologic heterogeneity occurs over at least 10 orders of magnitude. It varies from nanometer-scale pore size and shape, to micrometer-scale variability in the distribution of fabric elements (i.e., peloid packing), to millimeter-scale laminations, to decimeter and centimeter-scale bedsets, to meter-scale lithofacies zones, to decameter-scale stratigraphic zonations (Fig. 64). To characterize that heterogeneity we can use comparisons of pore images, elemental data from core analysis, lithofacies observations in core, and petrophysical observations. These tools are really comparisons of averages made at microns or nanometers (image data), to a few cm^2 (XRF data), to 100s of cm^2 (core facies), to 1000s cm^2 (well-log measurements). Given that the pore systems vary on a scale much smaller than is capable of observation by conventional tools, the proxies of calcium content, peloid abundance, natural fracture density, and thermal maturity used together will probably provide the best insight into upscaling the nanopore systems of the Niobrara Interval. Neutron density well log tools can capture estimates of calcium distribution and should thus be used in both basins.

Peloid abundance can be a large factor in the connectivity and storage systems, but can change on a sub-millimeter scale and cannot easily be mapped at any scale applicable to hydrocarbon explorationists. Core analysis is the most efficient technique to identify areas of peloid concentration. Pairing core observations with well log-derived mineralogical measurements can help identify areas of both large peloid abundance and potentially high-calcite matrix zones. There will still be uncertainty as to the distribution of individual calcite-rich laminae and their interlayered nature with calcite-poor laminae (as seen in the elemental maps; Fig. 17), but these methods provide a good first step to optimizing the stratigraphic occurrence

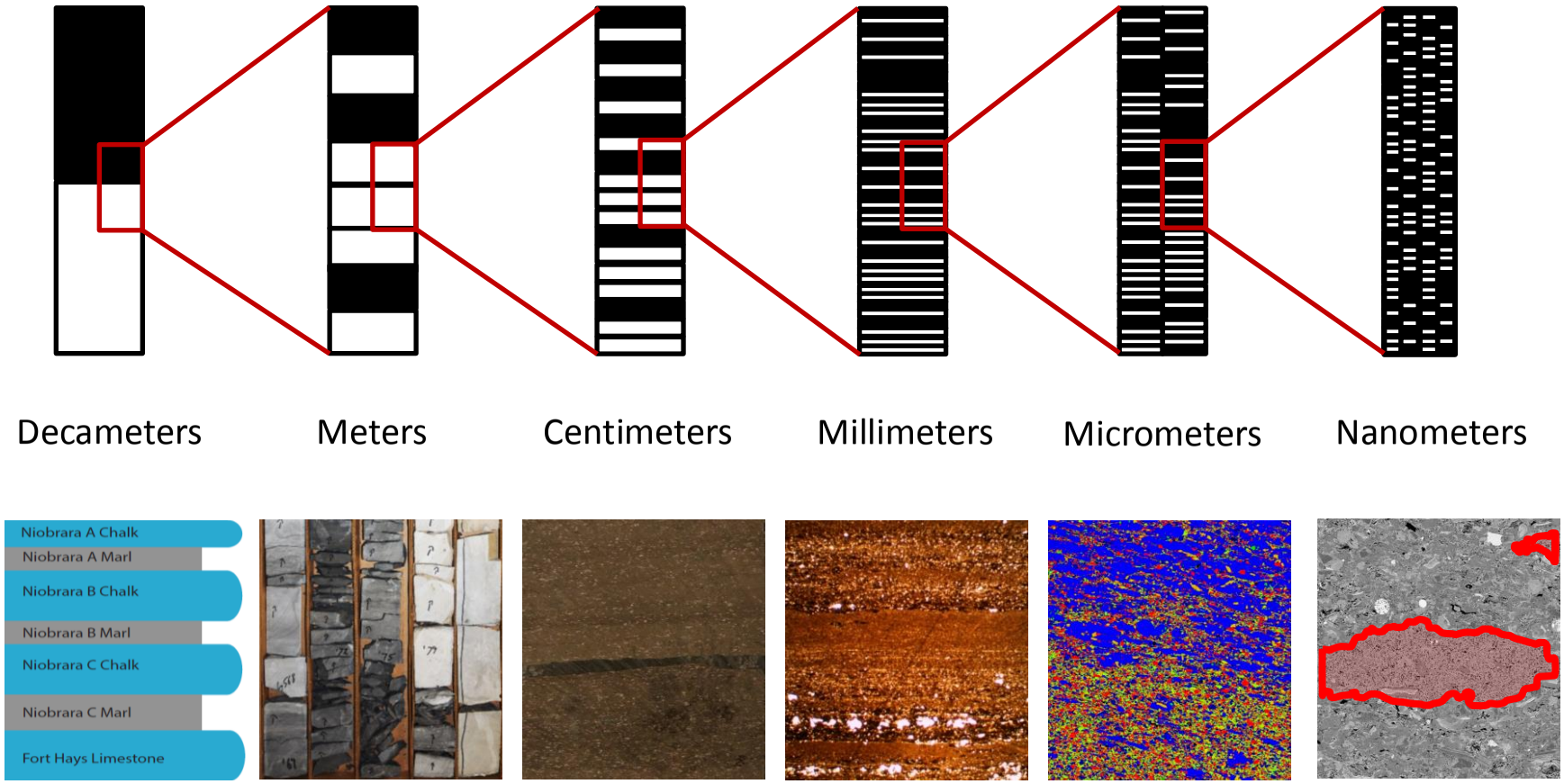

Figure 64. Schematics and examples of heterogeneity on multiple scales within the Niobrara section. The largest scale is to the left and is the stratigraphic zonation seen in the DJ Basin. Moving to the right, a core section of chalk and marl bedsets at the meter-scale. Each of those bedsets contains individual beds and laminae of differing lithologies exemplified by the centimeter-scale image of a cut thin section billet. Those laminae in turn contain millimeter scale heterogeneity in the form of sedimentary structures like the graded beds shown in the thin-section photomicrograph. Within the size of the field of view in the photomicrograph, the elemental microprobe maps reveal individual fabric elements and microorganism shells that vary on the micron scale. And finally, within the individual fabric elements, SEM images reveal another level of heterogeneity within pore shapes and sizes at the nanometer scale.

of favorable pore networks. The observation that calcium content predicts the pre-migration pore system (Fig. 27) but also that the significance of that initial, pre-migration pore system influences the extent that it will be filled by migrating hydrocarbons (Figs. 51) helps further develop the story. The addition of thermal maturity information can help the explorationist identify zones of potentially mobile hydrocarbons and immobile hydrocarbons, and also estimates of the extent of porosity development within those hydrocarbons (Fig. 65). Core and log-based fracture analysis help complete the picture.

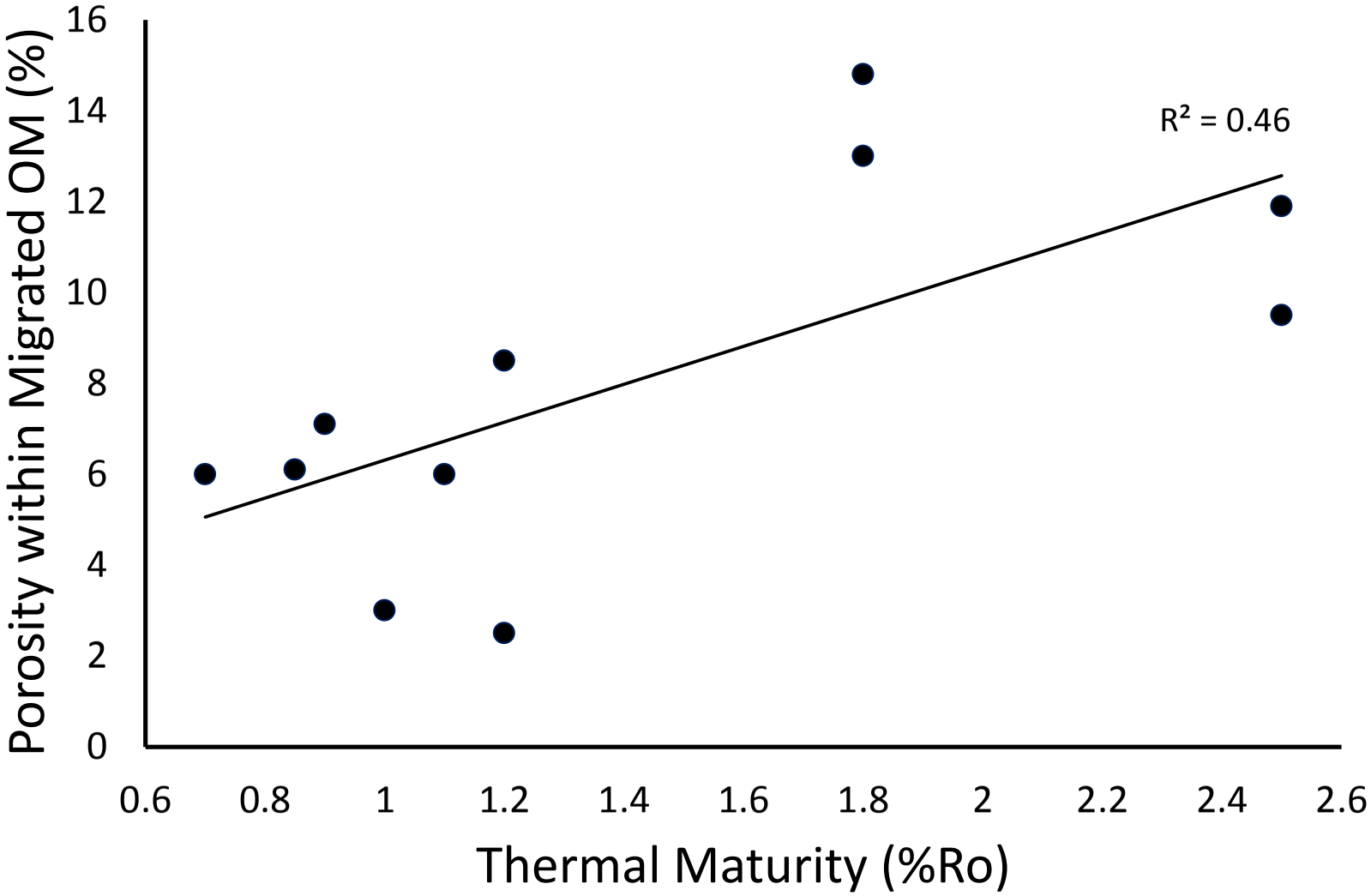

Figure 65. Abundance of porosity within pore-filling migrated organic material as a function of thermal maturity. Line is a best fit linear regression. Data from Burt (2014) and Michaels (2014).

Chapter 7: Conclusions

The pore networks of the Niobrara Formation in the Denver-Julesburg Basin and Niobrara Member of the Mancos Shale Formation in the Piceance Basin were imaged and analyzed at the nanometer to micron scale using Ar-milled surfaces and scanning electron microscopy. This effort expands upon the findings of Burt (2014) and Michaels (2014) and increases our understanding of the role lithology plays in the pre-migration pore systems of the Niobrara. The findings of this study can be focused into five main points:

1) Total, pre-migration porosity strongly correlates to calcium concentration (lithology) in both the DJ and Piceance basins. Pre-migration porosity increases from 3.4 to 11.7 percent while lithology ranges from marly shale to chalk with a correlation coefficient of 0.85. This positive correlation is also seen when considering matrix porosity and matrix calcium content with a correlation coefficient of 0.79.
2) Size, shape, and orientation of individual pores also correlate, with varying significance, to calcium concentrations (lithology). Both equivalent circular diameter (ECD) and pore width increase in both matrix and total pores (matrix plus peloid pores) as lithologies shift from shalier to chalkier lithologies. Pores in chalkier lithologies also consistently have a more equant median anisotropy (shapes). Pores in shalier lithologies tend to be more consistently horizontal as compared to pores in chalkier lithologies. These size, shape, and orientation trends are derived from the increased presence of clay in the shalier samples. The more elongate and ductile clay grains tend to compact and align during compaction, decreasing their size and roundness and increasing their horizontality. These factors likely contribute to

slowed or even blocked migration of lager hydrocarbon particles through the more shaley lithologies.

3) The total porosity and individual pore characteristics are more consistent between samples and basins in peloids (all calcite) than in the matrix (18.7-96.2% calcite). Not surprisingly, the same patterns recognized in total porosity and individual pore characteristics with regards to lithology variation apply to peloids and matrices. Pores within peloids, which are dominantly calcitic, tend to display similar size, shape, and orientation patterns as the most calcium-rich lithologies regardless of the entire sample's lithology. Pores within the variable lithology matrices vary strongly in size, shape, and orientation with matrix calcium content. This observation, though not new, helps bolster the claims that large, well-connected pores, can consistently be found in peloids.

4) The amount of pre-migration porosity influences the proportion of that porosity that is occluded during hydrocarbon migration. In the seven samples analyzed for current porosity (porosity not occluded by residual migrated hydrocarbons), total (matrix plus peloid), matrix, and peloid porosity all show moderate to strong correlations between amount of original porosity and the proportion of that original amount filled by migrated hydrocarbons. This suggests that hydrocarbon saturation (the percentage of porosity filled with hydrocarbons) will increase in rocks with greater initial, pre-migration porosity.

5) Pore connectivity was assessed by the porosity and number of pores that will be large enough for the passage of various hydrocarbon compounds. With larger

compounds (up to 1000nm), total porosity decreased by upwards of 75% in all samples while the number of pores decreased by over 90%. Peloid pores showed consistently smaller decreases and presumably more connected 3-D systems while matrix pores became extremely isolated.

As with all studies at this scale, upscaling is a primary concern to oil and gas explorationsists seeking to use this type of information. By tying observations made on the nanometers and micron scales to well log (lithology) and core facies (peloid abundance), greater efficiency can be achieved in the identification of favorable pore systems in the Niobrara Interval.

References

Ball, B. A., Cobban, W. A., Merewether, E. A., Grauch, R. I., McKinney, K. C., AND Livo, K. E., 2010, Fossils, Lithologies, and Geophsyical Logs of the Mancos Shale from Core Hole USGS CL-1 in Montrose County, Colorado: USGS Open-File Report, v. 1294, p. 1-38.

Burt, C. C., 2014, Pore Systems of the Tow Creek Bench of the Niobrara Member of the Mancos Shale Formation, Piceance Basin, Colorado: Masters Thesis, University of Colorado, Boulder, Colorado.

Chalmers, G.R., Bustin R.M., AND Power, I.M, 2012, Characterization of Gas Shale Pore Systems by Porosimetry, Pycnometry, Surface Area, and Field Emission Scanning Electron Microscopy/Transmission Electron Microscopy Image Analyses: Examples From The Barnett, Woodford, Haynesville, Marcellus, and Doig Units: AAPG Bulletin, v. 96, p. 1099–1119.

Cumella, S.P., Graven, E., Weimer, P., AND Rogers, N., 2014, Piceance Basin Niobrara Mancos Gas Accumulation, in Oil & Gas Fields of Colorado: Rocky Mountain Association of Geologists, v. 2012, p. 236-257.

Curtis, M. E., Ambrose, R. J., Sondergeld, C. H., AND Rai, C. S., 2010, Structural Characterization of Gas Shales on the Micro- and Nano-Scales: Canadian Unconventional Resources and International Petroleum Conference, 19-21 October 2010, Calgary, Alberta, Canada.

Curtis, M. E., Cardott, B. J., Sondergeld, C. H., AND Rai, C. S., 2012, Development of Organic Porosity in the Woodford Shale with Increasing Thermal Maturity: International Journal of Coal Geology, v. 103, p. 26-31.

Fishman, N. S., Hackley, P. C., Lowers, H. A., Hill, R. J., Egenhoff, S. O., Eberl, D. D., AND Blum, A. E., 2012, The Nature of Porosity in Organic-Rich Mudstones of the Upper Jurassic Kimmeridge Clay Formation, North Sea, Offshore United Kingdom: International Journal of Coal Geology, v. 103, p. 32-50.

Hattin, D. E., 1975, Petrology of Fecal Pellets in Upper Cretaceous Strata of Kansas and Saskatchewan: Journal of Sedimentary Petrology, v. 45, p. 686-696.

Hattin, D. E., 1981, Petrology of Smoky Hill Member, Niobrara Chalk (Upper Cretaceous), in Type Area, Western Kansas: AAPG Bulletin, v. 65(5), p. 831-849.

Heath, J. E., Dewers, T. A., McPherson, B. J. O. L., Petrusak, R., Chidsey, T. C., Rinehart, A. J., AND Mozley, P. S., 2011, Pore Networks in Continental and Marine Mudstones: Characteristics and Controls of Sealing Behavior: Geosphere, v. 7, p. 429-454.

Jarvie, D., 2010, Worldwide Shale Resource Plays and Potential: AAPG European Region Annual Conference, v. 80144, p. 848-861.

Kauffman, E. G., 1977, Geological and Biological Overview: Western Interior Cretaceous Basin: Rocky Mountain Association of Geologists, v. 14, p. 75-99.

Locklair, R. E., AND Sageman, B. B., 2008, Cyclostratigraphy of the Upper Cretaceous Formation, Western Interior, USA: A Coniacian-Santonian Orbital Timescale: Earth and Planetary Science Letters, v. 269, p. 540-553.

Lockridge, J. P., AND Scholle, P. A., 1978, Niobrara Gas in Eastern Colorado and Northwestern Kansas: Rocky Mountain Association of Geologists, Energy Resources in the Denver Basin, p. 35-49.

Longman, M. W., Luneau, B. A., AND Landon, S. M., 1998, Nature and Distribution of Niobrara Lithologies in the Cretaceous Western Interior Seaway of the Rocky Mountain Region: The Rocky Mountain Association of Geologists, Revisiting and Revitalizing the Niobrara in the Central Rockies, p. 137-170.

Loucks, R. G., Reed, R. M., Ruppel, AND S. C., Jarvie, D. M., 2009, Morphology, Genesis, and Distribution of Nanometer-Scale Pores in Siliceous Mudstones of the Mississippian Barnett Shale: Journal of Sedimentary Research, v. 79, p. 848-861.

Loucks, R. G., Reed, R. M., Ruppel, S. C., AND Hammes, U., 2010, Preliminary Classification of Matrix Pores in Mudrocks: Gulf Coast Association of Geological Societies Transactions, v. 60, p. 435–441.

Loucks, R. G., Reed, R. M., Ruppel, S. C., AND Hammes, U., 2012, Spectrum of Pore Types and Networks in Mudrocks and a Descriptive Classification for Matrix-Related Mudrock Pores: AAPG Bulletin, v. 96, p. 1071–1098.

Lu, J., Ruppel, S. C., AND Rowe, H. D., 2015, Organic Matter Pores and Oil Generation in the Tuscaloosa Marine Shale: AAPG Bulletin, v. 99, p. 333-357.

May, J. A., AND Anderson, D. S., 2013, Mudrock Reservoirs — Why Depositional Fabric and Sequence Stratigraphic Framework Matter: AAPG Search and Discovery Distinguished Lecturer Tour, 80338, 2012–2013.

Michaels, J. H., 2014, Pore Systems of the B Chalk and lower A Marl Zones of the Niobrara Formation, Denver-Julesburg Basin, Colorado: Masters Thesis, University of Colorado, Boulder, Colorado.

Milliken, K. L., AND Reed, R. M., 2010, Multiple Causes of Diagenetic Fabric Anisotropy in Weakly Consolidated Mud, Nankai Accretionary Prism, IODP Expedition 316: Journal of Structural Geology, v. 32, p. 1887-1898.

Milliken, K. L., Esch, W. L., Reed, R. M., AND Zhang, T., 2012, Grain Assemblages and Strong Diagenetic Overprinting in Siliceous Mudrocks, Barnett Shale (Mississippian), Fort Worth Basin, Texas: AAPG Bulletin, v. 96, p. 1553–1578.

Milliken, K. L., Rudnicki, M., Awwiller, D. N., AND Zhang, T., 2013, Organic Matter-Hosted Pore System, Marcellus Formation (Devonian), Pennsylvania: AAPG Bulletin, v. 97, p. 177–200.

Milliken, K. L., Ko, L. T., Pommer, M., AND Marsaglia, K. M, 2014, SEM Petrography of Eastern Mediterranean Sapropels: Analogue Data for Assessing Organic Matter in Oil and Gas Shales: Journal of Sedimentary Research, v. 84, p. 961–974.

Milne, J. J., AND Cumella, S. P., 2014, Niobrara and Codell Tight Oil Accumulation, a New Era of Oil Production from Horizontal Wells, DJ Basin of Northern Colorado, Oil & Gas Fields of Colorado- 2014, p. 74-94.

Momper, J. A., 1978, Oil Migration Limitations Suggested by Geological and Geochemical Considerations: Physical and Chemical Constraints on Petroleum Migration: AAPG Short Course.

Murray, R. C., 1960, Origin of Porosity in Carbonate Rocks: Journal of Sedimentary Petrology, v. 30, p. 59-84.

Nelson, P. H., Santus, S. L., 2011, Gas, Oil and Water Production from the Wattenburg Field in the Denver Julesburg Basin, Colorado: USGS Open File Report, v. 1175, p. 1-23.

Peterson, V.E., 1955, Fracture Production from the Mancos Shale, Rangely Field, Rio Blanco County, Colorado: Rocky Mountain Association of Geologists, Guidebook to the Geology of Northwest Colorado, p. 101-106.

Pettijohn, F. J., 1975, Sedimentary Rocks, Third Edition, Harper Row Publisher, New York, p. 628.

Pollastro, R. M., 1981, Authigenic Kaolinite and Associated Pyrite in Chalk of the Cretaceous Niobrara Formation, Eastern Colorado: Journal of Sedimentary Research, v. 51, p. 553-562.

Pollastro, R. M., AND Scholle, P. A., 1986, Exploration and Development of Hydrocarbons from Low-Permeability Chalks--An Example from the Upper Cretaceous Niobrara Formation, Rocky Mountain Region: Geology of Tight Gas Reservoirs, p. 129-141.

Pommer, M. E., Milliken, K. L., AND Ozkan, A, 2014, Pore Types Across Thermal Maturity within the Eagle Ford Formation, South Texas: AAPG Annual Convention and Exhibition, Houston, TX, April 7, 2014.

Rogers, N. T., 2012, Subsurface Stratigraphy of the Upper Cretaceous Lower Mancos Formation and Related unites, Piceance Basin, Northwestern Colorado: Masters Thesis, University of Colorado, Boulder, Colorado.

Sageman, B. B., Singer, B. S., Meyers, S. R., Siewert, S. A., Walaszczyk, I., Condon, D. J., Jicha, B. R., Obradovich, J. D., AND Sawyer, D. A., 2014, Integrating $^{40}Ar/^{39}Ar$, U-Pb, and Astronomical Clocks in the Cretaceous Niobrar Formation, Western Interior Basin, USA: GSA Bulletin, v. 126, p. 956-973.

Schieber, J., 2010, Common Themes in the Formation and Preservation of Intrinsic Porosity in Shales and Mudstones – Illustrated With Examples Across the Phanerozoic: SPE Unconventional Gas Conference, 23-25 February 2010, Pittsburgh, Pennsylvania, USA.

Scholle, P. A., 1977, Chalk Diagenesis and its Relation to Petroleum Exploration: Oil from Chalks, a Modern Miracle?: AAPG Bulletin, v. 61, 982-1009.

Scholle, P. A., AND Arthur, M. A., 1980, Carbon Isotope Fluctuations in Cretaceous Pelagic Limestones: Potential Stratigraphic and Petroleum Exploration Tool: The American Association of Petroleum Geologists Bulletin, v. 64, p. 67-87.

Scholle, P. A., AND Halley, R. B., 1985, Burial Diagenesis: Out of sight, out of mind!: SEPM Special Publication, v. 36, p. 309-334.

Scholle, P. A., AND Pollastro, R. M., 1985, Sedimentology and Reservoir Characteristics of the Niobrara Formation (Upper Cretaceous), Kansas and Colorado; Rocky Mountain Carbonate Reservoirs; a Core Workshop: SEPM Core Workshop, v. 7, p. 447-482.

Scott, G. R., AND Cobban, W. A., 1964, Stratigraphy of the Niobrara Formation at Pueblo, Colorado: USGS Professional Paper, v. 454, p. 27.

Sonnenberg, S. A., 2011, The Niobrara Petroleum System: A New Resource Play in the Rocky Mountain Region: Rocky Mountain Association of Geologists, Revisiting and Revitalizing the Niobrara in the Central Rockies, p. 13-32.

Slatt, R. M., AND O'Brien, N. R., 2011, Pore Types in the Barnett and Woodford Gas Shales: Contribution to Understanding Gas Storage and Migration Pathways in Fine-Grained Rocks: AAPG Bulletin, v. 95, p. 2017–2030.

Tian, H., Pan, L., Xiao, X., Wilkins, R. W. T., Meng, Z., AND Huang, B., 2013, A Preliminary Study on the Pore Characteristics of the Lower Silurian Black Shales in the Chuandong Thrust Fold Belt, Southwestern China Using Low Pressure N_2 Adsoprtion and FE-SEM Methods: Marine and Petroleum Geology, v. 48, p. 8-19.

Weimer, R. J., 1983, Relation of Uncomformities, Tectonicsm and Sea Level Changes, Cretaceous of the Denver Basin and Adjacent Area Areas: Rocky Mountain Section SEPM, Mesozoic Paleogeography of the West-Central United States: Rocky Mountain Paleogeography Symposium 2, p. 359-376.

Williams, P., AND Lyle, D., 2011, Bring in the Rigs: The Rocky Mountain Association of Geologists, Revisiting and Revitalizing the Niobrara in the Central Rockies, p. 33-40.

Zhao, X., Li, Q., Jiang, Z., Zhang, R., Li, Haipeng., 2014, Organic Geochemisty and Reservoir Characterization of the Organic Matter-Rich Calcilutite in the Shulu Sag, Bohai Bay Basin, North China: Marine and Petroleum Geology, v. 51, p. 239-255.